Università degli Studi di Ferrara

Doctoral course in Physics

XXXII cycle

Director Prof. Eleonora Luppi

Water decontamination from organic micropollutants via photocatalytic solar systems based on WO_3 photoanodes

Disciplinary sector: Fis/01

Supervisor

Prof. Donato Vincenzi

Candidate

Dott. Micol Boschetti

Co-advisor

Prof. Stefano Caramori

Years 2016–2019

Referees of the thesis

Prof. Luca Pasquini
Department of Physics and Astronomy, University of Bologna, Italy

Dr. Laura Meda
ENI-Donegani Institute, Research Center for Non-Conventional Energies of ENI S.p.A., Novara, Italy

Ph.D. candidate

Micol Boschetti
Department of Physics and Earth Science, University of Ferrara, Italy

Supervisor

Prof. Donato Vincenzi
Department of Physics and Earth Science, University of Ferrara, Italy

Co-advisor

Prof. Stefano Caramori
Department of Chemical and Pharmaceutical Sciences, University of Ferrara, Italy

Abstract (English)

The development of new materials and processes with a sustainable approach to allow an efficient removal from water sources of emergent contaminants, such as drugs and antibiotics, currently represents the next challenging task in water decontamination field. Photocatalysis and photoelectrocatalysis processes triggered via sunlight are among the most efficient Advanced Oxidation Processes for water decontamination. These methods are based on the interaction in water of natural light with oxide semiconductors, which generate high-reactive chemical species able to oxidize the organic micropollutants.

Here, the realization of two solar devices is presented, namely a parabolic concentrator and a modular stand-alone reactor. Their working principle is based on the photocatalysis and photoelectrocatalysis processes. As active material integrated within the solar devices, nanostructured tungsten trioxide was investigated via several realization techniques—solvothermal, electrochemical oxidation, and sol-gel—on glass and metal substrates. WO_3-based electrodes attained photocurrents in the range of 1–5 mA/cm^2, consistent with literature, and an activation in the visible part of the solar spectrum, up to ∼470 nm. Photodegradation tests, carried out on several specific drugs, showed outstanding results with an almost complete abatement in case of some pollutants, and a COD (Chemical Oxygen Demand) decrease of more than 60% in 1 h.

Both the solar devices could be scaled up in the next future for industrial scopes within the tertiary water treatment. Most importantly, they use a sustainable process, without additional energy costs, and with a possible hydrogen production as added value to the decontamination process.

Keywords: Wastewater treatment - AOPs - Photocatalysis - WO_3 - Photocatalytic reactor

Abstract (Italiano)

Nell'ambito del trattamento delle acque è emersa la necessità di sviluppare nuovi materiali e processi al fine di consentire un'efficiente rimozione di contaminanti emergenti, quali droghe e antibiotici, attualmente presenti nei bacini idrici, sfruttando un approccio sostenibile. I metodi di fotocatalisi e di fotoelettrocatalisi innescati da luce solare sono tra i processi di ossidazione avanzata più efficaci per la decontaminazione delle acque. Tali metodi sono basati sull'interazione in acqua di luce solare con ossidi semiconduttori; questa interazione genera specie chimiche altamente reattive, capaci di ossidare i microinquinanti organici, quindi purificando l'acqua.

In questo lavoro sono presentati due dispositivi solari, ossia un concentratore solare e un reattore autonomo modulare, il cui principio di funzionamento si basa sui processi di fotocatalisi e fotoelettrocatalisi. Come materiale attivo integrato all'interno dei dispositivi solari è stato studiato il triossido di tungsteno nanostrutturato. In particolare, diverse tecniche di realizzazione—solvotermale, anodizzazione elettrochimica, e sol-gel—sono state caratterizzate sfruttando substrati in vetro e metallo. Gli elettrodi basati su WO_3 hanno raggiunto fotocorrenti di 1–5 mA/cm^2, consistenti con quelle riportate in letteratura, e un'attivazione nella parte visibile dello spettro solare fino a $\sim$470 nm. I test di fotodegradazione, effettuati su alcuni specifici medicinali, hanno mostrato notevoli risultati, con un abbattimento pressoché totale di alcuni inquinanti, e una diminuzione di oltre il 60% del COD (Domanda Chimica di Ossigeno) in 1 ora.

Entrambi i dispositivi solari possono essere ampliati in un prossimo futuro a scopi industriali per il trattamento terziario delle acque, sfruttando un processo sostenibile, senza costi energetici aggiuntivi e con una possibile produzione di idrogeno come valore aggiunto al processo di decontaminazione.

Keywords: Trattamento acque - AOP - Fotocatalisi - WO_3 - Reattore fotocatalitico

Contents

Preface

Most of the human activities that use water produce wastewater: municipal agricultural, domestic, and industrial wastes are only some of the major types. On the one hand, the quantity of produced wastewater and its overall pollution load are continuously increasing worldwide, and on the other hand, the overall demand for clean water is growing at a rate of about 1% per year as a consequence of population growth, economic development, and changing consumption pattern, among other factors, and it will continue to significantly grow over the next two decades. It has been estimated that about 3.6 billion people—about half of the world population—will potentially face water scarcity in 2025, and this number will probably increase to 4.8–5.7 billion in 2050 [1].

In addition to this problem, since 1990s water pollution has worsened in almost all rivers in Africa, Asia, and Latin America, because here the incidence of the developing countries is greater [2]. Since the deterioration of water quality is expected to further escalate over the next decades, the risks for human and environmental health will follow the same trend [3]. Moreover, hundreds of chemicals are also impacting on water quality. Agricultural intensification has already increased the worldwide chemical use to approximately two million tons per year, with herbicides accounting for 47.5%, insecticides for 29.5%, fungicides for 17.5%, and others for 5.5% [4]. Emerging contaminants are continually increasing, and are often detected at concentration higher than expected. Examples include pharmaceuticals, hormones, industrial chemicals, personal care products, flame retardants, detergents, perfluorinated compounds, caffeine, fragrances, cyanotoxines, antibiotics, drugs, nano-materials, and anti-microbial cleaning agents and their transformation products. Impact on people and biodiversity will be mainly delivered via water and is largely unknown [5].

Also climate change will affect water quality in different ways. For example, changes in spatial and temporal patterns and variability of precipitations can affect the surface water flows and hence also the dilution effects, while temperature increase can cause higher evaporation from open sources and soils, and increased transpiration by vege-

tation potentially reduces water availability [6]. Dissolved oxygen will deplete faster because of higher water temperatures, and it can expected that higher content of pollutants will flow into water bodies after extreme rain events [7].

The greatest increase in exposure to pollutants is expected to occur in low and lower-middle income countries, primarily because of higher population and economic growth, in addition to the lack of wastewater management systems. Indeed, an estimated 80% of all industrial and municipal wastewater of such countries is released into the environment without any prior treatment, resulting in a growing deterioration of the overall water quality [5].

As reflected in the target 6.3 of the 2030 Agenda for Sustainable Development, there is the urgent necessity to "improve the water quality by reducing pollution, eliminating dumping and minimizing release of hazardous chemicals and materials, halving the proportion of untreated wastewater and substantially increasing recycling and safe reuse globally". For this reason, many countries are mobilizing to solve the problems concerning the wastewater treatment. To date, several conventional methods for treating wastewater are used by different industries, such as photo-degradation, adsorption, filtration, coagulation, and biological processes within the primary, secondary and tertiary treatments. Unfortunately, some of these techniques are not completely effective because of the high stability of pollutants molecules. Moreover, it is important to know that for a conventional wastewater treatment (WWT) plant about 25–40% of the operating costs is ascribable to energy consumption, which varies in the range of approximately 0.3–2.1 kWh per m^3 of treated water [8].

Given the existing conditions of environmental pollution, drinkable water scarcity, and necessity of clean energy sources, the attention of scientists has been increased in the field of wastewater treatment. The main goal in this context is the development of new different materials and processes, with an ecofriendly green approach, to allow an efficient removal of the contaminants present in the water sources [9]. Here, Advanced Oxidation Processes (AOPs) enter the scene as "near ambient temperature and pressure water treatment processes involving the generation of hydroxyl radicals in a sufficient quantity to affect water purification". In general, AOPs represent a class of treatments that involve the formation of highly-reactive transient chemical species (e.g. superoxide, peroxide, hydroxyl radical), which can ideally convert the recalcitrant organic compounds into inorganic carbon compounds [10]. The most efficient processes among the AOPs are those based on hydroxyl radical $^{\bullet}OH$, which is a powerful, non-selective, and green chemical oxidant. These processes are generally based on the dissociation of hydrogen peroxide in water, either by direct absorption of ultraviolet (UV) photons or by mediation with metal ions (Fe and Co are among the most studied) through

Fenton and photo-Fenton reactions. Differently, the more efficient $^{\bullet}OH$ radicals can be generated by the interaction in water of artificial or natural light with semiconductors. This process is commonly known as photocatalysis [11], and can be triggered via sunlight through a photocatalyst, thus exploiting a clean energy source without additional energy costs [12]. As added value, the photocatalysis process can also convert the radiation energy into useful forms of energy and fuels, such as electricity and hydrogen, obtaining a double environmental benefit, in addition to the wastewater treatment. In this case, the combined use of photocatalysis and electrochemistry can be exploited, giving rise to the so-called photoelectrocatalysis.

This thesis research describes the development of two photocatalytic solar systems based on tungsten trioxide photoanodes, targeting the water decontamination from some specific organic pollutants. This work was developed within the HPSolar (High Performance Solar Decontamination) project, which was part of the POR-FESR 2014-2020 program funded by Regione Emilia Romagna and European Union, and was realized in collaboration with laboratories of the University of Ferrara and local companies. A brief overview of this thesis Chapters is shown below.

The first Chapter concerns a theoretical introduction about photocatalysis and photoelectrocatalysis as Advanced Oxidation processes. The fundamental parameters and the general concepts, which are tied to the water splitting, are pointed out and discussed, in particular by describing the working principle of photoelectrochemical cells. Finally, a brief overview of the applications of the photocatalysis and photoelectrocatalysis processes in the field of wastewater decontamination is depicted, by focussing on the state of the art of existing prototypes.

Following, a short overview about the semiconductors that are present to date in literature as active materials for the photocatalysis process is given as introduction of the second Chapter. After this theoretical preface, an experimental part is described, which concerns the studied materials and the methods used to improve the photocatalytic efficiency of the semiconductors. In particular, the most-known-in-literature titanium dioxide has been studied since, once doped with nitrogen, it can extend its active range into the visible light. Later on, an investigation concerning tungsten trioxide is presented, by explaining three different realization methods on diverse substrates. This Chapter points out the realization techniques, the morphological, the electrochemical, and the optical characterizations of the two studied active materials.

Following, the third and fourth Chapters concern the integration of the characterized active materials, in particular the tungsten trioxide electrodes, within the photocatalytic and photoelectrocatalytic solar devices.

In the third Chapter, the realization of a parabolic solar concentrator for wastew-

ater treatment is presented. The described device has been planned starting from a previously designed system, which was built for architectural integration with the aim of energy conversion, from solar into electrical one. The modifications applied to the solar device allow its exploitation in the wastewater treatment field. The pollutant degradation tests worked out on the realized electrodes are displayed, in particular by focussing on several drugs, such as Atenolol, Carbamazepine, Levofloxacine, Ketoprofen, and 4-hydroxybenzaldehyde, which are barely eliminated by the current wastewater treatment plants. In addition, the Chemical Oxygen Demand (COD)—i.e. the amount of oxidizable pollutants that are present in water or wastewater—abatement is shown and discussed.

In the last Chapter, the integration of WO_3 electrodes in a modular stand-alone reactor for solar wastewater decontamination is described. The reactor is composed by single elements, which are based on photoelectrochemical tandem cells. This solar device exploits the photoelectrocatalytic technique for pollutant degradation, with hydrogen production as added value to the decontamination process. Finally, the photodegradation tests carried out on a mix of drugs are presented. The peculiarity of this prototype is the power supply, which is obtained only from solar energy. This feature makes the reactor completely independent and environmentally sustainable.

Each experimental Chapter is completed by a brief summary. Finally, conclusions are given, and some planned further works are described.

CHAPTER 1

The photocatalysis process: theory and applications

Advanced oxidation processes (AOPs) were first defined by Glaze et. al. in 1897 [13] as those processes that involve the generation of hydroxyl radicals ($^{\bullet}$OH) in a sufficient quantity to obtain water purification. During the last years, the development of AOPs, and the various methods to generate hydroxyl radicals and other reactive oxygen species have been of increasing interest for the scientific community. Many methods are classified under the ample definition of AOPs since they include all the processes that involve the use of oxidizing agents such as hydrogen peroxide (H_2O_2) or ozone (O_3), in addition to hydroxyl radicals, catalysts (iron ions, metal oxide electrodes), and irradiation (UV light, solar light, ultrasound), separately or in combination with mild conditions (low temperature and pressure). Among all the methods, light driven AOPs are supposed to be the most attractive ones for wastewater treatment due to the abundance of the solar light in regions where clean water scarcity is higher, and comparatively low costs and high efficiencies. In particular, the photocatalysis process is the most widely used in the field of clean and green chemistry since it can exploit light to work. Indeed, the photocatalysis process does not pollute the atmosphere and the environment, contrary to many chemical and physical processes that are exploited in wastewater treatment [12].

Generally, advanced oxidation is based on three basic steps. The first one involves the formation of strong oxidants like $^{\bullet}OH$, $HO_2^{\bullet}$, $O_2^{-\bullet}$. In the second step, these oxidants react with organic contaminants present in wastewater, converting them into biodegradable compounds. Finally, the oxidation of the biodegradable intermediates occurs, leading to a complete mineralization in water, carbon dioxide, and inorganic

salts.

Among the strong oxidants, the hydroxyl radical is the most reactive oxidizing agent, able to react unselectively and instantaneously with the surrounding chemicals, including organic pollutants and inhibitors. $^{\bullet}OH$ has an oxidation potential between 2.8 V (pH 0) and 1.95 V (pH 14) vs SCE (Saturated Calomel Electrode), which is strongly dependent on the pH conditions [14].

Thanks to these characteristics, AOPs possess many advantages with respect to other traditional methods for treatment of water, showing [12]:

- high reaction rates;
- a potential to reduce toxicity and completely mineralize organic contaminants;
- the ability of not accumulating waste for further treatment like methods using membranes or activated carbon absorption;
- the ability of not creating sludge as in the case of physical, chemical, or biological processes, which are included within the primary and secondary stages in treatment plants;
- a non selective pathway, which allows the treatment of different organics at a time.

In this first chapter, the working principles of photocatalysis and photoelectrocatalysis as advanced oxidation processes are introduced. Then, the fundamental parameters and the general concepts that are tied to water splitting and to water decontamination are pointed out and discussed in order to understand the operating principle of the so-called photoelectrochemical (PEC) cell. Finally, a brief overview of the possible applications in the field of the wastewater purification is depicted, focussing on the state of the art of already created prototypes.

1.1 Fundamentals of photocatalysis

As well known, photocatalysis is a process that involves the activation of a catalyst by means of light, thus having a photonic activation from the incident radiation. Sunlight contains photons with energies that reflect the Sun's surface temperature; the solar photons reaching the Earth surface range in energy from about 3.5 eV (for wavelength λ of 350 nm) to 0.5 eV (λ of 2500 nm) (Fig. 1.1) [15]. The energy of the visible region ranges from 3.0 (violet) to 1.88 eV (red); the peak power of the Sun occurs in the yellow region of the visible part, at about 2.5 eV. At high noon on a cloudless day, the

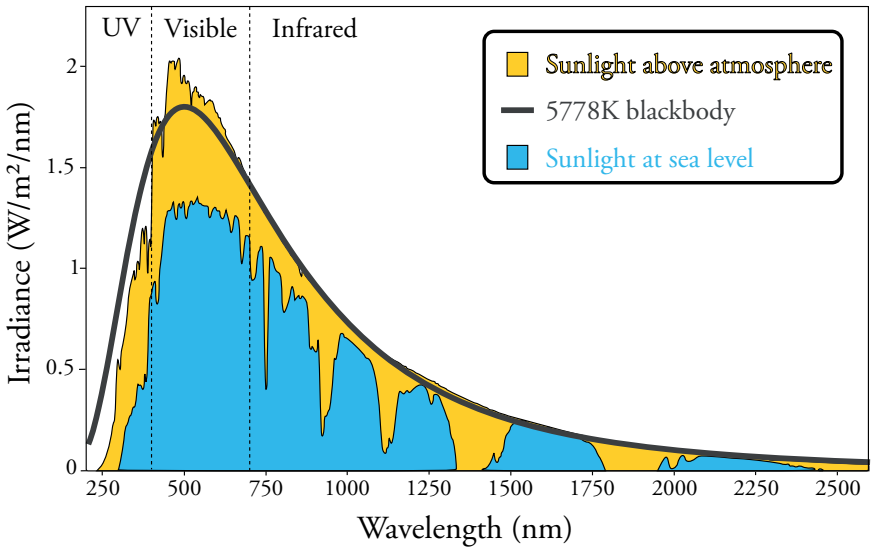

Figure 1.1: Spectral distribution of solar irradiance.

surface of the Earth at average latitudes receives 1000 watts of solar power per square meter (1 kW/m^2). Such standard irradiance is usually expressed as Air Mass 1.5 (AM 1.5) condition.

In solid-state physics, band theory describes with a theoretical model the electron states in solid materials, where electrons can have energy values only within certain specific ranges, occupying atomic orbitals. Due to the essentially infinite number of atoms and the consequential numbers of interacting orbitals that must be considered in a solid, the spacing of electronic energies becomes so small that they can be considered as a continuum of energy levels, and the electronic structure of the solid could be discussed in terms of energy bands. The energy difference between the maximum of the valence band (VB, the band of the saturated levels) and the minimum of the conduction band (CB, the band of the empty levels) is known as the band gap E_g. The entity of the energy gap is essentially determined by the degree of overlap between the atomic orbitals involved. According to the thickness of the band gap, materials are classified in three basic categories: metals or conductors ($E_g < 1.0$ eV), semiconductors ($E_g \simeq 1.5$–3.0 eV), and insulators ($E_g > 5.0$ eV), as shown in Figure 1.2 [12].

Semiconductors are materials of particular interest, displaying a range of useful properties, and thus having an enormous impact on our society, since they are the basic components of devices and electronic circuits. All the photocatalysts in general are semiconductors; in particular, they are metal oxide semiconductors (MOSs). Due to their versatile configuration and integration, MOSs have a wide range of applications, also involved in environmental issues, thanks to their capacity to form charge carriers

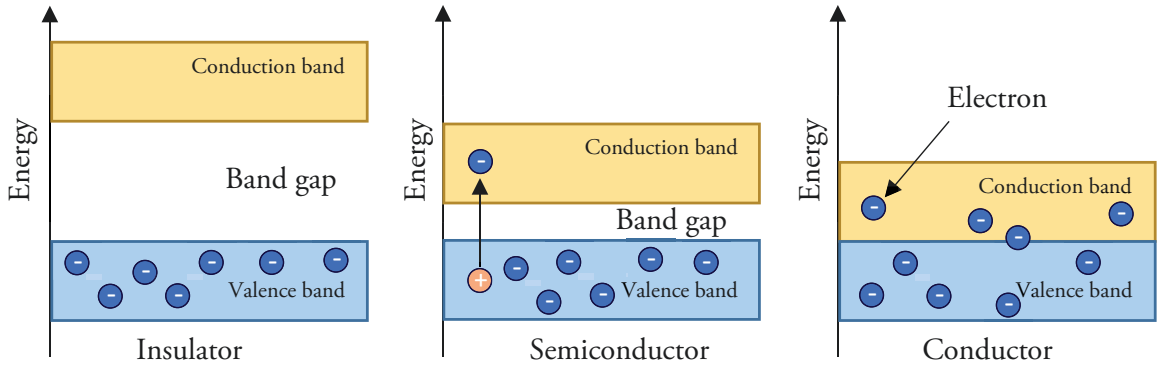

Figure 1.2: Different kind of materials (insulator, semiconductor and conductor) based on the band gap.

when they are exposed to light. In MOSs, the valence band derives from the filled orbitals of O^{2-}, while the conduction band results from the empty orbitals of the metal. Examples of metal oxide semiconductors are reported in Table 1.1, where each value of the energy gap is expressed in volts, referring to the potential, and in nanometers, referring to the wavelength.

As just anticipated, it is well known that, in case of a semiconductor used as a photocatalyst, when the material is exposed to a radiation with a particular wavelength, the absorption of photons with energy E equal to $E = h\nu$ above the band gap E_g, generates electron (e^-) hole (h^+) pairs. Here, h is the Planck's constant and ν is the frequency of the absorbed photon. Indeed, when an electron in the valence band

Table 1.1: Band gap energies of some oxide semiconductors in an electrolytic solution at pH 0. Adapted from [16].

Oxide semiconductor	E_{gap}(V)	E_{gap}(nm)
TiO_2	3.0	410
SnO_2	3.5	350
ZnO_2	3.0	410
$SrTiO_3$	3.2	390
CdS	2.4	520
$CdSe$	1.7	730
$GaAs$	1.4	890
GaP	2.3	540
WO_3	~ 2.7	~ 460
$BiVO_4$	~ 2.5	~ 500
$\alpha - FeO_3$	2-2.2	~ 590

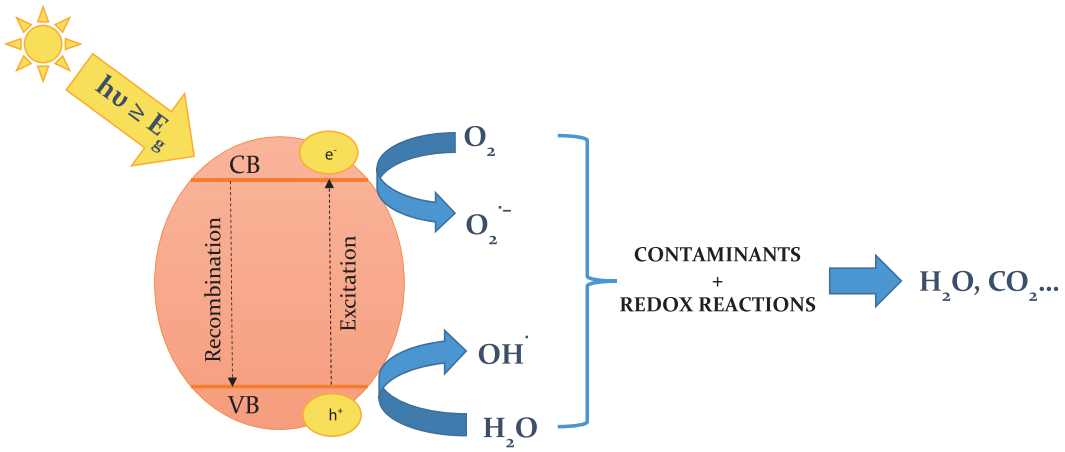

Figure 1.3: Photocatalysis process in a semiconductor particle.

absorbs a photon, it is excited to the conduction band; this process creates a hole in the valence band, leading to the formation of the photo-excited state. The $e^{-}h^{+}$ pairs can either recombine to liberate heat, or make their separate ways to the surface of the semiconductor material, where they have the opportunity of reacting with surface absorbed species, in case of a contact between a photocatalyst and an electrolyte.

The main processes that occur within a semiconductor photocatalyst particle (in Fig. 1.3) in case of photo-excitation in an aqueous solution containing dissolved oxygen and, for example, an oxidizable pollutant, are [17, 18]:

- electron-hole recombination in the bulk;
- electron-hole recombination at the surface;
- direct or indirect (through trap sites) reduction of oxygen, or oxidizing intermediates by the photo-generated electron at the surface of the semiconductor;
- direct or indirect (through trap sites) oxidation of the pollutant, or an oxidized intermediate by the photo-generated hole at the surface of the semiconductor, leading eventually to the mineralization of the pollutant.

In other words, at the semiconductor surface, electrons behave as reducing agents, while holes as oxidizers one.

Conventional photocatalysis has been broadly used exploiting the nanocrystalline anatase type of TiO_2 for light-initiated oxidation of natural toxins in waters. Indeed, the exposure of anatase TiO_2 by UV photons of adequate energy ($\lambda < 380nm$) promotes electrons from valence band to the conduction band, producing a hole as follows [12]:

$$TiO_2 + h\nu \rightarrow e^-_{CB} + h^+_{VB}. \tag{1.1}$$

In this way, the organic substances dissolved in the water can be specifically oxidized by the holes or by the heterogeneous hydroxyl radicals generated by the reaction between the photogenerated hole and the water in solution.

$$h^+_{VB} + H_2O \rightarrow {}^{\bullet}OH + H^+. \tag{1.2}$$

In general conditions, the previous reaction is highly demanding from energetic point of view, since the formation of the hydroxyl intermediate requires a potential of 2.85 V. Nevertheless, the Eq. 1.2 becomes thermodynamically and kinetically feasible in case of wide band gap metal oxides, which will be discussed in the Second Chapter. In addition, other weaker receptive oxygen species (like superoxide radical particles $O_2^{-\bullet}$, $HO_2^{\bullet}$ and H_2O_2) and more ${}^{\bullet}OH$ can be created from the photoinduced electron:

$$e^-_{CB} + O_2 \rightarrow O_2^{-\bullet}, \tag{1.3}$$

$$O_2^{-\bullet} + H^+ \rightarrow HO_2^{\bullet}, \tag{1.4}$$

$$2HO_2^{\bullet} \rightarrow H_2O_2 + O_2, \tag{1.5}$$

$$H_2O_2 + O_2^{-\bullet} \rightarrow {}^{\bullet}OH + OH^- + O_2. \tag{1.6}$$

The major drop in efficiency results from the recombination of photoinduced electrons with either unreacted holes or absorbed ${}^{\bullet}OH$.

$$e^-_{CB} + h^+_{VB} \rightarrow TiO_2 + heat, \tag{1.7}$$

$$e^-_{CB} + {}^{\bullet}OH \rightarrow OH^-. \tag{1.8}$$

In order to understand the charge carriers photo-generation and transport at the semiconductor-electrolyte interface, the kinetic and thermodynamic factors are illustrated below, considering the dark and the illumination conditions.

1.1.1 Thermodynamic and kinetic factors at semiconductor-electrolyte interface

Dark condition

A fundamental parameter described in the band theory is the Fermi level, defined as the top of the available electron energy level at 0 K [19]. This concept comes from the Fermi-Dirac distribution, which is given by Eq. 1.9:

$$f(E) = \frac{1}{1 + e^{\frac{(E-E_F)}{kT}}}, \tag{1.9}$$

where $f(E)$ is the probability that a state of energy E is occupied, E_F the Fermi energy, k the Boltzmann's constant and T the absolute temperature. In case of an intrinsic semiconductor, E_F is the energy level for which $f(E_F) = 1/2$, so that the Fermi level (E_F) is a virtual energy level that has the 50% of probability to be occupied by electrons [15].

As well known, the presence of electron-rich or electron-deficient atoms or defects in the semiconductor lattice brings to the formation of ionizable levels, respectively near to the conduction band or to the valence band. In these cases, the Fermi level position is shifted from the mid-gap, moving closer to the CB if donors are present, or near to the VB in case of acceptor in the lattice. As shown in Figure 1.4, in the first case,

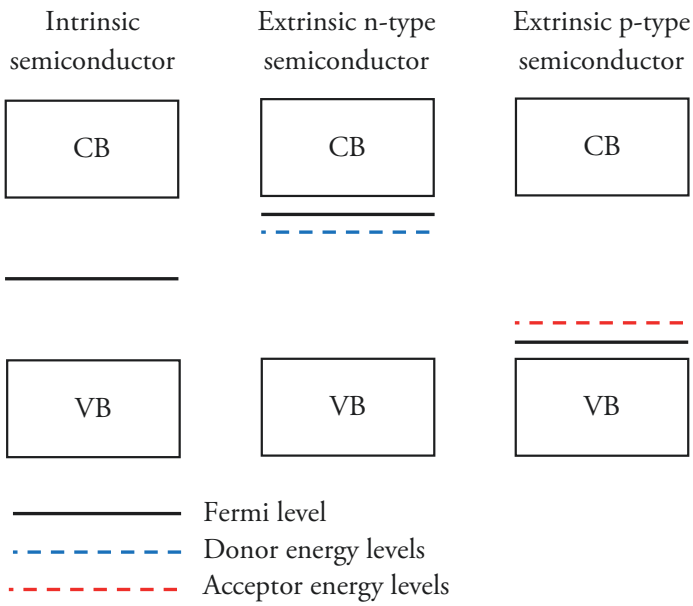

Figure 1.4: Band gap structure of intrinsic, n-type and p-type semiconductors

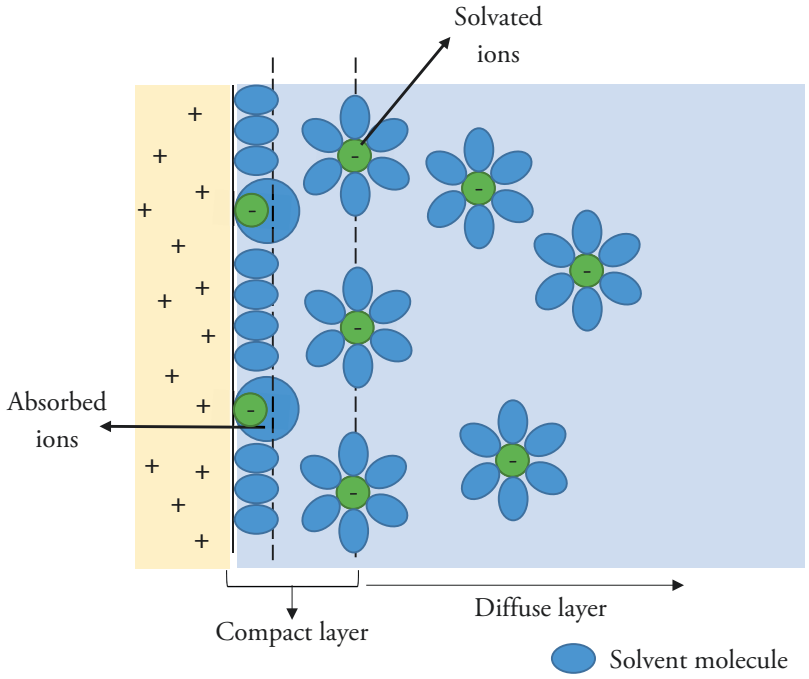

Figure 1.5: Scheme of the compact and diffuse layer at semiconductor-electrolyte interface

a n-type semiconductor is obtained, resulting in an excess of negative charge carriers (e^-) that improve the conductivity of the material, while ionized donors are formed. In the second case, there is the formation of an excess of positive carriers (h^+), that is a p-type semiconductor.

From the electrochemical point of view, the Fermi energy is just the electrochemical potential, or the partial molar free energy per electron. For this reason, the equilibration of the Fermi level is an important concept in the description of the thermodynamic of the semiconductor-electrolyte interface. Indeed, when a semiconductor is placed in contact with an electrolyte in dark conditions, i.e. without an intense irradiation source, a charge transfer occurs across the junction until electronic equilibrium is reached. Here, the Fermi energy of the electrons in the solid is equal to the electrochemical redox potential of the electrolyte, $\mu_{redox} = -eE_{redox}$. The charge transfer results in a current flux, and its direction depends on the relative potential of the two phases. In case of an n-type semiconductor, electrons are transferred from the semiconductor to the solution if E_F is more negative than the electrolyte electrochemical potential. On the contrary, in case of a p-type semiconductor, the electrolyte leaves electrons to the semiconductor.

As can be observed in Fig. 1.5, due to the relatively low density of charge carriers

in the semiconductor (10^{16}-10^{20} cm^{-3}), if the crystalline domain is sufficiently large, a positive space-charge layer of a typical thickness of 10^{-6}–10^{-8} m is formed near the surface [20].

On the one hand, on the electrolyte side, the space-charge layer is counterbalanced by the electrolytic double layer, that is, the so-called compact Helmholtz layer followed by the diffuse Gouy-Chapman layer. On the other hand, on the semiconductor side of the junction, the nature of the band bending depends on the position of the Fermi level in the solid.

Thus, considering an n-type semiconductor, four different situations may occur, as shown in Figure 1.6.

- If the Fermi level of the electrode is equal to the flat band potential, there is no charge excess on both the side of the junction and the bands are flat.

- Referring to a n-type semiconductor, if electrons accumulate at the semiconductor side, an accumulation layer is obtained.

- If, however, they deplete from the solid into the solution, a depletion layer is formed, leaving behind a positive excess charge formed by immobile ionized donor states.

- Finally, electrons depletion can go so far that their concentration at the interface falls below the intrinsic level. As a consequence, the semiconductor become p-type at the surface and n-type in the bulk, corresponding to an inversion layer.

In the case of p-type semiconductors, positive holes are the mobile charge carriers and a space-charge layer of opposite sign (negative) is created by hole transfer to the electrolyte. In other words, n-type semiconductors can be used as so-called photoanode electrodes, since the photo-generated holes reaching the surface drive photo-oxidation reactions, while a p-type material behaves as a photo-cathode electrode.

Considering the case of an n-type semiconductor, it is necessary to spend work to bring an electron from the bulk to the surface. Indeed, the usable free energy collected across a semiconductor-electrolyte interface is limited by the thermodynamic quantities and by kinetic factors.

Thermodynamically, the potential barrier height Φ_B^0 sets the upper limit to the energy that can be extracted from the junction and is given by 1.10:

$$q\Phi_B^0 = E_C - E_F, \tag{1.10}$$

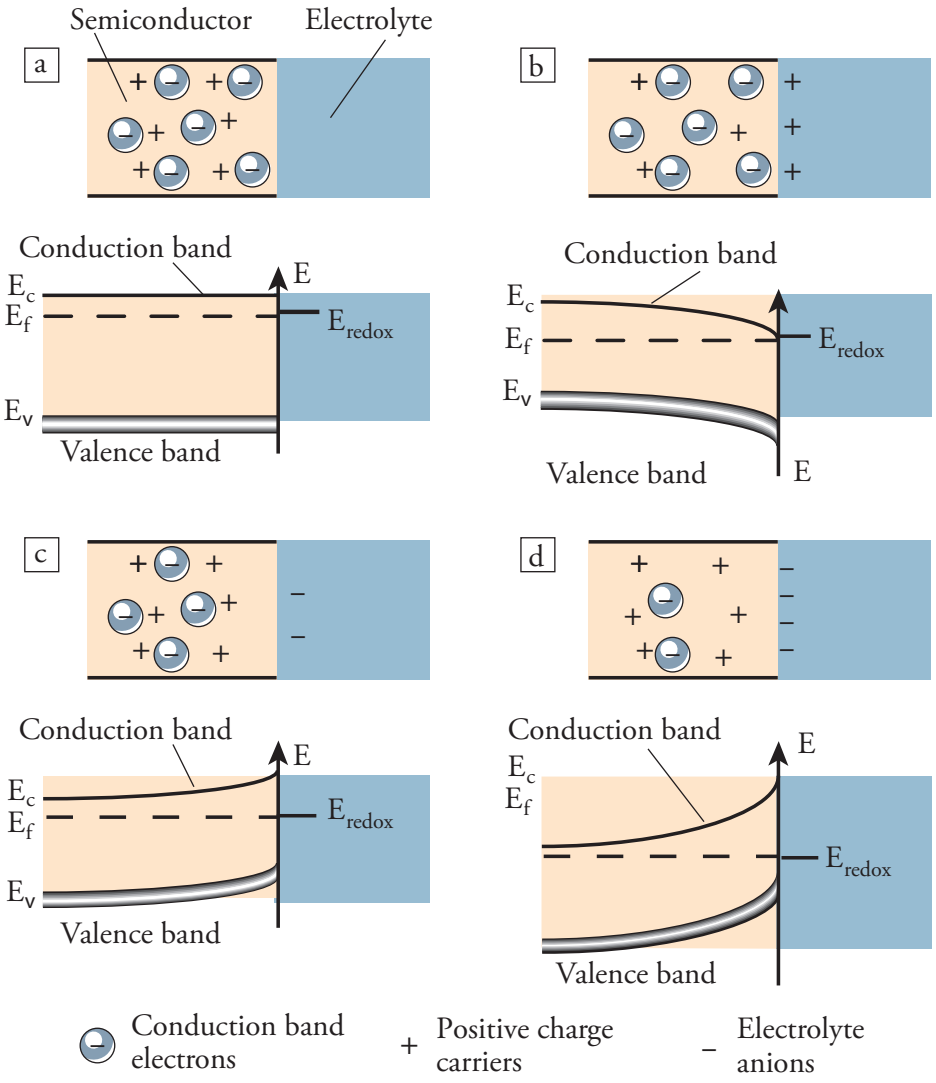

Figure 1.6: Scheme showing the electronic energy levels at the interface between an n-type semiconductor and an electrolyte containing a redox couple. The four cases indicated are: **a**, flat band potential, where no space-charge layer exists in the semiconductor; **b**, accumulation layer, where excess electrons have been injected into the solid producing a downward bending of the conduction and valence band toward the interface; **c**, depletion layer, where electrons have moved from the semiconductor to electrolyte, producing an upward bending of the bends; **d**, inversion layer, where the electrons have been depleted below their intrinsic level, enhancing the upward band bending and rendering the semiconductor p-type at the surface. Adapted from [21].

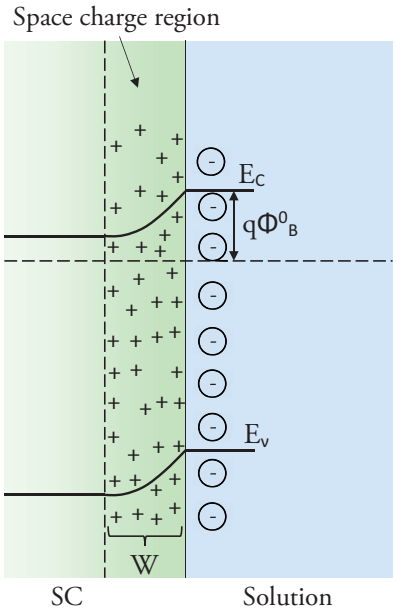

Figure 1.7: Dark equilibration of a n-type semiconductor in contact with an electrolyte containing a redox couple of potential U. Adapted from [20]

where q is the electron charge and E_C the conduction band edge at the surface, as indicated in Fig. 1.7. When the semiconductor is under illumination, the quantity related to the potential barrier is the open circuit photovoltage V_{OC} of the junction.

From the kinetic point of view, the usable free energy collected across the semiconductor/electrolyte interface is limited by the critical competition between the favorable process of charge separation and energy wasting charge recombination. The latter can occur inside and outside the depletion layer, by trapping into intraband-gap states at the surface of the solid and also by electron tunnelling to the acceptor states of the electrolyte through the potential barrier [22].

Illumination condition

As previously described, under illumination, when the semiconductor absorbs a photon with an energy greater than the energy gap, an electron is promoted from the VB to the CB, creating an hole. With respect to the dark condition, different electrochemical potentials, called quasi-Fermi levels, are defined, as shown in Figure 1.8. Light intensity and absorption properties of the semiconductor affect the quasi-Fermi levels.

The photo-generated electrons and holes can move toward the electrode under the electric field in the space charge layer. If a depletion layer is produced, the minority carriers travel along the surface, giving rise to the charge transfer reactions, while the

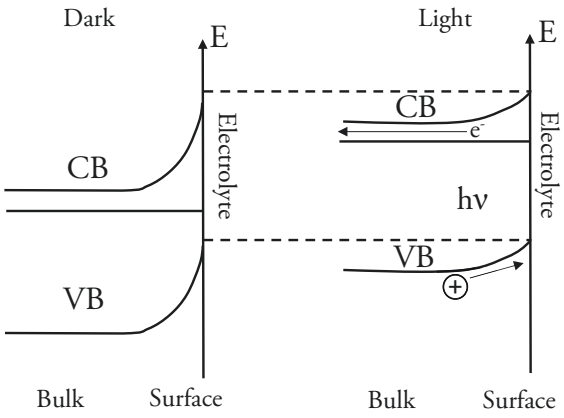

Figure 1.8: Illumination condition of a n-type semiconductor-electrolyte interface.

majority carriers move into the bulk. This phenomenon creates a photocurrent. Such a migration also induces an inverse potential into the electrode, called photo-potential, which reduces the potential drop across the space charge layer.

Quantitative models that account for the photo-effects in illuminated semiconductor-electrolyte junctions have been first proposed in the 1950's by G*ä*rtner [23] and applied by Butler [24] and Ginley [25] to crystalline tungsten trioxide and iron titanate photoelectrodes. These models are based on the two prevailing mechanisms of charge collection of minority carriers (holes in n-type semiconductors), i.e. by migration, in case of electric field inside the space charge layer, and by diffusion, when charge generation occurs outside the depletion layer. Minority carriers generated within a specific distance from the surface can reach the surface or the border of the depletion region, from which they are successfully swept, giving rise to photocurrent and chemical reactions at the surface of the semiconductor. In particular, the mentioned distance is called diffusion length L ($\mathrm{L} = \sqrt{2D\tau}$, assuming the diffusion along a cartesian coordinate normal to the surface) and it is dependent on the diffusion coefficient D and on the carriers lifetime τ.

The optimization of the charge separation kinetics with respect to recombination losses is crucial for realizing efficient photocatalytic systems. This is particularly important in case of nanostructured systems, where the small size of the nanocrystalline domains and their low doping level do not sustain a relevant depletion layer. Moreover, in a free electric field regime, charge separation events are mainly determined by the chemical nature of both the semiconductor surface and of the electrolyte, and by the different overpotentials for the oxidation-reduction reactions taking place at the semiconductor surface [20].

As reported above, when the photocatalyst is an n-type semiconductor, which is almost the exclusive case, it can be exploited as photoanode, since the photo-generated holes reaching the surface drive photo-oxidation reaction in the so-called anodic compartment of a photoelectrochemical cell, which is the subject of the next paragraph.

1.2 Photoelectrocatalysis and PEC cells: general concepts

1.2.1 A bit of history

Since the French scientist Edmond Becquerel [26] pioneered the photoelectric experiments in 1839, researchers and engineers have been infatuated with the idea of converting light into electric power or chemical fuels. The experiments were performed with liquid, not solid-state devices, in which illumination of solutions containing metal halide salt produced a current between two platinum electrodes immersed in the electrolyte. His research was motivated by photography. Daguerre immortalized the first photographic images in 1837 and Fox Talbot followed with the silver halide process in 1839. Thanks to different studies [27, 28, 29], the parallel between photography and photoelectrochemistry comes as a surprise to many chemists.

Some years later, the work of Brattain and Garret [30], and subsequently Gerischer [31] laid the foundations of the modern photoelectrochemistry, marking the change from mere support of photography to a thriving research direction on its own. Initially, the first detailed electrochemical and photoelectrochemical studies of the semiconductor/electrolyte interface were accomplished. Then, around the middle of the 20^{th} century, research focussed on two types of cells, whose operation principle is shown in Fig. 1.9.

The first type is a regenerative cell (Fig. 1.9 **a**), which converts light to electric power leaving no net chemical change behind. Photons, with energy greater than that of the band gap, generate electron-hole pairs, which are separated by the electric field present in the space charge layer. The negative charge carriers move through the semiconductor bulk to the current collector and the external circuit. The positive holes, instead, are driven to the surface where they are scavenged by the reduced form of the redox relay molecule R, oxidizing in: $h^+ + R \rightarrow O$. The oxidized form O is reduced back to R by the electrons that are returned into the cell from the external circuit.

The second type, named photosynthetic cell (Fig. 1.9 **b**), operates on a similar

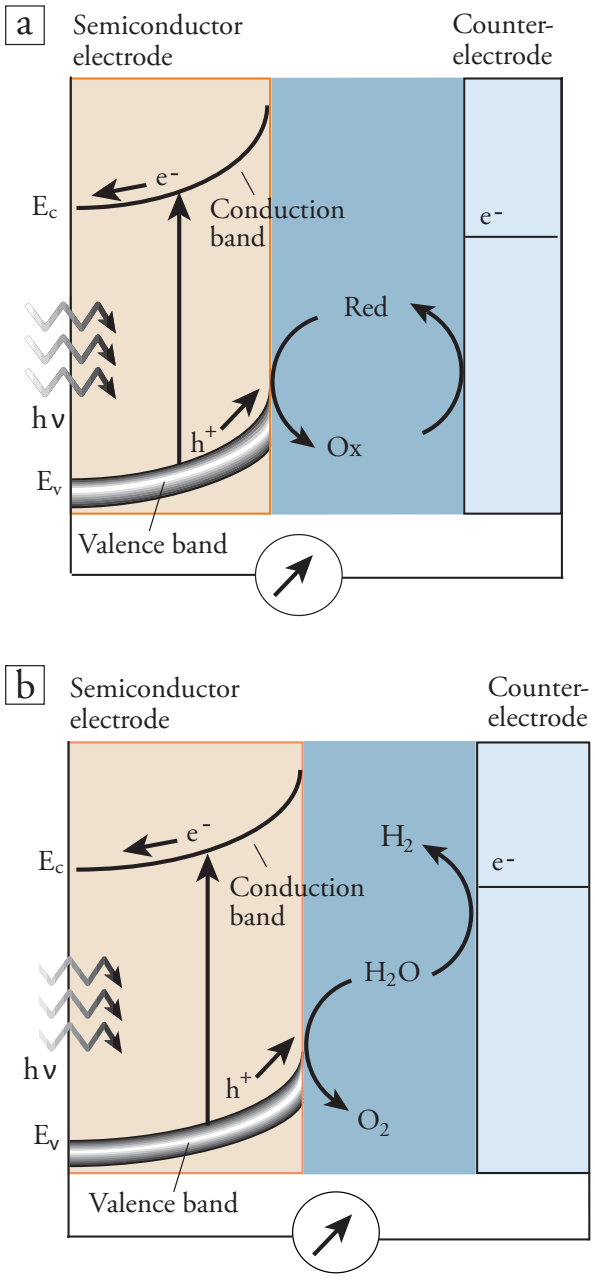

Figure 1.9: Operation principle of photoelectrochemical cells based on n-type semiconductors. **a**, Regenerative-type cell producing electric current from sunlight; **b**, a cell generates a chemical fuel, hydrogen, through the photo-cleavage of water. Adapted from [21].

principle except that there are two redox systems: one reacting with the holes at the surface of the semiconductor electrode and one reacting with the electrons entering the counter-electrode. In the shown example, water is oxidized to oxygen at the semiconductor photoanode and reduced to hydrogen at the cathode (the second electrode), obtaining the cleavage of the water by sunlight [21].

Almost fifty years later, in 1972, Fujishima and Honda produced the most celebrated scientific publication on photoelectrochemical cells [32], a work describing the photocatalytic water splitting in a PEC cell using a rutile—a mineral form of TiO_2—single crystal semiconductor electrode. In this work, Honda and Fujishima described a novel type of photoelectrochemical cell able to decompose water with visible light. The working principle of a photoelectrochemical cell is shown below.

1.2.2 Operating principle

The combined use of photocatalysis and electrochemistry gives rise to the photoelectrocatalysis, which can be employed for wastewater treatment with several advantages with respect to the two disciplines used separately. In the previous years, the photocatalytic hydrogen production by photodegradation of organic wastes has been shadowed by the more popular idea of water splitting. In fact, the two matters have been studied in parallel while the basic photocatalytic setups are similar [33]. In particular, the essential setup of a PEC cell exploits a n-type semiconductor as photoanode (or a p-type as photocathode) connected to a metallic cathode (or anode) (Figure 1.10, a and b).

The photoanode includes the photocatalyst, which, in case of a n-type oxide semiconductor, is the negative electrode from which oxidation reactions take place. On the other hand, the cathode consists of the electrocatalyst that facilitates the transfer of the electrons from the cathode to the liquid phase, through which reduction interactions take place. Both electrodes are immersed into an electrolytic solution with a defined pH in order to increase the conductivity. During the process of water cleavage, the photons are absorbed by the photoanode generating $e^{-}h^{+}$ pairs. The holes can oxidize the photodegradable substances present in the electrolyte liberating hydrogen ions that diffuse in the liquid phase. Then, the hydrogen ions diffuse from the anodic compartment to the cathodic one by an ion-transport membrane. In the meanwhile, the electrons are channeled through an external circuit toward the cathode where the reduced hydrogen ions produce hydrogen molecules.

The process that occurs between water in contact with the photo-generated electrons and holes is the photoelectrolysis of water, the also so-called water splitting. The chemical semi-reactions for water oxidation (Eq. 1.11) and reduction (Eq. 1.12) are

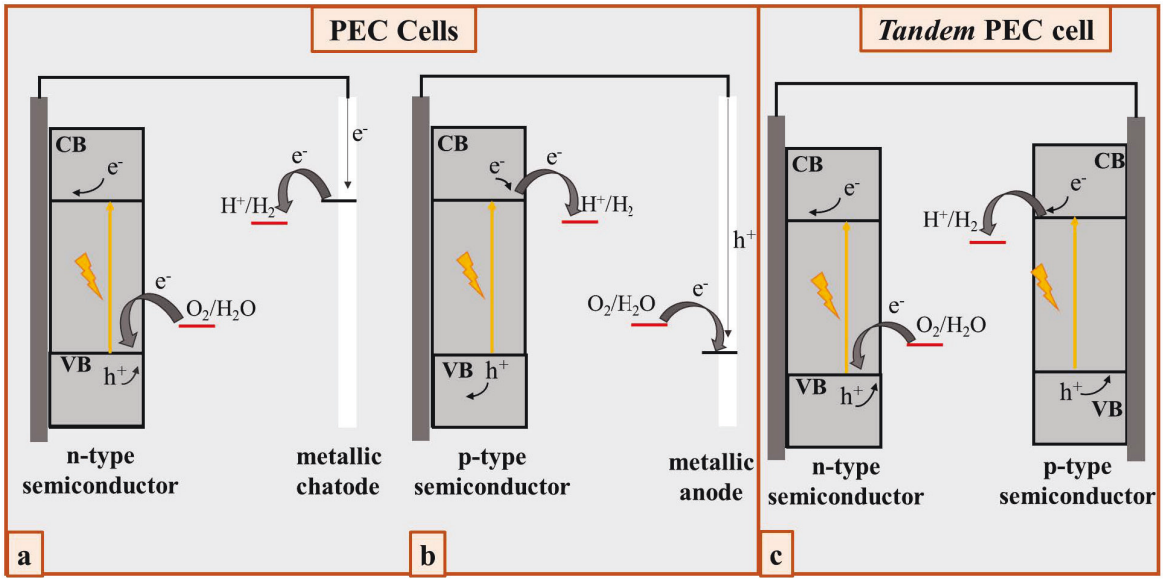

Figure 1.10: Schematic representation of PEC cells using a (a) n-type and a (b) p-type semiconductor electrode connected to a metallic counter electrode in an electrolyte solution and c) a n-type connected with a p-type electrode (tandem cell)

shown below:

$$2H_2O + 4h^+ \rightarrow O_2 + 4H^+;\ E^0 = 1.23V\ vs\ NHE; \tag{1.11}$$

$$4H^+ + 4e^- \rightarrow 2H_2;\ E^0 = 0V\ vs\ NHE. \tag{1.12}$$

Therefore, the overall reaction for the cleavage of water is shown in Eq. 1.13.

$$2H_2O \rightarrow O_2 + 2H_2;\ \Delta E^0 = 1.23V\ vs\ NHE. \tag{1.13}$$

According to this reaction, the ideal minimum energy required for the water splitting is equal to the energy difference between the oxygen and the hydrogen evolution potentials. This energy corresponds to the so-called Gibbs free energy, that is $E^0 = 1.23$ eV at room temperature [20]. However, due to the requirement of multiple transfer of electrons and protons, to make the reaction to take place, there is an excess, called overpotential, with respect to the theoretical energy. Therefore the minimal energy for water cleavage is 2.0–2.2 eV.

Although the efficiency of the photocatalytic effect is effective also with no external action, it extensively increases when the semiconductor is externally biased. What happens in this configuration is that the charge carriers drift accordingly to the external

electric field, reducing the chance of recombination. Therefore, the carriers accumulate on the surface depending on the applied field: the result is the net reactivity of the catalyst [34]. By bias is meant an external electric potential, which is added between the two electrodes, in order to increase the electromotive force driving electrons from anode to cathode.

Among the proposed various possibilities of additional bias, the most notable ones are those where the additional voltage is provided by renewable energy devices like photovoltaic cells [35] creating the so-called photoelectrode/photovoltaic (PEC/PV) tandem cell. In this way, this photoelectrochemical water splitting setup is undoubtedly a promising technology to harvest and store the abundant and free solar energy into hydrogen fuel, fulfilling the requirement of high energy for spontaneous water splitting under photo-illumination.

The first PEC tandem device was reported for photo-driven water splitting by Khaselev and Turner in 1998. It was composed of sophisticated and expensive p-type gallium indium phosphide (GaInP) photocathode, gallium arsenide (GaAs) solar cell and platinum (Pt) anode [36]. The typical arrangement of a tandem cell consists in a n-type semiconductor electrode connected with an appropriate p-type electrode as shown in Figure 1.10, c. A tandem cell is a frequently used configuration for unassisted overall water splitting because of the advantages that each component are tied together to form a highly efficient integration. Promoting the performance of a stand-alone semiconductor and finding new materials, coupled with an optimized configuration, are future steps for the practical application of tandem PEC cells [37].

Indeed, the main goal in the photoelectrochemical field consists in finding cheap, easy to manufacture and stable material in order to allow for a large electrochemically active surface, effective light harvesting, and reasonably good charge transport and collection efficiencies, all factors contributing to enhance the overall efficiency of the electrode. The next paragraph will introduce some fundamental parameters that are studied to improve a PEC cell efficiency.

1.2.3 Important parameters

In literature, the efficiency calculation of PEC cells has found some difficulties. Indeed, while the efficiency of a photovoltaic device is simply the ratio between the electric power output of the device and the light power incident on the device, in case of PEC cells the measurement of the efficiency is more complicated. The reason arises from the fact that, in addition to the energy of the exciting radiation, there is the necessity to take into account the effective output energy related to the produced fuel, the chemical

energy liberated by the photo-degradable substance, and the energy input by an applied bias [33].

The properties of the current-voltage (I-V) behaviour in a semiconductor electrode at equilibrium condition with the electrolyte can be examined by:

$$I = -I_0[exp\,(-\frac{eV}{kT}) - 1], \tag{1.14}$$

where V is the external bias and I_0 is the exchange current at equilibrium, which is dependent on the material characteristics and the redox couple. Equation 1.14 predicts that for V<0 (forward bias), the current is exponentially dependent on the voltage, but it is essentially independent from when V>0 (reverse bias). This equation, where the current flow predominates in one direction under an applied bias, is called rectification and it is a typical characteristic of an electrical diode. Therefore, the equation is generally called diode equation.

As mentioned in Paragraph 1.1.1, inside a semiconductor under illumination, the minority carriers travel along the surface, giving rise to the charge transfer reactions, while the majority carriers move into the bulk. This phenomena creates a photocurrent. Such a migration also induces an inverse potential in the electrode, called photo-potential, which reduces the potential drop across the space charge layer. When the photo-potential equals the difference between the electrode dark potential and the band potential, the band bending disappears, and an applied potential is needed to achieve a photocurrent. To describe the current-voltage behaviour under light condition it is convenient the partition of the current into two separate components: one that originates from majority carriers and one from minority carriers. The concentration of photo-generated majority carriers is usually small compared to that present from the thermal ionization of dopants atoms, so they should exhibit a I-V characteristic curve that is well described by the diode equation. On the other hand, illumination generally produces a substantial change in the concentration of minority carriers. If the electric field is so strong that all the photo-generated minority carriers are separated and then collected, the minority carrier current is approximately equal to I_{ph} (the photon flux absorbed by the semiconductor multiplied by the charge on an electron e^-). The net current can be obtained by adding together, with the appropriate sign, the majority and minority carrier components [16]:

$$I = I_{ph} - I_0[exp\,(-\frac{eV}{kT}) - 1]. \tag{1.15}$$

Eq. 1.15 corresponds to the diode curve with an offset equal to I_{ph} over the voltage range of interest (Figure 1.11).

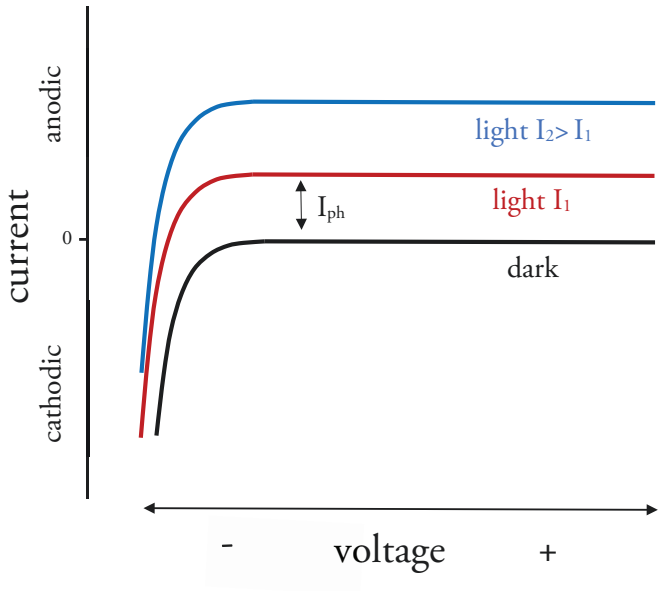

Figure 1.11: Current-voltage curve for an n-type semiconductor in dark condition (black line) and under two different illumination intensities (red and blue lines)

In order to better understand the efficiency of the photoanodic response, the Incident Photon to Current Conversion Efficiency (IPCE)—or External Quantum Efficiency EQE—can be introduced. It measures the effectiveness of a cell to convert the incident photons of a monochromatic radiation into electric current. IPCE depends on three fundamental processes involved in photoelectrochemical cells: the photon absorbance, defined as the fraction of electron-hole pairs generated per incident photon flux (η_{e^-/h^+}); the charge transport to the solid-liquid interface ($\eta_{transport}$), and the efficiency of the of interfacial charge transfer ($\eta_{interface}$). If the counter electrode does not limit the current flow through the circuit, then IPCE can be defined as:

$$IPCE = \eta_{e^-/h^+} \cdot \eta_{transport} \cdot \eta_{interface}. \tag{1.16}$$

The generation of electron-hole pairs is usually equal to one, while the probability of the electron or hole transfer across the solid-liquid interface is generally not unitary, because the interfacial charge transfer kinetics are often sluggish. The charge transport to solid-liquid interface is a limiting process too and depends on the effective charge mass in the semiconductor bands, which is a property connected with the transport speed. In other words, IPCE corresponds to the ratio between the number of electrons (n_e) flowing in the external circuit and the number of photons ($n_h\nu$) striking on the photoanode as shown in Eq. 1.17:

$$IPCE(\lambda) = \frac{n_e}{n_{h\nu}} = \frac{hcJ_{sc}}{e\lambda P}, \tag{1.17}$$

where c is the speed of light, e the electron charge—and their ratio is equal to a constant 1.24×10^3 (V m)— J_{sc} is the short-circuit photocurrent density ($A\,m^{-2}$), λ the photon wavelength (m), and P the radiant power density ($W\,m^{-2}$) at wavelength λ [15]. Recording IPCE at different wavelength give the possibility to judge the effectiveness of the cell with respect to the spectral response of a photocatalyst. The IPCE value is expected to varies between 0 and 1. Frequently, the IPCE is expressed in %, so IPCE% is expected to vary between 0 and 100.

Since not all the incident photons are absorbed by a cell, a percentage of them passes through the cell or is reflected by the surface. The ratio between the number of charge carriers produced by the cell over the actual number of photons absorbed by the cell is expressed by the Internal Quantum Efficiency (IQE). For its nature, IQE is expected to be a larger number than EQE but it is also included between 0 and 1.

Another efficiency expression equivalent to EQE for a PEC cell can be calculated by the following Eq. 1.18, taking into account of the effective output energy related to the produced fuel:

$$\eta = \frac{\Delta G^0 \cdot R}{P}, \tag{1.18}$$

where ΔG^0 is the standard Gibbs energy for the fuel formation multiplied by the rate R in moles/second, and divided by the incident radiation power. If instead of ΔG^0 the corresponding potential is used assuming a 100/Faradaic Yield for the products of interest, the Eq. 1.18 becomes:

$$\eta = \frac{E \cdot J}{P}, \tag{1.19}$$

where $E = \Delta G^0/nF$, n is the number of electrons involved in the fuel formation reaction, and F is the Faraday constant, i.e. 96485 C/mol, and J is the current density involved in the decomposition process [33]. In case of water splitting, $E = 1.23\,eV$. When a bias voltage V_{bias} is applied, we can talk about Applied Bias Photon to current Efficiency (ABPE) defined as Eq. 1.20:

$$ABPE = \frac{J \cdot (1.23 - V_{bias})}{P}. \tag{1.20}$$

All the discussed parameters are useful to study and to understand a possible improvement of a PEC device due to a better efficiency of the photocatalyst.

1.3 Applications: prototypes at the state of the art

Photocatalytic solar systems

Organic micropollutants like persistent organic pollutants (POPs), herbicides, and pesticides are compounds that have been found at relatively high contents in the aquatic environment. These pollutants have increased the toxicity levels in water. Presently, the most common wastewater treatments are based on a combination of mechanical, biological, physical and chemical processes such as filtration, flocculation, chemical or biological oxidation of organic pollutants. The common problem of the current conventional methods for water treatment is represented by the inefficiency to remove toxic and bio-recalcitrant organic compounds (BROCs). Differently, the electrochemical processes, in particular AOPs, implement clean and effective techniques for the direct or indirect generation of highly reactive transient chemical species (e.g., superoxide, peroxide, hydroxyl radical) to convert BROCs into biodegradable compounds [38]. All the AOPs sectors are nowadays under intense investigation from the scientific community. Nevertheless, solar photocatalysis currently plays a minor role, since the growth of research focusing on solar systems applied therein has shown a smaller increase compared to overall photocatalysis research, as shown on Figure 1.12.

This argumentation points out the opportunity to dedicate efforts to this clean tech-

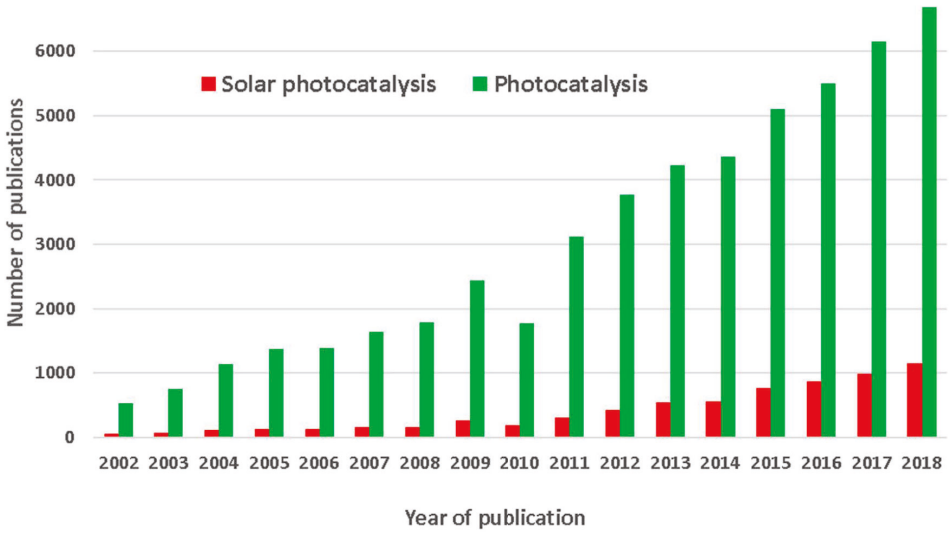

Figure 1.12: Publications on photocatalysis compared to those on solar photocatalysis. Data from Scopus comparing "photocatalysis" with "solar and photocatalysis". Adapted from [38].

nology connected to the abundant solar energy source, in particular, making use of systems based on solar collectors. These latter may be concentrating or non-concentrating systems. The advantages of concentrating systems consist in:

- a potentially small reactor tube area, thus allowing for easier handling of the wastewater;
- a limited reactor area, which is also more compatible with supported catalysts and turbulent flows;
- the possibility of controlling the evaporation of the volatile compounds.

Furthermore, it has been estimated a degradation rate improvement due to an increase of the radiation intensity within given limits [38]. Parabolic-trough concentrators (PTCs) are the most promising type of concentrating solar reactors that is proved to be effective for wastewater treatment. PTCs can be defined as parabolic reflective surfaces that concentrate the sun radiation on a focal line, where the wastewater flows in a tubular reactor [39]. The concentrating system is generally constructed by bending a sheet of reflective or highly polished material into a parabolic shape and can also present tracking systems with one or more axis to follow the sun position during the day [40]. In Figure 1.13 a schematic drawing of a PTC is shown.

The starting point for the use of solar collectors in wastewater remediation can be traced back to parabolic systems, originally developed for thermal energy applications, and then adapted in 1989 in Albuquerque, NM, USA for water purification. Immediately afterwards, in 1990, a dedicated facility started operations at the *Plataforma Solar de Almeria*, Spain. Ten years later, dedicated research on wastewater treatments started to be effectively performed [41].

Although the solar water treatment have produced significant interest in research, they have not yet reached commercialization; there are only a few examples of medium to large-scale solar wastewater processing plants in industry. However, recent literature results demonstrate that solar wastewater treatment has the potential to be successfully employed both as cheaper and more environmentally-friendly alternative to conventional processes, or integrated in existing plants, thereby increasing efficiency and reducing operating costs [38]. Certainly, further research towards industrialization is needed both from the point of view of photocatalytic systems, and in case of photoelectrochemical systems.

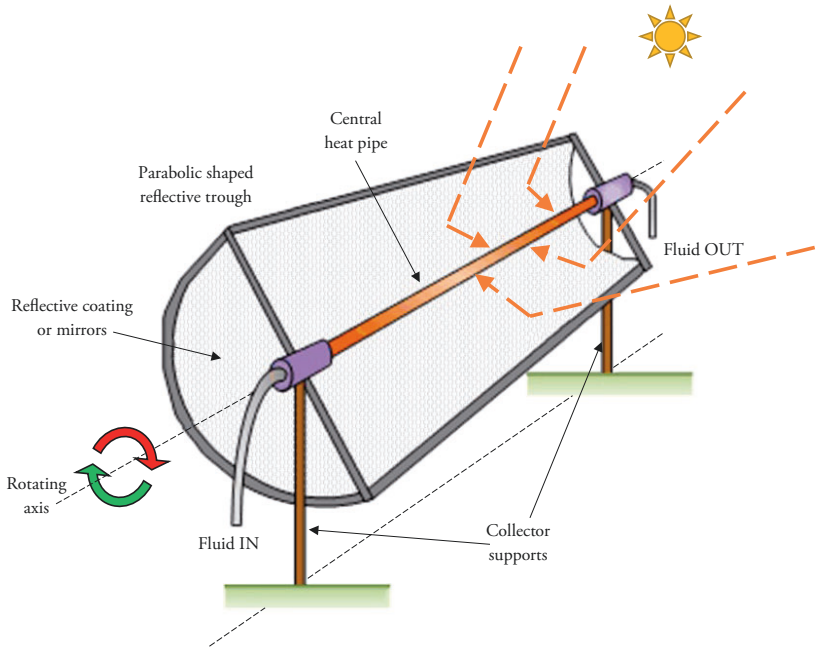

Figure 1.13: Schematic drawing of a parabolic through collector. Adapted from[38].

Photoelectrochemical systems

Starting from Honda and Fujishima work, a lot of work has been done in this field [33], e.g. more than forty years of studies on photocatalytic degradation of organic substances, the development of new nanostructured photocatalysts, the optimization of material deposition and, in general, the progress of Materials Science in combination with the increasing awareness on the environmental issue. In addition to waste water treatment, the conversion of the solar radiation into useful forms of energy, such as electricity and hydrogen must be considered. Nowadays, the production of electricity and hydrogen by photocatalytic degradation of organic wastes in a photoelectrochemical cell is an attractive project with a double environmental benefit [33].

Following, the photoelectrochemical reactors for the water photoelectrocatalysis are described. In particular, the patent of Grätzel and Augustynski [42] and the patent of Keable et al. [43] are pointed out. The first one describes a Grätzel cell—for which Michael Grätzel has been awarded the 2010 Millennium Technology Prize—, i.e. a photoelectrochemical tandem system consisting of two cells electrically connected in series. The system allows the water separation process in hydrogen and oxygen through visible light. The photoactive material is a semiconductor oxide, such as WO_3 or Fe_2O_3 in contact with the aqueous solution. Such materials absorb radiation in blue

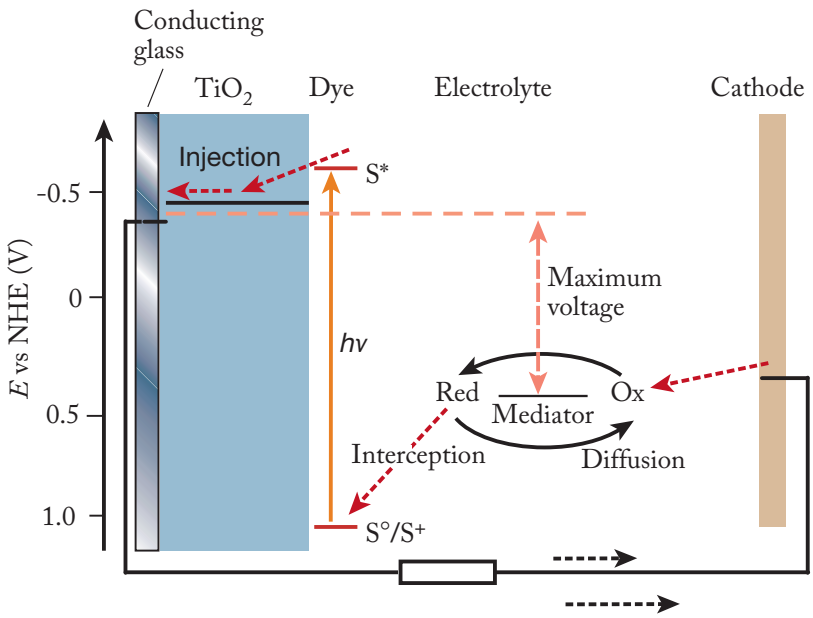

Figure 1.14: Schematic representation of a DSSC cell

and green wavelengths generating protons and oxygen from water. The red and yellow components of the solar spectrum, that are not absorbed by the photo-active material, are transmitted to a second photo-cell mounted in the direction of the incident light on the back of the first, comprising a Dye-Sensitized Solar Cell (DSSC) in TiO_2. A DSSC is a low-cost solar cell belonging to the group of the thin film solar cells. In Figure 1.14 a schematic representation of a DSSC Grätzel cell is presented.

The second patent describes a photoelectrochemical system for the division of an electrolyte into hydrogen by using of light. It is composed by two electrically connected cells. The first includes a photo-active electrode consisting of a glass substrate covered by a conductive layer and a WO_3 film: the cell is operative when put in contact with the electrolyte, absorbing light and producing charge carriers. The second cell involves the use of photovoltaic cells in Si, instead of DSSC, increasing the voltage, improving durability and showing itself less expensive.

To conclude, lab-scale experiments carried out with reactor systems [9] and pilot scale plants have been demonstrate the efficiency of the electrochemical oxidation processes but they have not yet reached commercialization. Indeed, the current scenario is based on the study of electrocatalytic activity and stability of electrode materials, the optimization of the reactor geometry, and hydrodynamics.

Starting from the characterization of the active materials—i.e. the photoanode electrodes—the projected and assembled solar devices are presented and discussed in

the following chapters. The realization of the described devices has been motivated by the necessity of developing stand-alone systems for wastewater treatment using solar energy.

CHAPTER 2

Oxide semiconductor photocatalysts

In the previous chapter, the fundamental concepts about photocatalysis and its applications have been shown, to better understand the resources of AOPs in the field of wastewater treatment. As introduced, the investigation of different catalyst materials and the comparison between homogeneous and heterogeneous catalysis routes are also crucial points, and are, hence, object of intense discussion [38]. In particular, the heterogeneous catalysis makes use of a solid catalyst, which is activated by light immersed in the aqueous phase as well as in the gas phase, while, for the homogeneous process, the catalyst and the reactant are in the same phase. In the past years, the heterogenous catalysis gained considerable interest in comparison to the homogeneous one due to the disadvantages of the latter. Indeed, the complicated separation process, the high cost, and the technical impracticability of the involved products, do not make possible the use of homogeneous catalysts, such as metal salts, in the AOPs [17].

Differently, the semiconductors used as catalysts are very versatile materials because of their attractive properties, such as optical transmittance, uniformity, low resistivity, mechanical hardness, stability to heat treatment, hydrophobic and piezoelectric behaviour. Therefore, they become a suitable candidate for devices such as for gas sensor application, Li-ion batteries, photovoltaic, supercapacitor, light emitted diodes, display devices and solar cell [44], DSSCs (Dye Sensitized Solar Cells) for electrochemical water splitting [45], antibacterial [46], antifogging, and self cleaning.

The difference of the photocatalytic reaction from the classic catalysis consists in the photonic activation of the catalysts by the incident radiation, instead of the thermal one. Indeed, as introduced in the Section 1.1, in heterogeneous photocatalysis processes the photo-catalyst is generally a semiconductor material that is activated

by absorption of UV or UV-visible photons. Several semiconductor have been investigated as catalysts, as reported in Table 1.1. Among these, titanium dioxide (TiO_2) has received the most investigation effort, since its good photocatalytic properties under UV radiation were already known in the early 1970s. However, novel types of catalysts focused to solar applications are rapidly emerging, especially those which are able to efficiently absorb visible light [38]. Indeed, the charge carriers resulting from the absorption of the visible light can be used to drive redox reaction at the semiconductor-electrolyte interface, triggering the direct conversion of solar energy into chemical one. Considering the photocatalytic wastewater treatment based on photoanodes, the photogenerated holes have high oxidation potential able to decompose most kinds of organic waste, even at trace level, while electricity or fuels production can be achieved by providing a suitable cathode to attract photogenerated electron from the external circuit. Indeed, many visible-light-responsive photoelectrodes, such as $Ag/AgCl/TiO_2$, $CdS/ZnS/TiO_2$, WO_3, $BiVO_4$, $/WO_3$, and $\alpha - Fe_2O_3$, were studied and developed to improve absorption and energy output [47, 48, 49].

In this chapter, the oxide semiconductors, which represents the active material of the realized photocatalytic devices, are introduced. In particular, the discussion will be focused on two of the oxide semiconductors—the titanium dioxide (TiO_2) and the tungsten trioxide (WO_3)—considered as photoanode materials. The realization processes and the characterization of different semiconductor materials will be pointed out, also studying, in case of TiO_2, the characterization with nitrogen doping.

2.1 Oxide semiconductors and methods to improve their efficiency

As already introduced, in order to have redox reactions without applied bias, the potential of the photogenerated electrons must be more negative than the H^+/H_2 reduction potential, and the potential of the photogenerated holes must be more positive than O_2/H_2O oxidation potential. This request is not verified for many of the most common semiconductors able to absorb visible light. Indeed, many of them have a band gap greater than 2.3 eV, ideally suitable for the splitting of water with a single photon, but they do not possess a sufficiently negative conduction band to support the unassisted production of hydrogen. In Figure 2.1 the band positions of several semiconductors in aqueous electrolyte are shown. The lower edge of the conduction band (red colour) and the upper edge of the valence band (green colour) are presented along with the band gap in electron volts. The energy scale is indicated in electron volts using either

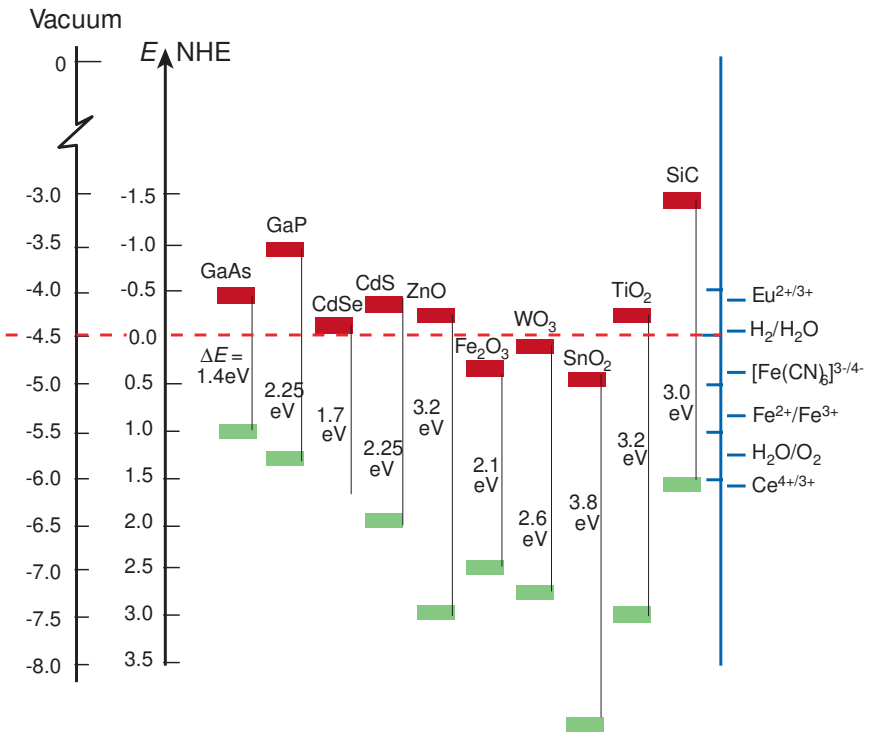

Figure 2.1: Band positions of several semiconductors in aqueous electrolyte at pH 1. Adapted from [21].

the Normal Hydrogen Electrode (NHE) or the vacuum level as a reference. On the right side (in blue) the standard potential of several redox couples—in particular, the H^+/H_2 and O_2/H_2O couples—are presented against the standard hydrogen electrode potential.

Among the displayed oxide semiconductors, TiO_2, WO_3 and α-Fe_2O_3 have attracted a considerable interest in photocatalysis and in photoelectrochemistry due to their chemical and photochemical stability, relative abundance, environmental safety, and band gap. The latter is suitable for the production of charge carriers with sufficient free energy to drive a variety of redox reactions [50]. Following, the features of TiO_2 and WO_3 are discussed, particularly considering the possible techniques to improve their efficiency.

Doped TiO_2 for visible light photocatalysis

Following the Fujishima and Honda's work for water photolysis in a PEC cell, rutile TiO_2 has been the first catalyst to be used as photoanode material for the studies of water cleavage by radiation, because of its outstanding stability and active features.

Indeed, as shown in Fig. 2.1, the TiO_2 satisfies the required conditions for the activation of the redox reactions, without applied bias. However, the Fujishima and Honda's experiment introduced a chemical bias by using two solution having different pH values within the two PEC compartments. A basic solution was used at the anode, and an acidic one at the cathode. According to the Nernst equation, the resulting bias E was thus:

$$E = 0.059V\Delta pH, \tag{2.1}$$

considering the standard electric potential of the reference electrode equal to 0.

The wastewater treatment efficiency and power generation capacity of the TiO_2-based PEC cells that exploit solar radiation are restricted by the wide band gap (3.2 eV) of the electrode. Indeed, these electrodes show limited applications under visible light radiation because of its poor light absorption ability and low charge separation efficiency under normal reaction condition [51]. Therefore, in literature many attempts have been used to extend the photocatalytic activity of the TiO_2 toward longer wavelengths, such as surface modifications, heterojunctions, metal and non-metal doping [52], surface sensitization by organic dyes and metal complexes.

Generally, among the possible methods to enhance the semiconductor performance, doping is particularly employed. Doping consists in a modification that reduces the band gap between the valence band and the conduction band by adding impurities in an otherwise pure semiconductor. Each type of dopant has a unique impact on the crystal lattice of the semiconductor. Metal and non-metal doping enhances the photo-responsiveness of the photocatalyst to the visible region by creating new energy levels—also called impurity states—between the valence band and the conduction band. These new levels reduce the band gap, and the excited electrons are shifted from the impurity state to the conduction band. Metal dopants like Co, Cr, Cu, Zn, Mo, Mn, Fe, Ni, give rise to a new band below the conduction band whereas, non-metals like N, P, F, Si, S, Cl, Se, Br, create a new band above the valence band [12]. The doping process helps to avoid charge recombination by enhancing the electrons trapping [53]. As a consequence, the photocatalytic activity increases with respect to the bare oxide semiconductor.

In addition to the above-mentioned techniques, a widely used methodology is the deposition of noble metal ions (Ag, Au, *etc.*) on the TiO_2 surface, where the noble metal is exploited as a light harvester, in order to improve light absorption in the visible region [54]. The disadvantages in exploiting noble metals are the toxicity, which poses health hazard, and the high costs, i.g. in case of silver and gold, in addition to photocorrosion of the metal-loaded photocatalyst during reactions. A possible solution is represented by the replacement of the traditionally doped or metal-based TiO_2 with

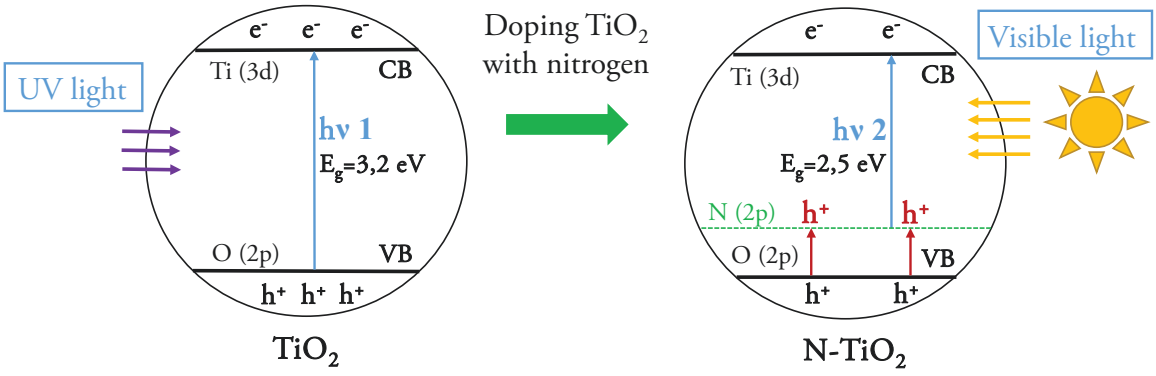

Figure 2.2: Schematic energy level of nitrogen doped TiO_2. Adapted from [54].

non-metal doped photocatalysts [55]. There are three possibilities thanks to which a non-metal can react with the oxide semiconductors. Firstly, the dopant could hybrid with the oxide of the photocatalyst. Secondly, the dopant could replace the oxygen site and thirdly, the dopant is added in a oxygen deficient site, which acts as a blocker for re-oxidation. The size of the dopant plays an important role in the substitution modality of oxygen within the photocatalyst. For example, Guo et al. [56], studying the trends in non-metal doping of the $SrTiO_3$ surface, showed that the smaller radius species, like C, N, or F, substitute the O atom in the TiO_2 terminate surface whereas, larger radius species, such as P, S, Cl, S and Br, replace the O in the SrO-terminated surface.

Among non-metals, nitrogen doping of TiO_2 is quite encouraging because of its comparable atomic size, small ionization energy and stability. The incorporation of nitrogen into the TiO_2 lattice leads to the formation of a new mid-gap energy state, i.e. the N 2p band above the O 2p valence band, which decreases the band gap of the TiO_2 to ~ 2.5 eV and shifts optical absorption to the visible light region [57]. Therefore, it is possible for the electrons to migrate from the valence band to the conduction band upon absorbing visible light (Fig. 2.2).

The electrons photogenerated in the CB accumulate on the catalyst surface, and are then scavenged by oxygen molecules dissolved in water, to yield highly oxidative species, such as superoxide radical anions and hydroxyl radicals, which are responsible for the degradation of the organic pollutants. In the same way, the generated hole in the VB are scavenged by OH^- ions.

N-doped TiO_2 can be easily synthesized by different routes, such as the sol-gel method, plasma or ion implantation, solvothermal, ball milling, sputtering, hydrothermal, and the direct hydrolysis of organic/inorganic salts. In this work, electrodes with

bare and N-doped TiO_2 based on nanosol routes were realized to study the possible efficiency improvement via to the visible light absorption.

WO_3 surface nanostructuration

Tungsten oxide is the most investigated and used material for electrochromic devices, in which coloration and bleaching can be reversibly obtained by an electrochemical process. According to the deposition conditions, it is possible to obtain different polymorphs such as monoclinic (> 17–330°C), orthorhombic (300–740°C), and tetragonal (>740°C) WO_3 [58].

Differently from wide band gap oxide semiconductors, tungsten trioxide is a promising photoanode material because of its high resistance against photocorrosion in aqueous solutions [59, 60] and its band gap of 2.5–2.7 eV that can absorb $\sim$ 12% of the incident sunlight. Moreover, WO_3 shows a longer hole diffusion length ($\sim$ 150 nm) than both α-Fe_2O_3 (2–4 nm) and TiO_2 ($\sim$ 100 nm), and good electron transport properties [61]. Nonetheless, WO_3 shows some limitations, such as its slow charge transfer at the semiconductor-electrolyte interface, its gradual loss of photoactivity because of the formation of peroxo-species on the surface, and its rapid charge recombination, caused primarily by surface defect sites [51].

Therefore, different strategies to overcome some of these drawbacks have been reported, including the synthesis of nanostructured WO_3, such as:

- nanoflakes and nanowires, to increase the surface area and facilitate the charge transfer [62];
- surface modification with co-catalysts to improve oxygen-evolution reactions [63];
- overcoating with metal oxides (e.g. Al_2O_3) or treatment with hydrogen to eliminate the accumulation of surface peroxide [64];
- enhancement of charge separation through coupling with other semiconductors (e.g.$BiVO_4$) [65].

Among these possible solutions, the nanostructuration of the material can be certainly an advantage, since the increased surface roughness may facilitate the penetration of the electrolyte, enhancing the photoinduced hole injection from the WO_3 to the electrolyte and facilitating the interfacial charge separation. In addition, the higher surface irregularities can reduce the bulk hole diffusion path, leading to a general improvement of the photoelectrode performances. Nevertheless, this consideration should not be

easily generalized, since in nanoparticulate films the charge recombination in the illuminated regions becomes possible, due to the loss of the conventional space charge effects. Thus, finding a successful interfacial kinetic competition between charge transfer and recombination events turns to be mandatory [20].

The improved photoelectrochemical performances of nanocrystalline semiconductors are also analyzed by Grätzel [21] comparing the photoresponse of two dye-sensitized TiO_2 electrodes: a single-crystal and a mesoporous TiO_2 film, respectively. The IPCE (incident-photon-to-current conversion efficiency) value obtained with the single-crystal electrode is only 0.13% near 530 nm, where the sensitizer shows its maximum absorption, while it reaches 88% in case of nanocrystalline electrode. Similarly, the photocurrent in standard sunlight augments 10^3-10^4 times when passing from a single crystal to a nanocrystalline form. Moreover, although these studies achieved some improvements in photocatalytic performance, one of the most important parameters for practical applications, i.e. the stability of the photoanode, was still not addressed. Therefore, the development of more efficient methods to overcome the shortages of WO_3 is still urgent for the applications in PEC cells to efficient and stable wastewater treatment and power output.

In the next paragraphs and chapters, within the discussion on electrodes characterization and devices realization, the possible solutions about the efficiency improvement—carried out in this thesis work—will be proposed and analyzed.

2.2 TiO_2 vs N-doped TiO_2 electrodes

Due to their conductive, optical, and catalytical properties, the particles with nanometric size acquired a considerable importance in the photocatalytic applications. In this regard, colloidal nanosuspension (nanosol) started to collect success. A colloid is a solution that contains particles with sizes ranging between 1 and 1000 nm in diameter. The colloidal particles are typically much larger than molecules of the dispersing medium and have a surface area/volume ratio much higher than the bulk system, thus the surface has a significant role on the properties of the colloid itself [66].

In this section, the realization techniques and methods for the development of electrodes from bare and N-doped TiO_2 nanosols are presented.

2.2.1 Electrodes deposition: materials and methods

Each realized electrode consists in a 2.2 mm thick glass substrate covered by a deposited via spray-pyrolysis Fluorine-doped Tin Oxide (FTO) layer (Aldrich), which is used

as transparent—FTO shows a transmittance of 80-82% in the visible spectrum—and conductive film. The electrode substrates were obtained from the original slab by cutting and incising the glasses by means of a high-precision dicing machine (DISCO, DAD 3220). Above the FTO layer, the TiO_2-based catalysts were deposited at the laboratories of the Institute of Science and Technology of Ceramic Materials (ISTEC-CNR) in Faenza, Italy. For the electrodes realization, two different commercial TiO_2 and N-doped TiO_2 nanosols (Colorobbia, Italy) were diluted with deionized water to 2 wt%.

The N-doped nanosol was used at original commercial conditions, without modification, while the bare TiO_2 was treated with an ion exchange resin to increase the pH value. The resin was able to sequester Cl^- ions and release OH^- ions with a consequent increase in pH. Once the required pH value had been reached, the resin was removed by separation. The obtained pH value was 4.5 [67].

The particle size distribution of the nanosol was measured by Dynamic Light Scattering (DLS) through a Zetasizer Nanoseries (Malvern Instrument, Malvern, UK). This technique provides the hydrodynamic diameter of suspended particle, expressed as D50, which is the value of the particle diameter at 50% of the cumulative distribution. The DLS analysis also provides a polydispersion index parameter (PDI), ranging from 0 to 1, quantifying the colloidal dispersion degree. Their ζ potential—defined as the measure of the nanoparticles surface charge, which indicates how stable is the particle in the suspension system—was examined by an Electrophoretic Light Scattering (ELS) (Zetasizer Nanoseries). The analysis are shown in Table 2.1.

Following, the deposition technique is described. Firstly, the samples were washed in an ultrasound bath for 15 min with isopropyl alcohol and then dried in air. The TiO_2 films were deposited at room conditions (temperature and pressure) by dip-coating (Fig. 2.3), dipping them for 5 s in the colloidal nanosuspension, with a withdrawal at a constant velocity of 2 mm/s. Then, the coated samples were air dried, allowing the solvent (water) evaporation, and, subsequently, they were thermally treated to promote the adhesion to the substrate. The thermal treatment was carried out at 400 °C with a heating ramp of 2.5 °C/min and a permanence at 400 °C for 1h. The described

Table 2.1: Physicochemical characteristics of bare and N-doped TiO_2.

Nanosol	Diameter(nm)	PDI	ζ potential(mV)
TiO_2	25.3±0.3	0.4	39.8±1.5
$N-dopedTiO_2$	98.6±2.5	0.2	10.6±0.7

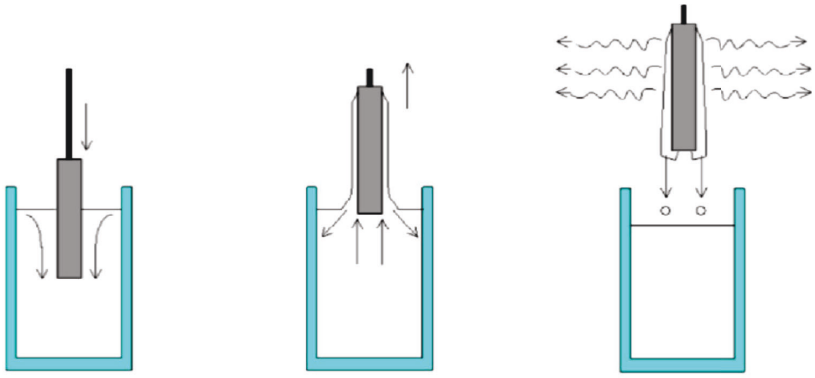

Figure 2.3: Schematic representation of dip-coating method.

procedure was repeated 5 times to obtain a thicker layer of the catalyst.

An electrode based on TiO_2 (following named sol-gel TiO_2) was realized as comparison sample in our laboratories using the sol-gel method for the precursor production, and the doctor-blading technique for the catalyst deposition. The sol-gel method was based on titanium isopropoxide (99,999%, Aldrich) as starting reactive, which, immersed in an alcoholic solution of butanol (99%, Aldrich), underwent hydrolysis in concentrated nitric acid (65%, Fluka) followed by Ti-O-Ti bond configuration, finally resulting in the formation of nanoparticles. After the precursor deposition via doctor-blading, the samples were annealed at 550 °C for 40 min in air conditions [68].

Layer analysis

In order to study the deposited-film thickness, SEM (Scanning Electron Microscope) analysis was carried out by using a Zeiss EVO 40 SEM with an electron beam of 20 keV. In addition, an Energy-Dispersive X-ray Spectroscopy EDS analyzed the chemical composition of the sample surfaces.

Figure 2.4 shows the EDS spectroscopy image of the bare TiO_2 electrode in cross section. The white section corresponds to the FTO conductive film, while the above gray layer corresponds to the TiO_2 film.

Similarly, 2.5 displays an image of the N-doped TiO_2 electrode. From the EDS analysis the presence of nitrogen in the coating layer is not verified. This can be attributed to an incorrect industrial synthesis.

In both cases of bare and N-doped TiO_2, the film thickness corresponded to ∼700 nm.

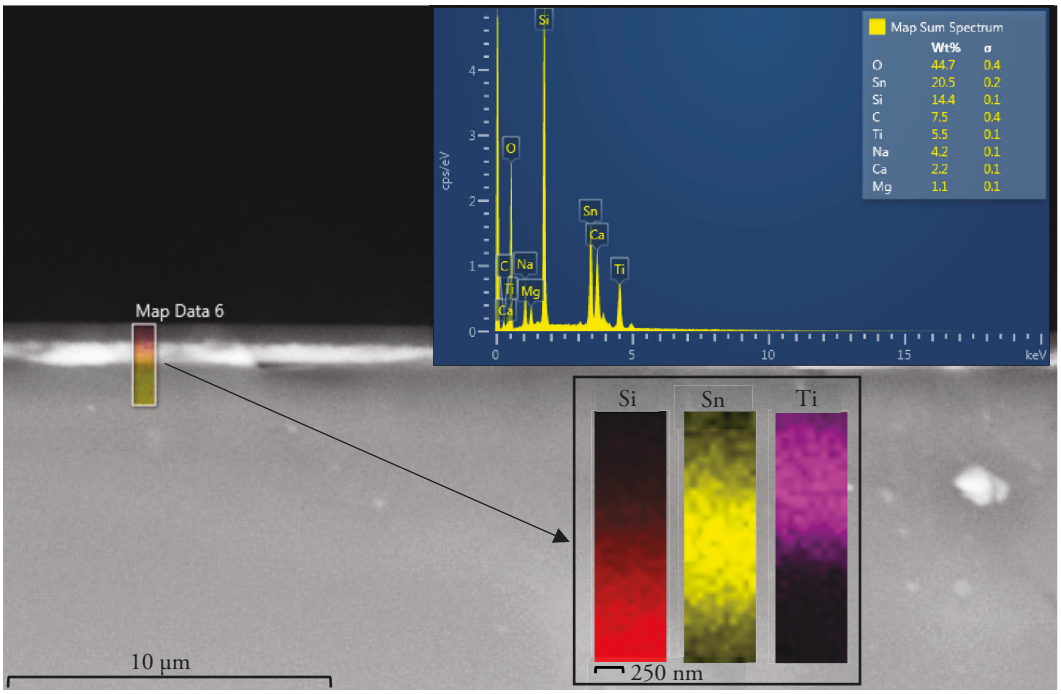

Figure 2.4: EDS spectroscopy of the bare TiO_2 electrode. Adapted from [69].

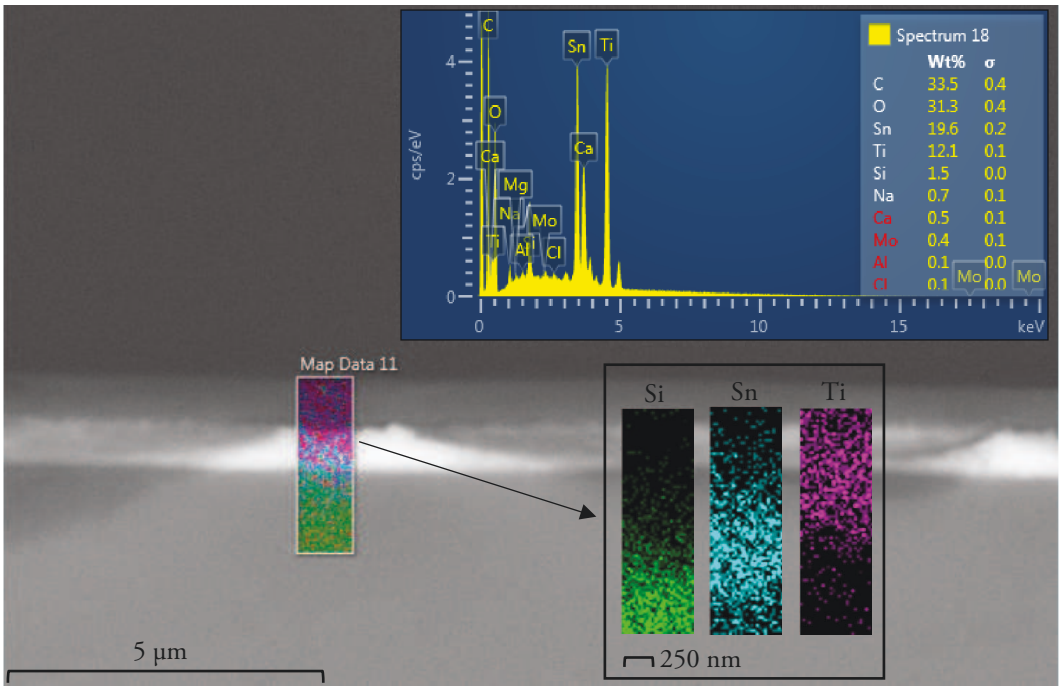

Figure 2.5: EDS spectroscopy of the N-doped TiO_2 electrode.

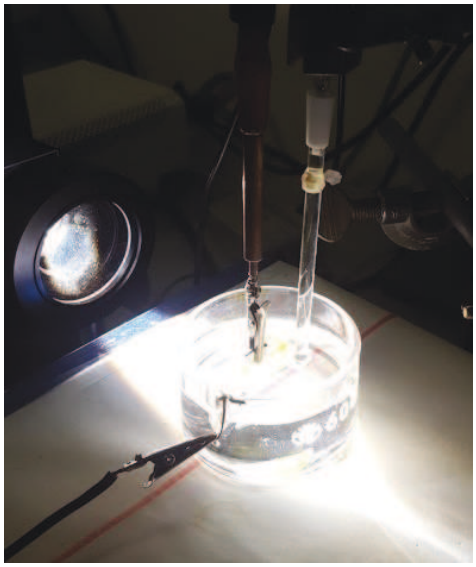

Figure 2.6: Experimental setup for the electrochemical characterization.

2.2.2 Electrochemical characterizations

The electrochemical characterizations were carried out by using the following experimental setup (Fig. 2.6):

- a Xe ABET LS 150W solar simulator providing AM 1.5 Air Mass conditions;
- an Autolab PGSTAT302N potentiostat;
- a Molectron Power Max 500 power meter, to measure the irradiance;
- the TiO_2 electrode used as working electrode;
- a Pt counter electrode;
- a Saturated Calomel Electrode (SCE), used as reference electrode;
- two conductive electrolytic solution, Na_2SO_4 0.5M or H_2SO_4 1M.

The Xe-lamp spectrum is shown in Figure 2.7. The 1.5 Air Mass filter was added to simulate the solar radiation conditions. The presence of the SCE as reference electrode corrected the drawbacks due to the ohmic drop, i.e. the portion of the potential difference between the working electrode and the counter electrode, which is spent to keep the current flowing into the cell, and which is given by the product of the cell resistance and the intensity of the circulating current. As a consequence, the real potential difference between the working and reference electrodes was obtained.

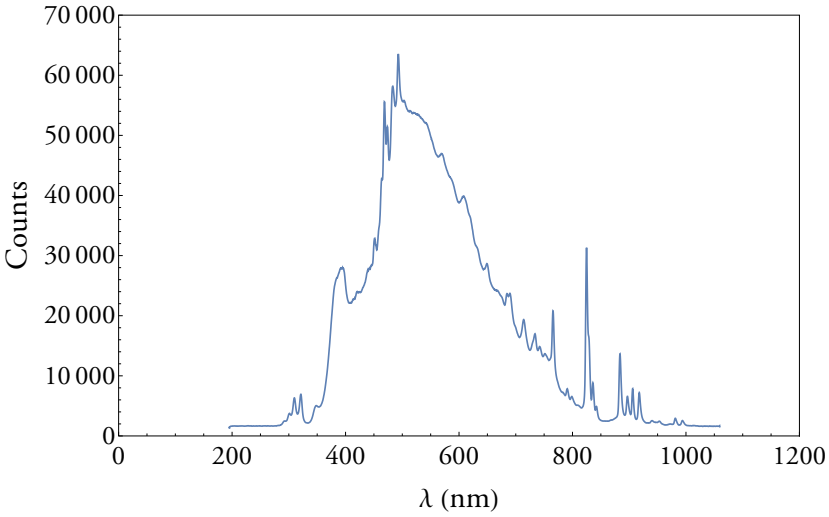

Figure 2.7: Xe-lamp spectrum.

The same experimental setup, with the addition of a high radiance monochromator (Applied Photophysiscs LTD, London, 1200 lines/mm, f:4, band pass 10 nm), was exploited for the photo-action spectra (IPCE vs λ) measurements under 1.5 V vs SCE potential bias (AMEL mod.552 potentiostat). Each test was conducted on the three TiO_2-based electrodes, the N-doped, the commercial ones, in comparison with respect to the sol-gel TiO_2.

Photocurrent test: results and discussion

The photocurrent tests were conducted via Cyclic Voltammetry (CV) evaluating the produced photocurrents of the three electrodes. The potential was cyclically varied between -0.5 V and 1 V. The measurements were performed in alternating dark-illumination condition and in illumination condition at 100 mW/cm^2. The graphs display the JV curves, from which it is possible to observe the photocurrent values of each electrode. The first Graph (Fig. 2.8) shows the reached photocurrent values in case of neutral environment (Na_2SO_4 electrolyte 0.5 M, pH 7). In case of commercial and N-doped TiO_2, the saturation photocurrent value (0.01 mA/cm^2) is reached at -0.2 V. The sol-gel TiO_2 electrode showed a double value of the photocurrent, and thus a better efficiency. Secondly, the Graph 2.9 shows the reached photocurrent values in case of acidic environment (H_2SO_4 electrolyte 1 M, pH 0). Also in this case, the commercial and N-doped TiO_2 showed a low value of the saturated photocurrent, which is reached at 0.2 V. Differently, the sol-gel TiO_2 electrode displays a 0.17 mA/cm^2 photocurrent, reacting to the higher H_2SO_4 electrolyte conductivity.

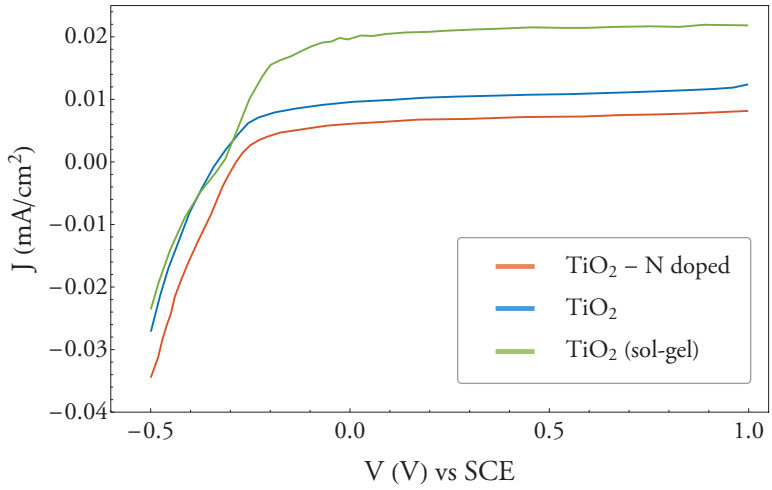

Figure 2.8: JV (V vs SCE) curves (100 mW/cm^2, AM 1.5 filter) in neutral (pH 7) Na_2SO_4 electrolyte 0.5 M, of N-doped (orange), commercial (blue), and sol-gel (green) TiO_2 electrodes

IPCE analysis: results and discussion

The IPCE measurements of the N-doped, the commercial, and the sol-gel TiO_2 electrodes are here presented, considering both the neutral and the acidic environments. Firstly, in the neutral environment (Fig. 2.10), a greater efficiency of the commercial TiO_2 is highlighted, while the N-doped electrode activity in the visible range does not

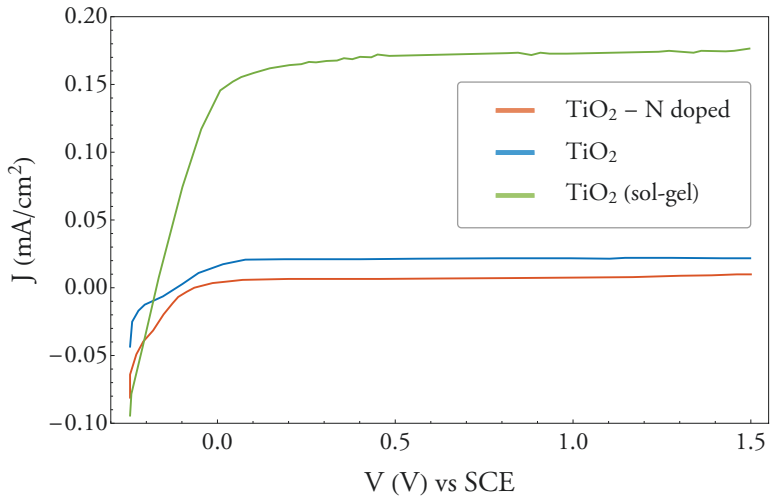

Figure 2.9: JV (V vs SCE) curves (100 mW/cm^2, AM 1.5 filter) in acidic (pH 0) H_2SO_4 electrolyte 1 M, of N-doped (orange), commercial (blue), and sol-gel (green) TiO_2 electrodes

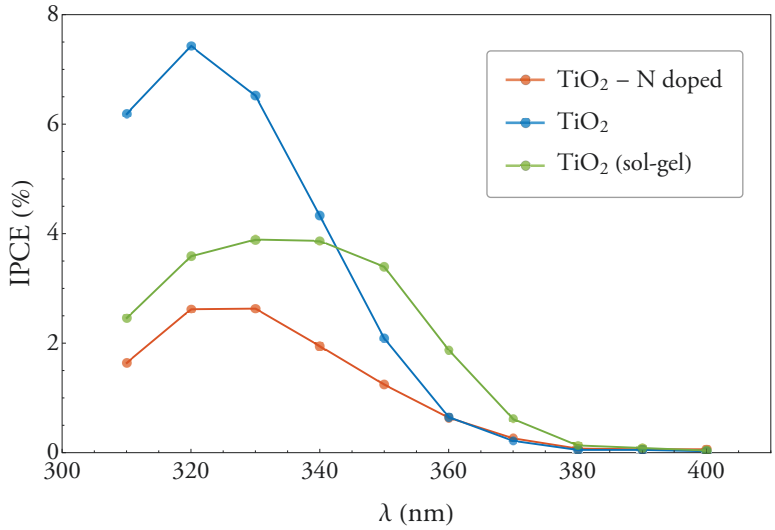

Figure 2.10: IPCE spectrum under 1.5 V vs Pt in neutral (pH 7) Na_2SO_4 electrolyte 0.5 M, of the N-doped (orange), the commercial (blue), and sol-gel (green) TiO_2 electrodes

appear.

When passing to the acidic environment (Fig. 2.11), the comparison electrode displayed a noticeably efficiency increase, according to the greater photocurrent value. Unfortunately, the N-doped TiO_2 electrode activity in the visible range did not appear, neither in acidic solution, probably because of the too thin thickness of the layer and also for reasons attributable to the industrial synthesis. Indeed, in the latter case an

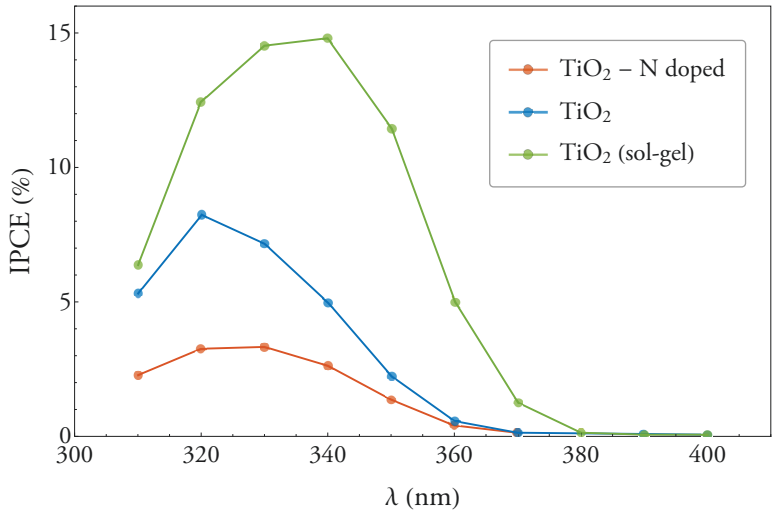

Figure 2.11: IPCE spectrum under 1.5 V vs Pt in acidic (pH 0) H_2SO_4 electrolyte 1 M, of N-doped (orange), commercial (blue), and sol-gel (green) TiO_2 electrodes

insufficient nitrogen doping could be carried out for the photocatalytic purposes.

2.2.3 Optical characterizations

The optical characterizations were carried out to study the absorbance/transmittance properties of the realized samples in bare and N-doped TiO_2. In this case, the experimental setup consisted in:

- a Regminton mod. 2312 (575 W) lamp (spectrum shown in Figure 2.12);
- an Ocean Optics ISP-30-6-REFL integrating sphere;
- an Ocean Optics USB4000 XR1-ES spectrometer with a 250-1150 nm wavelength range (sensibility: 3 nm), equipped with a optical fiber with a quartz core.

To obtain the transmittance spectra, the number of photons for each wavelength with (I) and without (I_0) the electrode in the optical path was measured. In the analysis, several contributions have to taken into account: the catalyst, the FTO and the glass substrate transmission, and the reflections due to the refraction indexes of the crossed materials. These contributions are integrated in the Fresnel law, considering the incident rays perpendicular to the interface, so that the reflectance R is:

$$R = \left(\frac{n_1 - n_2}{n_1 + n_2}\right)^2, \tag{2.2}$$

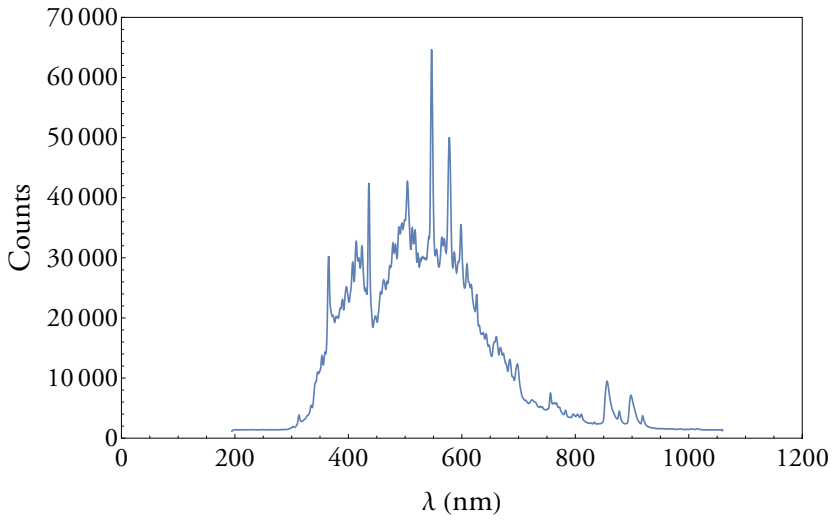

Figure 2.12: Regminton-lamp spectrum.

where n_1 and n_2 are the refraction indexes of the crossed materials. Each refraction index was calculated in function of the λ using the empirical Eq. 2.3 from Bodurov et al. work [70]:

$$n^2 - 1 = \frac{4.6796\lambda^2}{\lambda^2 - 0.2002148^2}. \tag{2.3}$$

These values concern TiO_2 nanoparticles diluted with water to 2 wt%. Following, the reflectance was multiplied by I_0, obtaining the reflectance contribution due to the FTO-TiO_2; subtracting I and normalizing by I_0, the catalyst transmittance was obtained [69]:

$$I^* = RI_0 - I. \tag{2.4}$$

TiO_2 electrodes: results and discussion

In Figure 2.13 the transmission spectrum of the bare TiO_2 is reported. The absorption peak at 340 nm was highlighted, at which corresponds the 40% of the absorption of the incident radiation for that λ. Overall, the analyzed TiO_2 film absorbed the radiation in the range of 310 and 380 nm. The TiO_2 optical characterization result verified the photocatalytic properties reported in literature, for which the TiO_2 photo-activity in the UV range is known.

N-doped TiO_2 electrodes: results and discussion

Similarly, the transmission spectrum shown in Figure 2.14 was obtained for the N-doped TiO_2 by using the same procedure. Also in this case, the absorption peak was

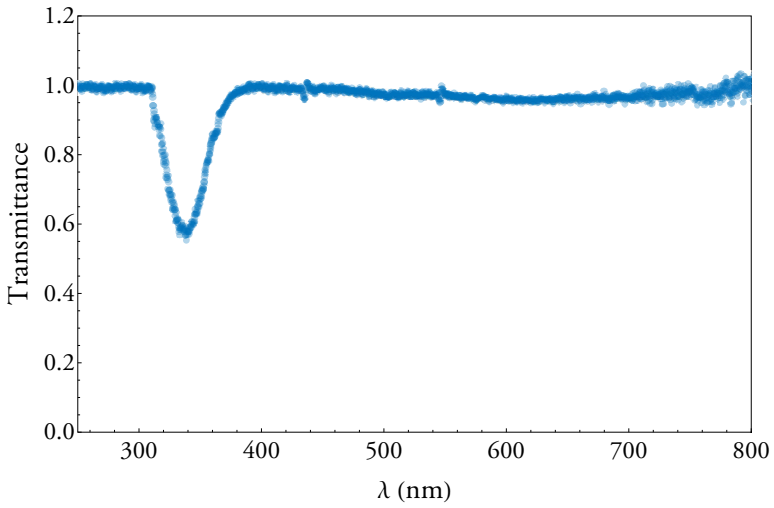

Figure 2.13: TiO_2 transmittance spectrum in function of λ.

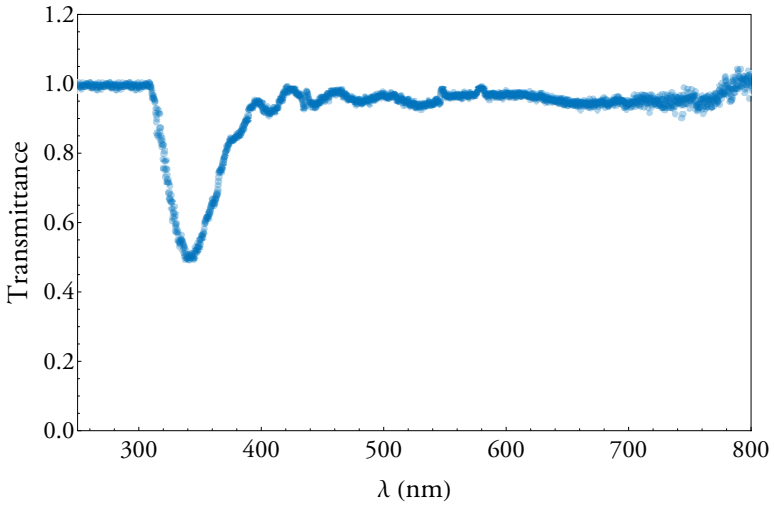

Figure 2.14: N-doped TiO_2 transmittance spectrum in function of λ.

highlighted at 340 nm at which corresponds the 50% of the absorption of the incident radiation for that λ. Overall, the analyzed N-doped TiO_2 deposited layer absorbed the radiation in the range of 310–390 nm. As can be noticed, the desired shift into the visible range due to the nitrogen doping was not obtained. The only difference highlighted between the two spectra is the presence of some minor absorbance peaks beyond the 400 nm in the N-doped TiO_2 spectra, probably due to the presence of N. Nevertheless, these are too small to allow the material to activate using the visible light.

2.3 WO_3 electrodes

A semiconductor material, used as photoanode, is the main component of a PEC cell since it determines the system performances. Indeed, several studies have been carried out to improve the material efficiencies. The mechanical adhesion and chemical film stability are relevant properties that must be considered [71]. In particular, corrosion and dissolution of the photoanode in the electrolyte should be avoided and, in this regards, WO_3 is a promising material due to its photochemical stability in aqueous acidic solution up to pH 5 [72].

In this work, thin films of WO_3 based on nanocrystalline structures were realized in order to minimize the imperfections and the surface contaminations, which may lead to charge trapping and carrier recombination. Moreover, nanostructures combine high electro-active surfaces, good light harvesting abilities and easy-to-fabricate low-cost chemical methods. Indeed, WO_3 can be prepared via several techniques, which are aimed to the production of nanostructured interfaces. These latter optimize the interfacial area as well as the electrical interconnection among the nanoparticles/nanostructures. These methods include, but are not limited to, sol-gel, hydrothermal and electrophoretic processes [73, 61], electrochemical anodization [74], rf sputtering [75], pulsed laser deposition [76], and evaporation [77].

In the following section, three kind of nanocrystalline WO_3 realization processes are presented: sol-gel, electrochemical anodization of metallic tungsten, and solvothermal method. During recent years, the first two implementation methods have been accurately studied by the research group of General and Inorganic Chemistry at the Department of Chemical and Pharmaceutical Sciences, University of Ferrara, main partner of this thesis project [20, 74, 78, 50, 71, 79]. Differently, the solvothermal technique was recently considered as process for the crystalline material synthesis.

2.3.1 Electrodes deposition: materials and methods

The described realization methods were carried out on several materials, which have been used as substrates for the electrode realization. In particular the sol-gel method was used for the realization of a colloidal WO_3 as precursor material, deposited via spin-coating on glass substrate covered by a FTO layer, as in the case of the discussed TiO_2 material. The same precursor was deposited also on glass spheres, unfortunately obtaining a detachment of the material from the substrate, as displayed in the next paragraphs. As alternative, the solvothermal technique has been exploited and tested over glass covered-by-FTO substrates. Finally, the electrochemical anodization

of metallic tungsten has been studied by observing the tungsten trioxide layer growth over the metallic substrate.

Sol-gel route

Since sol-gel routes are based on the sintering of colloidal nanoparticles, they are a simple way to obtain efficient oxide semiconducting films. To date, the most promising results regarding this technique were achieved by Augustynski et al. [61], who developed a sol-gel route using a colloidal solution of tungstic acid to obtain mesoporous semi-conductive films consisting of preferentially oriented monoclinic-phase nanocrystals of WO_3. The synthesis exhibits a series of interesting properties, including high transparency for the wavelengths above 500 nm, good adhesion to the conducting glass support, and large incident-light-to-current conversion efficiencies when acting as photoanodes in a PEC cell. Due to their photoresponse, these electrodes can operate under solar illumination, delivering photocurrents in the range of a few milliamperes per square centimeter.

According to the Santato-Augustynski procedure, the preparation route of the nanocrystalline WO_3 is, thus, presented [80]. Before the treatment, the FTO-glass substrates were cleaned by sonication in isopropyl alcohol (Aldrich) for 10 min. Later, 5 gr of Na_2WO_4 (Carlo Erba) were dissolved in 100 ml of Millipore water; 20 ml of concentrated HCl were added to this solution. The resulting tungstic acid (H_2WO_4) precipitate was collected by centrifugation and washed three times in water to remove HCl and NaCl excesses. The wet precipitate was then dissolved in 5 ml of water at 60 °C in the presence of 2 g of oxalic acid, which acted as dispersing agent thanks to its chelating properties. This led to the formation of a transparent sol of nanoparticles. The resulting colloidal suspension was weighted; a Polyethylen-glycol Bisphenol A Epichlorohydrin Copolymer (PEG-BAE) (Aldrich), in a 1:5 w/w ratio, was added. Finally, ten drops of Triton® X-100 were added, to obtain the nanostructuration of the material during the sintering process. The precursor was deposited via spin-coating on the FTO substrates with a cycle of 600 rmp for 6s and 2000 rpm for 20s. The resulting films were dried in air at approximately 100 °C and then annealed at 550 °C. The described procedure was repeated 6 times, increasing the deposited layer thickness: each spin-coating cycle was followed by an annealing step at 550 °C for 20 min with a final longer annealing for 1h. A picture of the WO_3 layer on glass substrate is shown in Figure 2.15 on the right, a.

The same sol-gel precursor preparation procedure was exploited for the colloidal WO_3 deposition on rough glass spheres of 3 mm in diameter. The spheres were made rough through abrasion cycles for several hours in a Turbo Tumbler 1220 Pro (Lyman

products corporation, Middletown) with the addition of Carborundum (Abrasive G.B. Ltd.). This procedure made more suitable the colloidal WO_3 adhesion with respect to the smooth glass sphere. Firstly, the spheres were cleaned by sonication 3 times in isopropyl alcohol (Aldrich) for 10 min, eliminating the Carborundum and the glass powder. Secondly, they were immersed in the diluted (1:5 V/V ratio) colloidal solution for 5 min, and finally annealed at 550 °C for 1h. In particular, the exploitation of the diluted colloidal solution allowed to obtain spheres with a photocatalytic efficiency similar to that obtained with higher concentrations but, at the same time, avoided the accumulation of large quantities of semiconductor on the substrate. Indeed, the use of too high concentrations led to the easy loss of part of the semiconductor during the photodegradation tests. The attempt to prepare colloids in solvents different from water (such as methanol, ethanol, or isopropanol) led to not reproducible results, thus deciding to continue to work in aqueous environment.

The realized spheres were covered by one or two layer of colloidal WO_3 and tested in case of photodegradation measures, as discussed in the Chapter 3. In static conditions, the photodegradation efficiency showed very good results, but, unfortunately, in flow condition it was obtained a detachment of the WO_3 material from the substrate when immersed into an electrolyte. The solvothermal method was, thus, selected as an alternative technique to obtain better adhesion in case of bare glass substrate.

Solvothermal routes

Generally, the hydrothermal and the solvothermal synthesis terms are used to indicate any chemical reaction in the presence of a solvent in supercritical or near supercritical conditions (high temperature and pressure) [81]. To be more exact, the process is called “hydrothermal” when water is used as solvent, while it is defined as “solvothermal” when organics are used as main solvent. The mechanism of crystalline material synthesis through these methods usually involves a crystal nucleation and a subsequent growth directly in the solution. By controlling the process variables, such as pH, temperature, reaction, time, reactant, and additive concentrations, the final products could be fabricated obtaining the desired particle size and film morphology. According to Grimes et al. procedure [62], the nanocrystalline WO_3 electrodes were realized via solvothermal technique on FTO layers.

Before the treatment, the FTO-covered glass substrates were cleaned by sonication in isopropyl alcohol (Aldrich) for 10 min followed by heating at 450 °C for 15 min. Following, a WO_3 thin seed layer was deposited on FTO. This layer was based on a solution composed by dissolving 0.46 g of metallic tungsten (0.5 M) in 5 ml of 30 wt% H_2O_2 and then adding 2 drops of Triton® X-100. The solution was spin-coated (1000

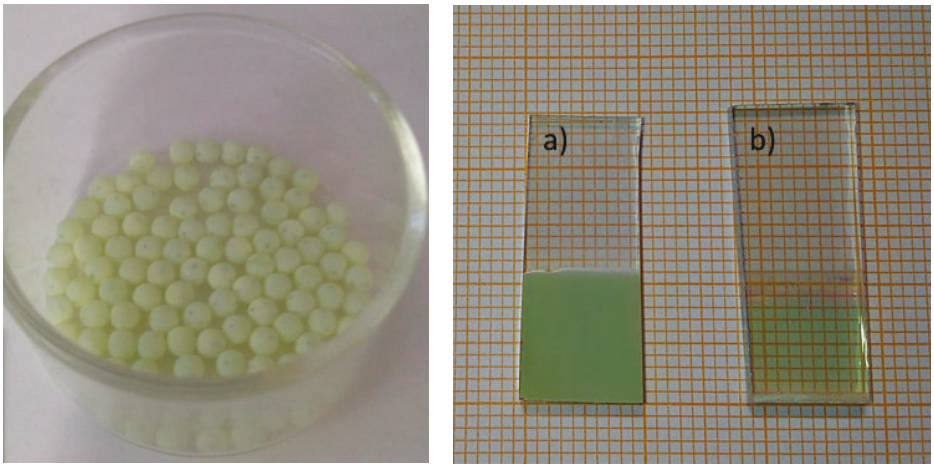

Figure 2.15: On the left: solvothermal WO_3 deposited on rough glass spheres. On the right: solvothermal (a) and colloidal via sol-gel (b) WO_3 electrodes deposited over FTO-glass substrates.

rpm for 9 s and 2000 rpm for 20 s) on the FTO and, finally, annealed at 500 °C for 1 h in air, obtaining a very thin dense layer.

The solvothermal precursor composition played a dominant role in controlling growth of the tungsten trioxide nanostructures. Nanowire and nanoflake arrays can be selectively deposited by adjusting the amount of water added to the precursor [62]. Moreover, acidic conditions were necessary to grow the nanostructured WO_3 film. In particular, the solution for the solvothermal synthesis was prepared by dissolving 1.25 g of H_2WO_4 in 10 ml of Millipore water (mQ) and 10 ml of 30 wt% H_2O_2 while heating and stirring bain-marie at 95 °C. 18 ml of this H_2WO_4 solution (0.25 M), with 1.2 g of oxalic acid and 3 ml of HCl (6M), were added to 60 ml of acetonitrile and 15 ml of mQ water. The obtained reaction mixture was kept in a container at 180 °C for 2 h within an autoclave with inside the FTO-coated substrates oriented at 30 degrees with respect to the vertical and the FTO side facing the bottom of the container. Finally, the resulting electrodes were annealed in air at 500 °C for 1 h, obtaining the WO_3 layer (Fig. 2.15 on the right, b).

Unfortunately, the electrodes realized using the described procedure showed a poor adhesion of the WO_3 layer. As a consequence, a very thin TiO_2 blocking layer was deposited on the FTO glass substrate to improve the adhesion. The layer was deposited via soaking in a 0.4 M $TiCl_4$ solution at room temperature for 6 h, with the conductive side facing upward. Thus, the film was annealed at 450 °C for 45 min. The same procedure was exploited in case of the rough glass spheres, obtaining a yellow coating film of WO_3 as shown in Figure 2.15, on the left.

Electrochemical oxidation of metallic tungsten

Tungsten (W) belongs to the group of the so-called valve metals, which show a very high corrosion resistance in most common aqueous media, and does not react to the alteration of the surface layer. According to electrochemical and XPS evidences [82], it has been proposed that anodic oxidation of W may result in the initial formation of a mixture of oxides, namely WO_2, W_2O_5 and WO_3 according to the following equations [74]:

$$W + 2H_2O \rightarrow WO_2 + 4H^+ + 4e^-; \tag{2.5}$$

$$WO_2 + H_2O \rightarrow W_2O_5 + 2H^+ + 2e^-; \tag{2.6}$$

$$W_2O_5 + H_2O \rightarrow 2WO_3 + 2H^+ + 2e^-. \tag{2.7}$$

Impedance analysis performed by Metikos-Hukovic et al. [83] during the potentiostatic anodization, also suggests that the migration of oxygen vacancies is the main charge transport mechanism across the growing oxide film, and hence it is enhanced by the accumulation of negative charges at the film-solution interface. Therefore, the electrochemical anodization of metallic tungsten can be a convenient method for the realization of porous photoactive substrates in which the oxide structures are tightly interconnected and strongly tied to the metal collector. Both factors contribute to the increase of the photogenerated charge collection efficiency.

Besides detailed oxide formation studies, the most common route for the anodic preparation of porous WO_3 films involves the application of a constant potential to metallic tungsten laminae in the presence of aqueous electrolyte containing fluoride anions that establish mild oxide dissolution conditions. Indeed, in the electrolytic composition water is required to act as an oxygen donor allowing for oxide formation, while fluorides act as a chemical etchant, promoting localized oxide dissolution and the formation of corrosion pits from which the field assisted dissolution is stronger. The competition between the oxide layer formation and the dissolution bring to the nanoporous structure. In order to reach these conditions, a harsh treatment consisting in the application of a sudden potential step of several tens of volts, between the anode and the cathode, has to be adopted. In addition, electrolyte temperature and composition are important for reaching reproducible results and a reasonable surface coverage [20] and have, hence, to be controlled. Following, the realization method based on a patented route [84] is presented.

Prior to anodization, metallic tungsten foils (99.95%, 0.1 mm thick, Alfa Aesar) ca.

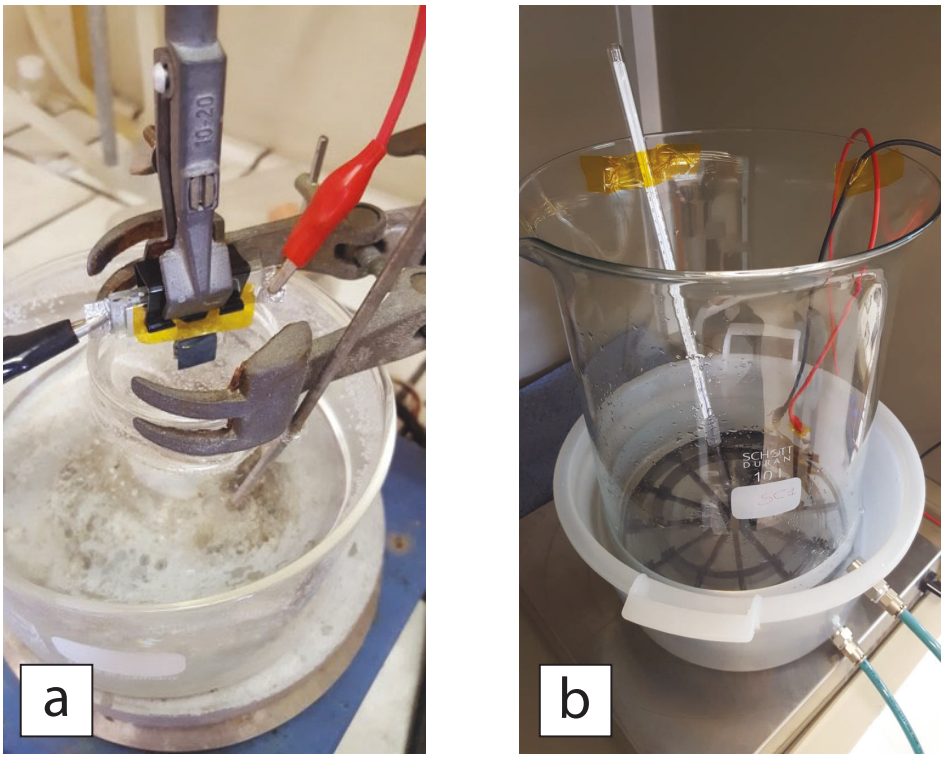

Figure 2.16: Picture of the apparatus for the electrochemical anodization process: a) on a W surface of 2×1 cm^2; b) on a W lamina of 1.5×100 cm^2.

2×1 cm^2 were sonicated in alconox solution (Aldrich) for 10 min, rinsed in water and washed with ethanol and acetone. The potentiostatic anodization was carried out in a two-electrode configuration in which the tungsten anode and cathode were assembled facing each other at an average distance of 3 mm (Fig. 2.16 a). By using a DC power supply (KERT Cosmo 1500/1), the voltage was quickly manually increased to a final value of 40 V at a rate of approximately 0.5 V/s. The electrolyte was composed by N-methyl-formamide (Aldrich) NMF/H_2O 8:2 and 0.05% w/w NH_4F. The solution was not stirred, and the anodization was carried out for 72 h at room temperature (20 ± 3 °C). The typical average current density during the anodization in NMF was 8–10 mA and the total charge exchanged—obtained by integration of the i-t curve—was 150 ± 18 C. After the anodization process, the resulting electrodes were rinsed with water, ethanol, and acetone, and then sonicated in water for 10 min in order to remove the weakly tied surface material. The electrodes were then dried under a stem of air, and finally annealed in air at 550 °C for 1 h to promote sintering and crystallization.

In order to obtain an electrochemical oxidation of a large surface area, considering a future solar device realization as application, the same recipe was adapted—as

electrolyte quantity—for the anodization of a metallic tungsten strip of ca. 1.5×100 cm^2. The apparatus was assembled adapting the anode and cathode foils in a spiral configuration in order to maintain a constant average distance between the anode and cathode, thanks to a circular ray system, especially designed. As it can be observed in Figure 2.16 b, the foils were immersed into the electrolytic solution, giving the power supply with a Kepco bipolar operational power supply/amplifier (0 to ± 50 V, 0 to ± 4 A).

In this case, the solution was stirred with a magnetic stirrer and its container was immersed in water at room temperature in order to cool the solution. Indeed, due to the reached high currents (∼4 A), the solution tended to increase its temperature. The water was maintained ca. at room temperature by circulating within the system thanks to a pump.

The obtained foil was accurately anodized following the described procedure, but unfortunately it showed an insufficient photocatalytic efficiency, probably due to the temperature surges reached. From the industrial point of view, is thus necessary to create an apparatus for a better control of the electrochemical anodization parameters.

2.3.2 Morphological characterization

Sol-gel routes

A superficial tomography of the WO_3 layer was evaluated by Atomic Force Microscope (AFM) (Digital Instruments VEECO, Nanoscope III Scanning Probe Microscope). As can be observed in Figure 2.17, the nanoparticles range between 50-70 nm in diameter, thus a mesoporous structure of the oxide semiconductor that uniformly covers the substrate was obtained. According to the Santato-Augustynski procedure, the high-temperature range of 500–550 °C influenced the nanoparticles size and, hence, the surface morphology. Indeed, it has been observed (Fig. 2.18) that a further increase of the temperature turned into larger-sized nanoparticles, with clearly observable pores [20]. Moreover, prolonging the heating, an higher degree of crystallinity of the thin film was observed. Indeed, the formation of the WO_3 monoclinic band structure was evaluated by Raman spectroscopy (Fig. 2.19), confirming the more intense formation of the bands, which are originated by the bending and the stretching of the W-O-W bonds. The average thickness is an important parameter to be controlled as it influences the produced photocurrent [71]. The evaluation of the WO_3 layer thickness was observed via Scanning Electron Microscope imaging with a Zeiss Evo 40 SEM with an electron beam of 18 keV (Fig. 2.20). As discussed in the next paragraph, the photoelectrochemical tests confirmed that the best results can be obtained with porous

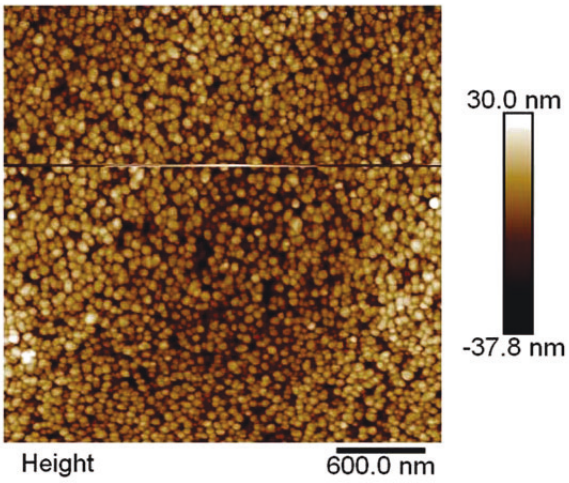

Figure 2.17: AFM image of colloidal WO_3.

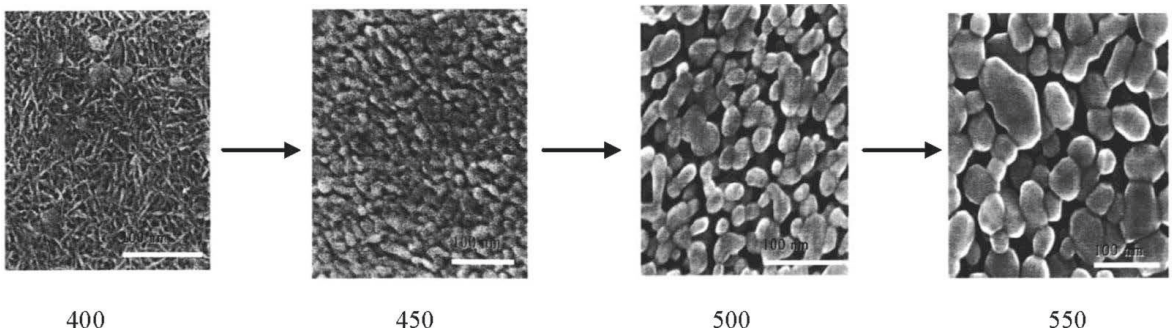

Figure 2.18: SEM micrographs of WO_3 films obtained by deposition of the tungstic acid/PEG precursor annealed in the 400–550 °C temperature range. Adapted from [20].

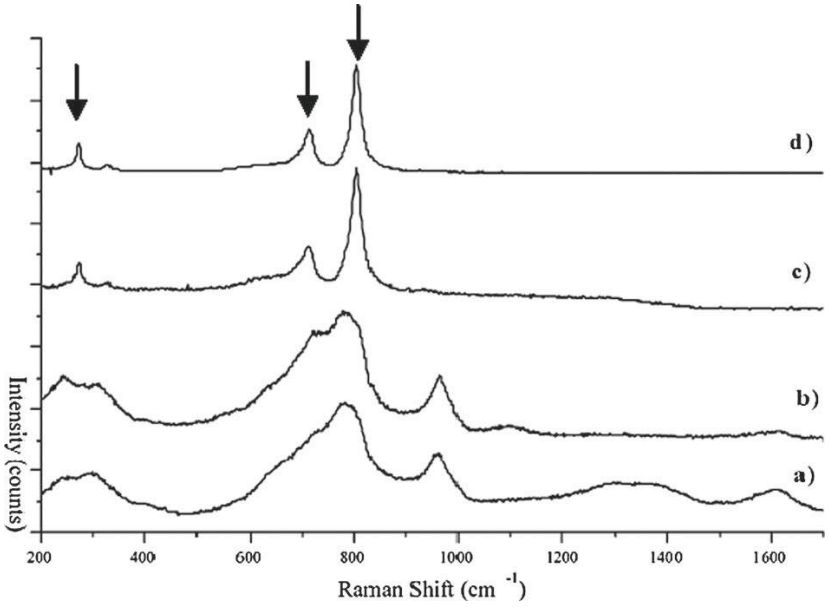

Figure 2.19: Raman spectra of WO_3 thin films deposited from tungstic acid/PEG precursor at 350°C (a), 450°C (b), 500°C (c), 550°C (d). The arrows indicate the main monoclinic WO_3 bands. Adapted from [20].

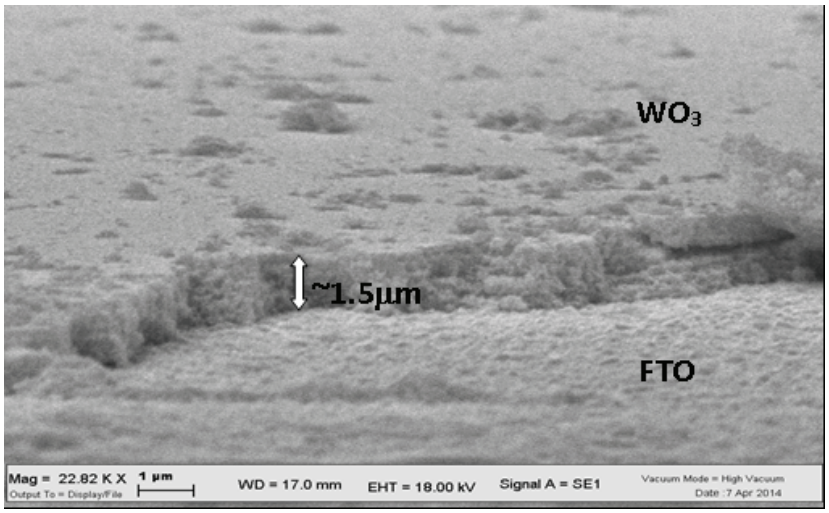

Figure 2.20: Cross section SEM image of the WO_3 colloidal layer. Adapted from [85].

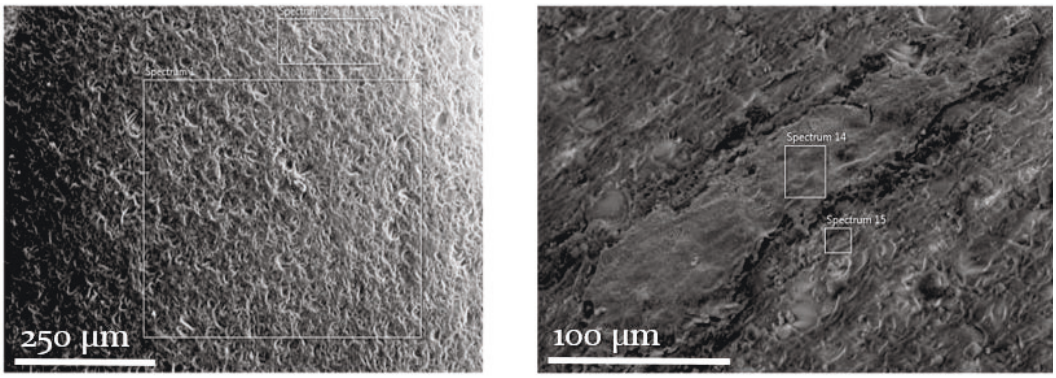

Figure 2.21: Top view SEM image of the bare glass surface of the rough sphere (on the left) and of the WO_3 colloidal layer over the glass sphere (on the right).

electrodes 1.5–2.5 μm thick. Indeed, they show a good crystallinity, a significant improvement in film photoactivity with increasing annealing temperature, and saturation photocurrents of 2–2.5 mA/cm^2 under AM 1.5 illumination.

The superficial morphology of the colloidal WO_3 deposited on glass spheres was also observed. In Figure 2.21 the surface of the rough glass sphere (on the left) is displayed, in comparison with the top view of the WO_3 colloidal coating (on the right). In this case, EDS spectroscopy was carried out (Fig. 2.22); it highlighted the presence on the spheres of several elements in addition to W, O, S, including Na, Ca, Mg, Al. The presence of some of these elements is due to glass composition. In particular, the presence of impurities may be a possible answer to the colloidal detachment from the substrate.

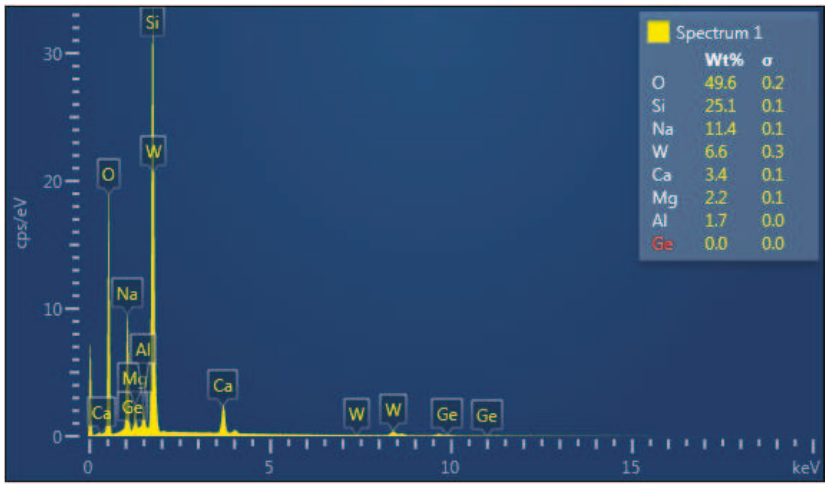

Figure 2.22: EDS analysis on spheres covered by one coat of colloidal WO_3.

Solvothermal routes

Referring to Grimes's work, WO_3 morphologies of hexagonal and monoclinic structure have been obtained, ranging from nanowire to nanoflakes arrays [62].

The morphology of the electrodes realized via solvothermal technique and the WO_3 seed layer deposited on TiO_2 thin film were characterized by using a Jeol JSM 70001F FEG-SEM apparatus. No SEM images of the thin TiO_2 layer are here presented because its thickness was below the instrumental detection limit (5 nm in cross section mode), thus suggesting a TiO_2 layer thickness of few nm. Differently, the WO_3 seed layer could be observed (Fig. 2.23) as a compact film.

The thickness of the seed layer varied from 25 to 75 nm probably due to the inhomogeneous nature of the pyrolytic FTO (thickness 500–600 nm). Instead, the solvothermal WO_3 layer showed two different structures, as displayed in Figure 2.24. Above the compact seed layer, the WO_3 structure featured nanoparticles of 50–100 nm in diameter. Starting from this region, the solvothermal film grew with a $\sim$8 μm thick layer of thin and wide lamellar structures, also visible in Figure 2.25, where a top-view of the electrode surface is presented. The nanoflakes film grow perpendicular to the substrate.

In addition, X-ray diffraction (XRD) data analysis (Bruker D8 Avdance XRD Instrument) was conducted (Fig. 2.26) to have a comparison between the colloidal and solvothermal WO_3 structures, investigating their lattice properties, which may affect the electrode photoactivity. The peaks of both materials are sharp and clear, and they could be attributed to high-quality monoclinic WO_3. The diffraction peaks at 2θ of 23.2°, 23.6°, and 24.4° correspond to the (002), (020), and (200) facets. As well known,

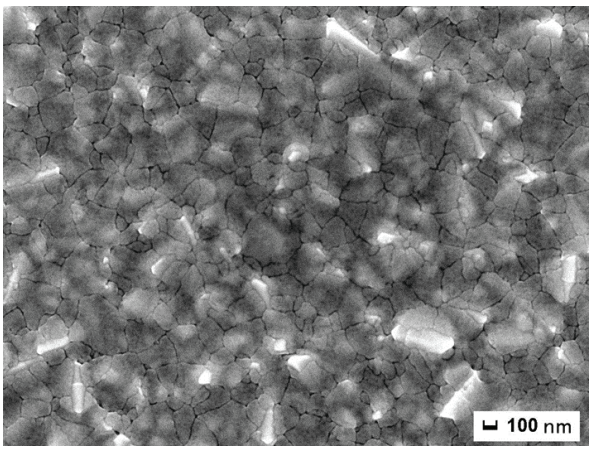

Figure 2.23: SEM top view of the WO_3 seed layer. Adapted from [16].

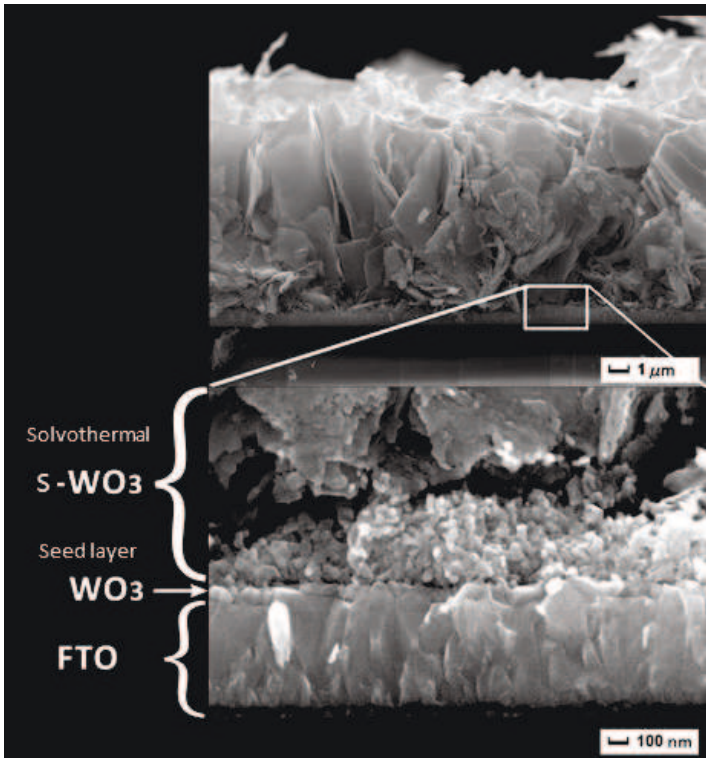

Figure 2.24: SEM cross section of the WO_3 electrode solvothermally grown. Adapted from [16].

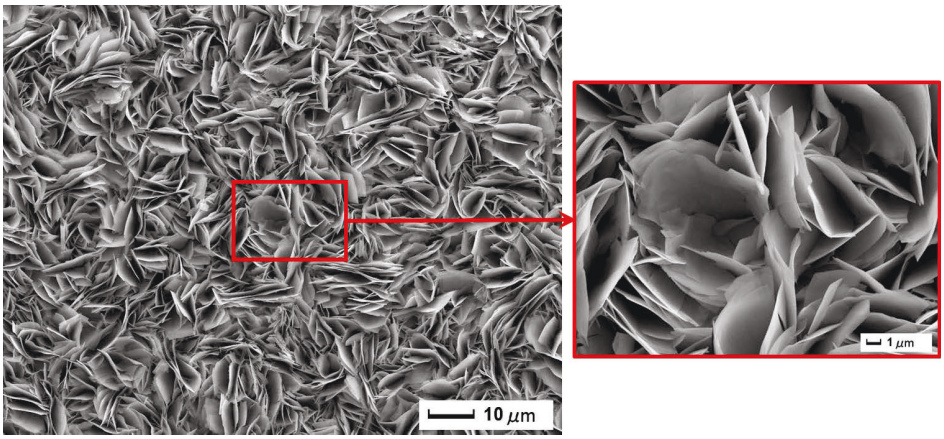

Figure 2.25: SEM top-view of the WO_3 electrode solvothermally grown. Adapted from [16].

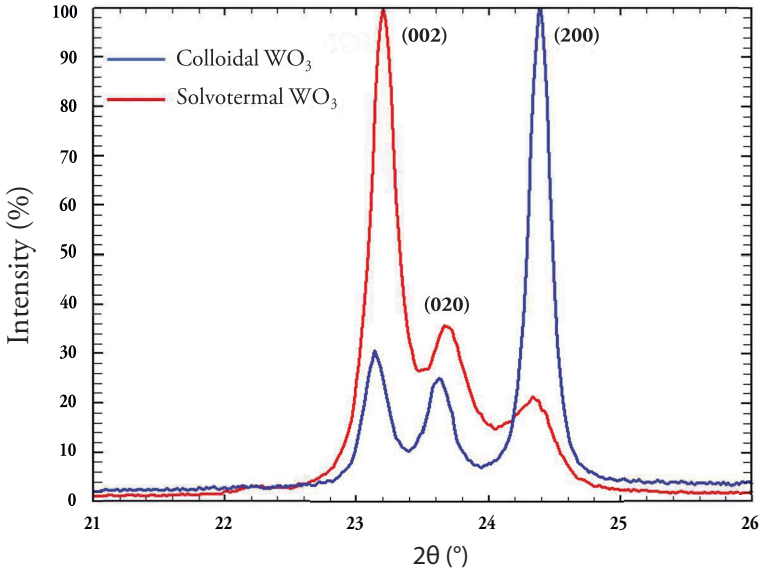

Figure 2.26: XRD spectrum of solvothermal (red) and colloidal (blue) WO_3 structures. Adapted from [16].

the reactivity of the photoelectrode is influenced by its atomic surface and its linked electronic structure [86], thus the preferential exposition of (200) or (002) facet strongly influence electrode performances. According to Lu et al. [87], the preferential exposure of the highly active (001) facets, which belong to the same 001 family of planes as (002) facets, endowed the WO_3 nanocrystals with significantly enhanced photocatalytic activity. This can be attributed to the effective production of active oxygen species and reduced recombination of photogenerated electrons and holes.

Electrochemical oxidation of metallic tungsten

After 72 hours at room temperature and the subsequent annealing, the electrochemical anodization in NMF resulted in the formation of an irregular porous nanocrystalline (monoclinic) oxide layer 3–5 micron thick. The layer was covered by bundled-up structures, ∼300 nm wide, longitudinally crossed by cracks that gave to the surface an overall worm-like appearance. The AFM image (Fig. 2.27), gave the topographic picture of the surface, confirming the existence of such morphology and revealing a maximum height difference between structure crests and valleys or pores of approximately 600 nm. Considering several measures, it was demonstrated [74, 88] that the same surface morphology was observed in case of an accelerated anodization route at 40 °C, in which nano-tubular domains can also be noted (Fig. 2.28). This analogy suggested that, also under these conditions, the formation of the oxide followed the same stages that were

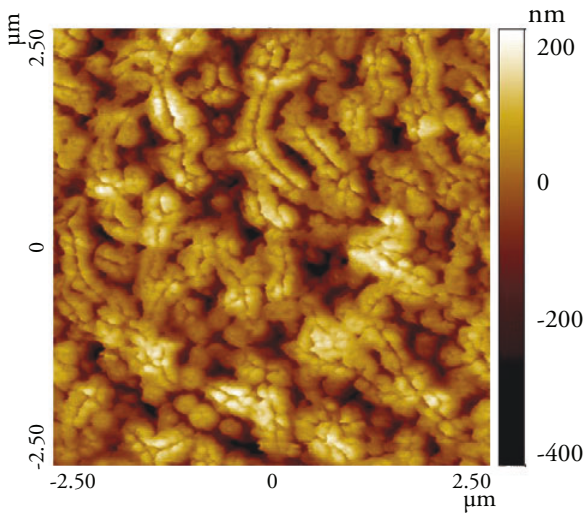

Figure 2.27: AFM micrograph of anodically formed WO_3 after annealing process at 550°C for 1h in air. Adapted from [88].

observed at room temperature. The kinetics of both the competing processes, i.e. the oxide formation and the dissolution, have been improved, as demonstrated by the significantly higher currents (40–50 mA/cm^2 at 40 °C compared to 4-6 mA/cm^2 at room temperature), which were observed during the accelerated anodization process (Fig. 2.29). After an initial time interval, during which the current is very low due to the presence of the compact oxide layer, a steep rise of the anodic current can be observed. This indicates that both the chemical etching by F^- ions and the oxide dissolution, which is coupled with the formation of WO_3 from the underlying metal, were taking place [88]. The competition between the two processes determineed the inward movement of the W/WO_3 interface and the formation of an outer porous oxide film, which can reach a thickness of few microns.

2.3.3 Electrochemical characterization

The photoanodes were tested in both two and three electrodes photo-electrochemical configurations. They had a Pt-foil as a counter electrode, and a Saturated Calomel (SCE) as a reference electrode, respectively, as in case of the TiO_2 electrochemical characterization. Indeed, the electrochemical measurements were carried out by using the same experimental setup exploited for the TiO_2 measurements (Section 2.2.2). Also in this case, the photocurrents (via JV curves) and the photoconversion (IPCE) produced by the WO_3 electrodes were obtained. The electrodes were tested in Na_2SO_4 and H_2SO_4 electrolytes, which are commonly used for WO_3-based PEC-cell characteriza-

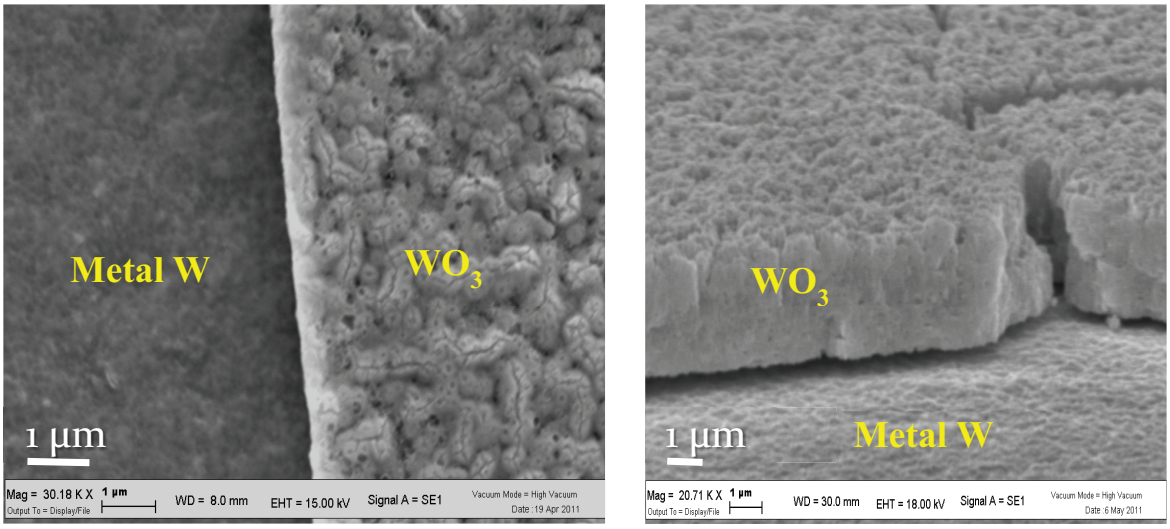

Figure 2.28: SEM micrograph of anodically formed WO_3 after 7 h at 40°C after annealing process at 550°C for 1h in air. On the left, the to view of the oxide layer surface is shown with respect to the metallic substrate; on the right the cross section shows the thickness of the WO_3 layer. Adapted from [88].

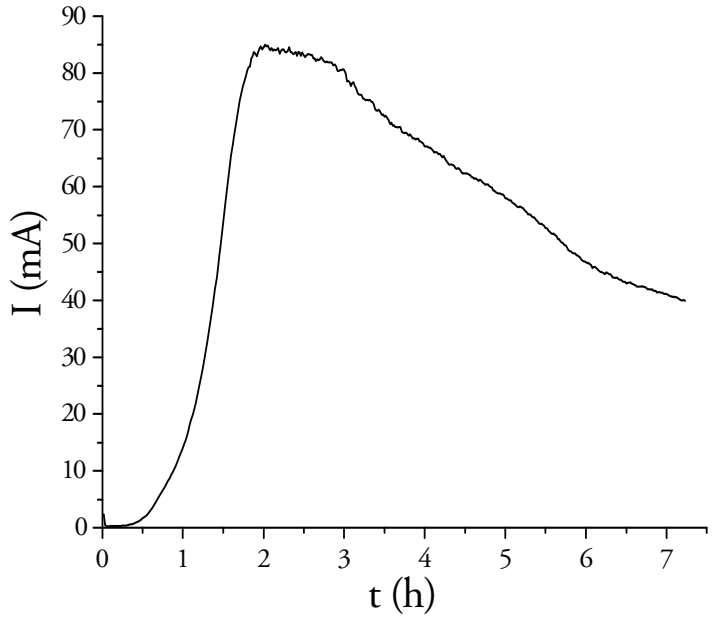

Figure 2.29: Typical current-time behaviour recorded during the anodization process. Adapted from [88].

tion. In this way, the oxide semiconductor behaviour in neutral and acidic environment can be studied.

Sol-gel routes: colloidal WO_3

Concerning the electrochemical tests on colloidal WO_3, JV curves were carried out under modulated illumination in H_2SO_4 and Na_2SO_4 solution to investigate the different behaviour due to the diverse counter-ions. As it can be observed in Figure 2.30, the maximum photocurrent remained the same, indicating that, probably, the ion mobility through the photoactive film is not a limiting factor, with a subsequent minimal recombination via surface states.

During the electrochemical tests, attention was paid concerning the neutral environment, considering the pH real conditions at the end of the water line—in Ferrara the pH value is ∼7.6—in a wastewater plant. Indeed, as reported in literature, WO_3 is a promising material due to its photochemical stability in aqueous acidic solution up to pH 5 [71]. The problem is, thus, represented by the tungsten trioxide stability in neutral environment, which has to be studied. For what concerns the JV curves, the measurements were carried out also in different concentration solution of Na_2SO_4, 0.5 M, 5 mM, and 0.7 mM.

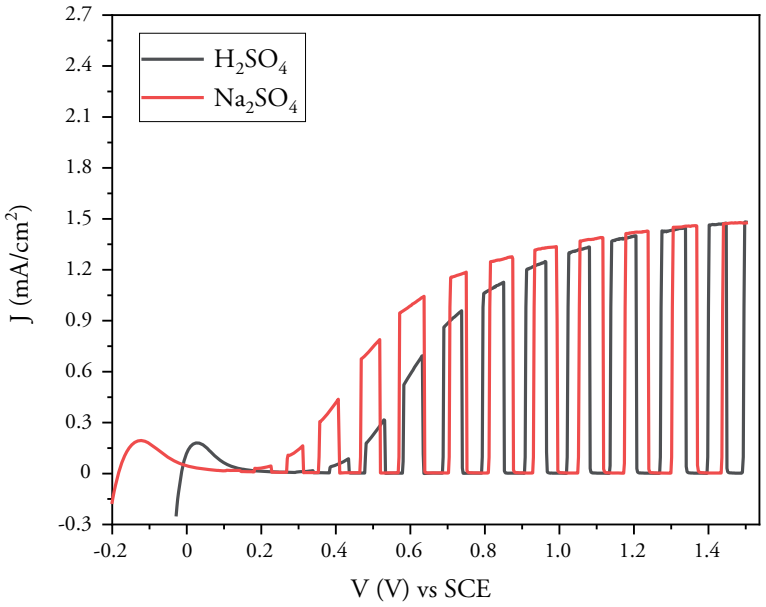

Figure 2.30: J-V curves of colloidal WO_3 in neutral (pH 7) Na_2SO_4 electrolyte 0.5 M (red) and in acidic (pH 0) H_2SO_4 electrolyte 1 M, three electrodes conditions Pt vs SCE, under modulated illumination with intensity of 100 mW/cm^2.

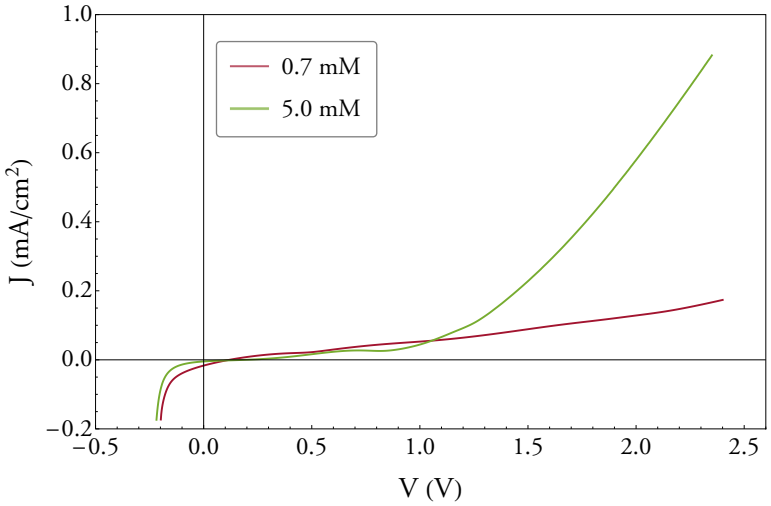

Figure 2.31: JV curves of colloidal WO_3 in two electrodes conditions vs Pt, under light intensity of 100 mW/cm^2, within neutral (pH 7) Na_2SO_4 electrolyte at two different concentration: 0.7 mM (red line) and 5 mM (green line).

Figure 2.31 displays the photocurrent density vs Pt for two diluted solution: 0.7 mM (red line) and 5 mM (green line) of Na_2SO_4 at pH 7, under 100 mW/cm^2. The more the solution is diluted, the more the corresponding photocurrent is inferior due to the lower conductivity of the solution. The electrode was negatively biased down to -0.2 V, since the transition from -0.2 to 0 V clean the surface from oxidation intermediates

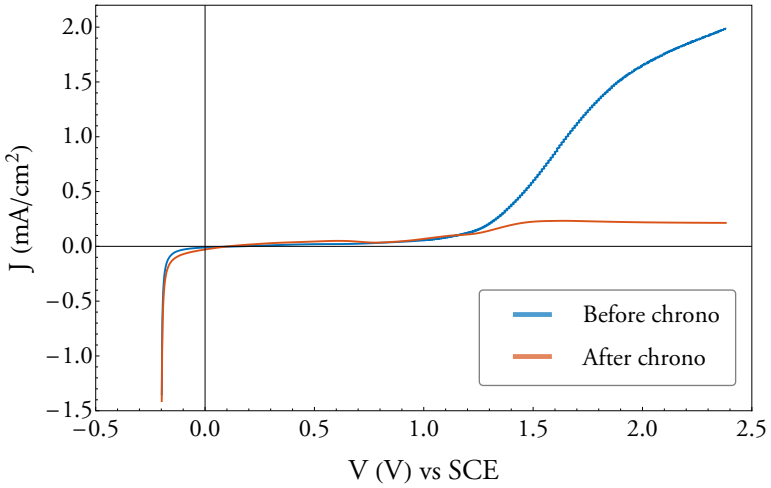

Figure 2.32: J-V curves of colloidal WO_3 in neutral (pH 7) Na_2SO_4 electrolyte 0.5 M, three electrodes conditions Pt vs SCE, with light intensity of 100 mW/cm^2: before chronoamperometies (blue line) and after (orange line).

that may be blocking the active surface. Second, the electrochemical doping occurring upon W^{5+} formation helps to maintain WO_3 conductivity.

In Figure 2.32, JV measurements were, instead, performed under the same conditions, but in this case a concentrated (0.5 M) solution of Na_2SO_4 was exploited. Since the solution was more conductive with respect to the diluted one, the photoanode reacted showing an increase of the produced photocurrent, ca. 2 mA/cm^2 at 2.4 V (blue curve). This values are comparable to the observed water oxidation photocurrents for colloidal WO_3 films reported in the literature [60, 63, 89, 90].

After the JV measurements, chronoamperometry tests were carried out on the same electrodes, by observing the photocurrent trends in time. Here, a drop of the efficiency over time was observed: this led to a considerable decay of the photocurrent value (orange line in Fig. 2.32). The photocurrent decay was probably due to the accumulation of peroxide intermediates on WO_3 surface during water oxidation. Indeed, although water oxidation to oxygen is energetically favorable, it is kinetically slow and subject to other competing redox reaction, including the formation of peroxide intermediates [91]. Several solutions have been tested, among treatment in sulfuric acid, annealing, and polarization cycles, finding the latter as the best solution to be adopted in our solar systems. As it can be observed in Figure 2.33, the attempt of reactivating the electrode by applying a negative potential close to the V_{oc} value caused a temporary return of the photocurrent to the initial values.

In a potentiostatic arrangement, the applied voltage was switched between negative

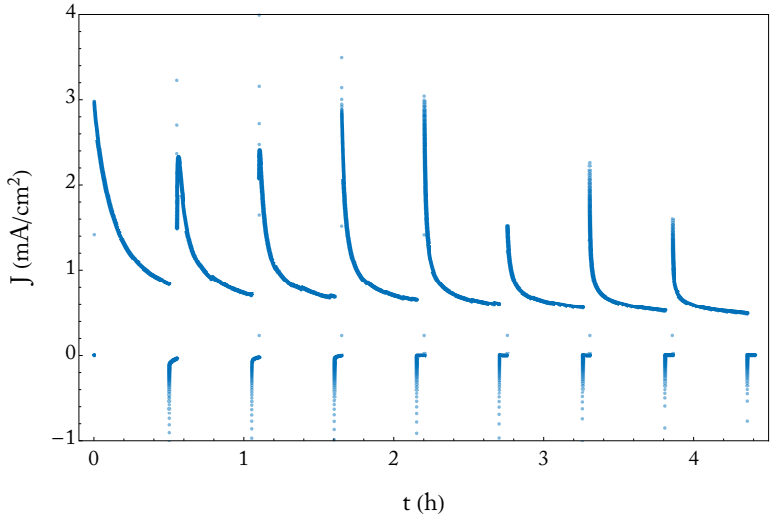

Figure 2.33: Chronoamperometry of colloidal WO_3 in neutral (pH 7) environment, two electrodes conditions, with light intensity of 500 mW/cm^2, with polarization cycles of 1800 s at 2 V and 180 s at 0 V

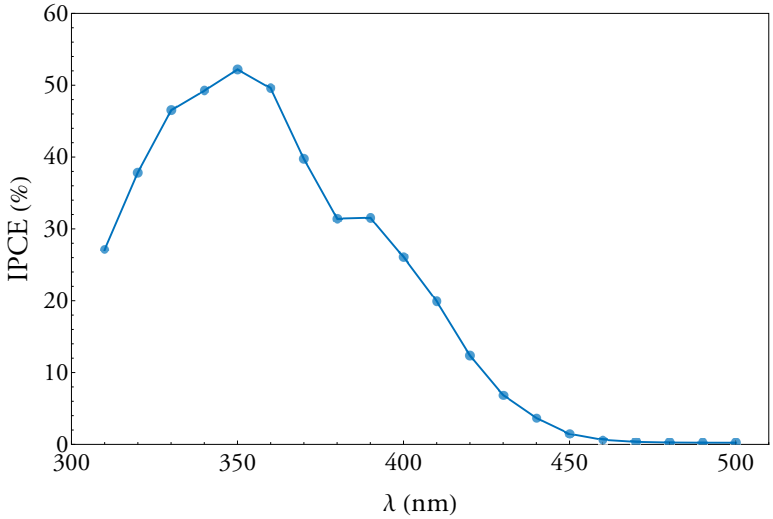

Figure 2.34: IPCE spectrum under 1.5 V vs Pt in neutral (pH 7) Na_2SO_4 electrolyte 0.5 M of colloidal WO_3.

(from 0 from -0.3 V) and positive (from 2.0 to 2.5 V) values, and the resulting current was integrated as a function of time. Upon negative polarization, electrons are injected into the conduction band of the semiconductor, and the negative charge is compensated by migration/intercalation of H^+ into the nanocrystals; with positive polarization, discharging of the film is produced. Charge compensation occurs only for sites that can be effectively permeated by the solvent, therefore this method can provide a means to probe that the electro-active surface is able to exchange charges with the electrolyte [71].

This polarization inversion method is at the base of the photoanode efficiency reactivation within the solar devices that were realized in this thesis work. In the following Chapter, the system exploited to make autonomous the polarization cycles are displayed.

To conclude the discussion on the electrochemical tests performed on colloidal WO_3, photo-conversion measurements are here reported. A wide spectral sensitivity was measured, showing a maximum of the IPCE of the order of more than 50% and a photoaction onset at 460 nm (Fig. 2.34).

Solvothermal routes

The solvothermal film growth technique introduced by Grimes shows good photoelectrochemical results, among which an incident photon-to-current conversion efficiency higher than 60% at 400 nm, with a photocurrent of 1.43 mA/cm^2 under AM 1.5 illu-

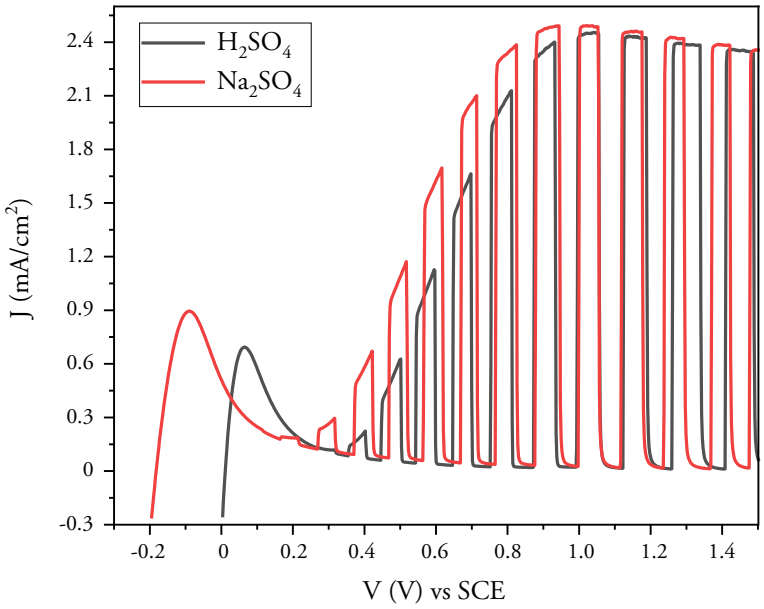

Figure 2.35: J-V curves of solvothermal WO_3 in neutral (pH 7) Na_2SO_4 electrolyte 0.5 M (red) and in acidic (pH 0) H_2SO_4 electrolyte 1 M, three electrodes conditions Pt vs SCE, under modulated illumination with intensity of 100 mW/cm^2.

mination [62]. In this thesis work, the J-V curves were carried out under modulated illumination in H_2SO_4 and Na_2SO_4 solution, as in case of the sol-gel colloidal WO_3. Also in this case, as can be observed in Figure 2.35, the maximum photocurrent remained the same in both environments. The photocurrent onset, instead, changed because of the different pH values. Indeed, the onset potential at higher pH values theoretically shifts in the cathodic direction of 400 mV [16].

Figure 2.36 displays J-V curve obtained under 100 mW/cm^2 illumination condition in a 0.5 M solution of Na_2SO_4 in a neutral environment. In this case, the graph shows the values of the photocurrent reached in case of the solvothermal growth with (blue line) and without (orange line) the addition of the adhesion TiO_2 layer. The best performances showed a maximum photocurrent value of 2.1 mA/cm^2, reached at a V_{oc} of 1 V in presence of the TiO_2 layer. Therefore, the presence of the adhesion layer improved both the WO_3 film adhesion, and the performances of the entire electrode. This happened because, the electrode could still collect electrons despite the presence of TiO_2, which probably is defective enough to allow for charge collection channels. Indeed, the thin layer (< 5 nm) does not allow for the full development of its band structure. Finally, the IPCE% measurements are reported. As shown in Figure 2.37, a wide spectral sensitivity was measured, with a maximum of IPCE of the order of more than 60% in the UV part of the spectrum. In addition, it can be observed the

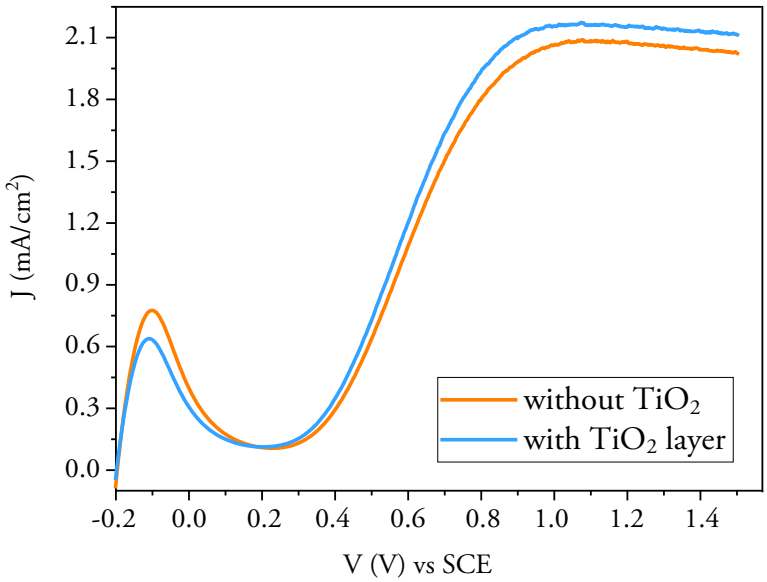

Figure 2.36: J-V curves of solvothermal WO_3 in neutral (pH 7) Na_2SO_4 electrolyte 0.5 M, three electrodes conditions Pt vs SCE, under illumination with intensity of 100 mW/cm^2: in case of TiO_2 blocking layer (blue line) and without the TiO_2 (orange line).

activation of the electrode in the visible range of the solar spectrum, from 400 to 460 nm.

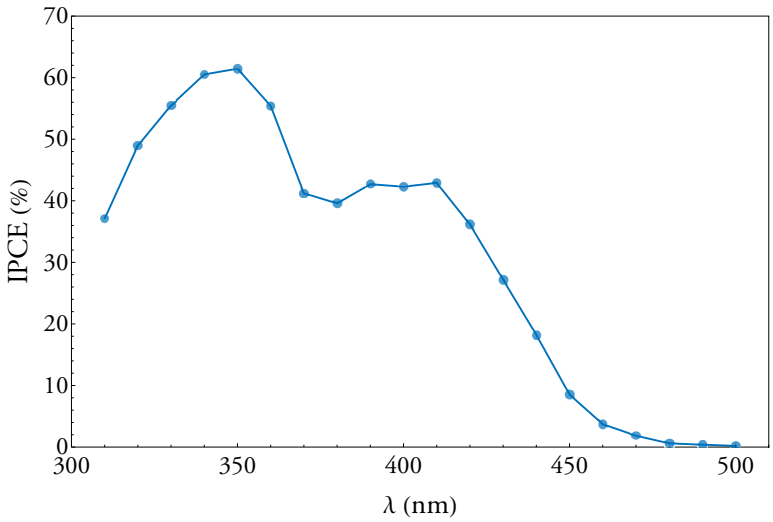

Figure 2.37: IPCE spectrum under 1 V vs Pt in acidic (pH 0) H_2SO_4 electrolyte 1 M of solvothermal WO_3.

Electrochemical oxidation of metallic tungsten

As displayed in Figure 2.38, when compared to the colloidal WO_3, the photoelectrochemical performances of the anodized WO_3 were relevant in particular under high power intensities. Indeed, while the efficiencies of the two electrodes were quite similar at low power intensities, under strong illumination condition the anodically grown electrode did not show saturation, and outperformed the colloidal film by almost a factor of four. The results indicated a more effective hole transfer to the electrolyte under high power intensities. This suggested that it is convenient to exploit the anodized WO_3 in devices that use solar concentration. As consequence of the described results, the current-voltage measurements were carried out considering different light intensities—from 100 to 500 mW/cm^2—to evaluate the electrode response under solar concentration conditions of the anodized WO_3. The tests were accomplished on wastewater samples that were used as electrolytes in a configuration of both two (Fig. 2.40) and three (Fig. 2.39) electrodes. In the first configuration, the applied potential difference is divided between the working electrode (WO_3) and the counter-electrode (Pt). As already introduced, under these conditions the counter electrode type, the active surface area, and the hydrogen presence on the counter electrode during the measurements can influence the threshold potential of the photocurrents. Differently, in three-electrode measurements, an unpolarizable reference (SCE) is used, thus reducing the photocurrent shift due to the over-potential. For what concerns these tests, the addition to

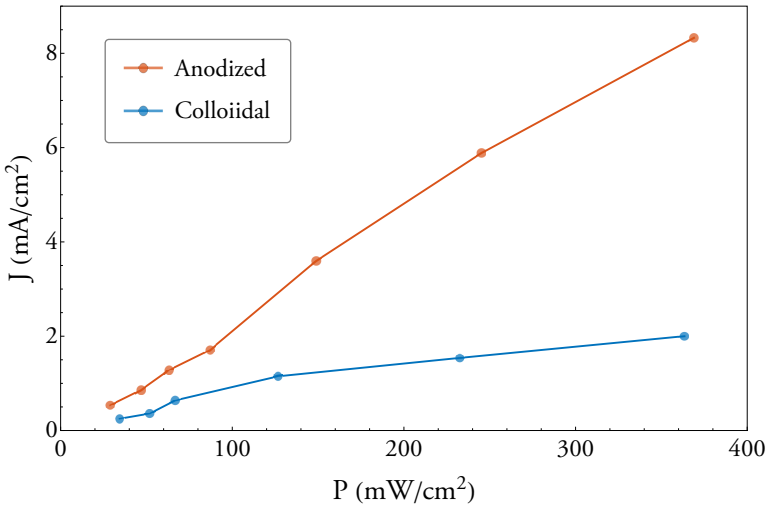

Figure 2.38: Photocurrent density taken at 1 V vs SCE as a function of the incident irradiance (AM 1.5) of the anodically grown (orange) and sol-gel (blue) WO_3. Adapted from [88].

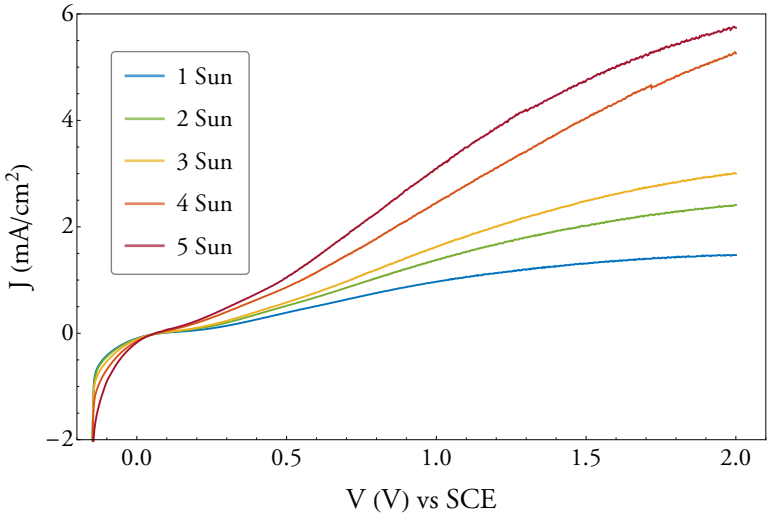

Figure 2.39: J-V curves in real wastewater at pH 7.5, three electrodes conditions with Pt vs SCE, with light intensities from 100 to 500 mW/cm^2.

the wastewater of aluminum sulfate ($Al_2(SO_4)_3$) was considered, in order to observe the possible change in the electrode efficiency. Since its high efficiency, effectiveness in clarification, and utility as a sludge de-watering agent, aluminum sulfate is a chemical compound that is commonly used as coagulant within the processes of coagulation and flocculation in the current waste-water treatment plants. Comparing the graphs 2.40 and 2.41, it is possible to notice that the threshold potentials did not change signifi-

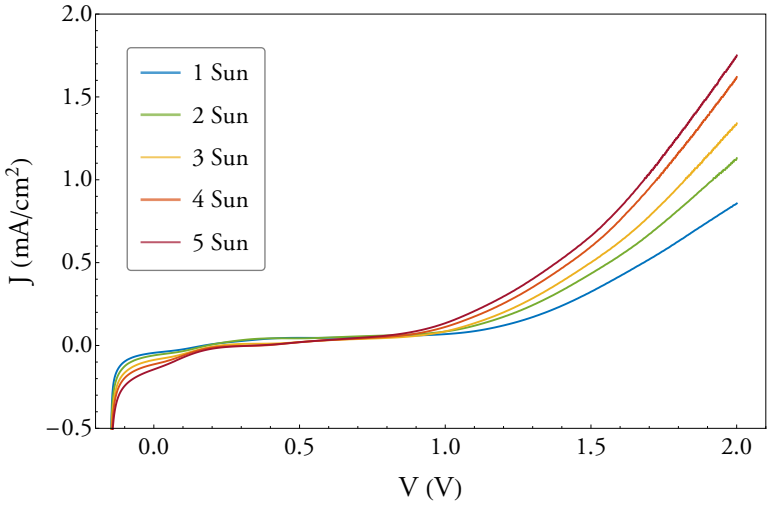

Figure 2.40: J-V curves in real wastewater at pH 7.5, two electrodes (Pt) conditions with light intensities from 100 to 500 mW/cm^2.

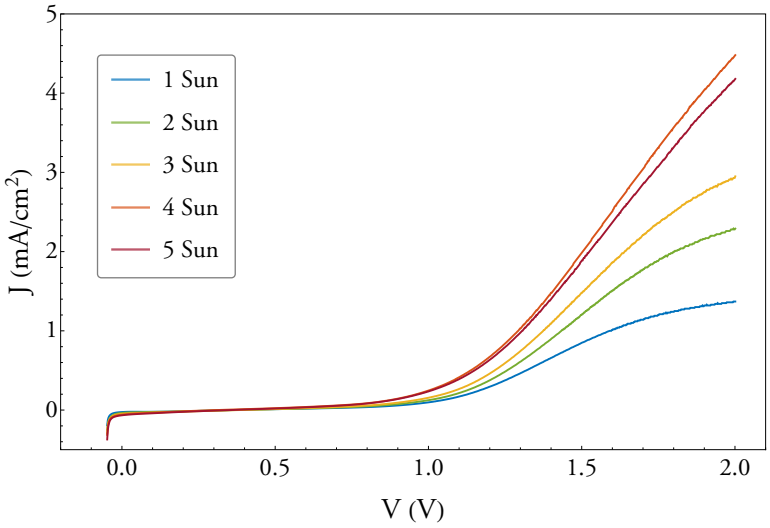

Figure 2.41: J-V curves in real wastewater, two electrodes (Pt) conditions with light intensities from 100 to 500 mW/cm^2; addition of $Al_2(SO_4)_3$ at pH 2.5.

cantly after the addition of $Al_2(SO_4)_3$, despite the change of the pH value, while the currents noticeably rose thanks to the decrease of the solution resistance. Anyway, considering the three graphs (Fig. 2.39, 2.40, 2.41), the improvement in the photocurrent response for the higher light intensities has to be underlined. To conclude, considering the photoconversion of the electrochemical anodized WO_3, a wide spectral sensitivity is measured, with the maximum of the IPCE of the order of 50% and a photoaction onset at 480 nm (Fig. 2.42).

2.3.4 Optical characterization

The optical characterization was carried out in order to have a comparison between TiO_2—in particular the N-doped nanosol—and WO_3 on covered by FTO glass substrate, and to estimate the photoanode transmittance spectrum. Data were acquired using the same setup that was exploited for the TiO_2 electrodes, mainly constituted by an Ocean Optics ISP-30-6-REFL integrating sphere and an USB4000 XR1-ES spectrometer, equipped with an optical fiber. As described in Section 2.2.3, the transmittance spectrum was obtained by the ratio between the number of photons acquired by the spectrometer that was shielded or not shielded by the photoanode. Then, the total transmittance of the entire electrode was acquired: this included the absorption of the WO_3, the FTO layer, and the glass substrate, in addition to the reflection contribution of the WO_3 layer, as shown in Figure 2.43 (blue line). Transmittance spectrum was, finally, elaborated to isolate WO_3 absorption contribution (orange line).

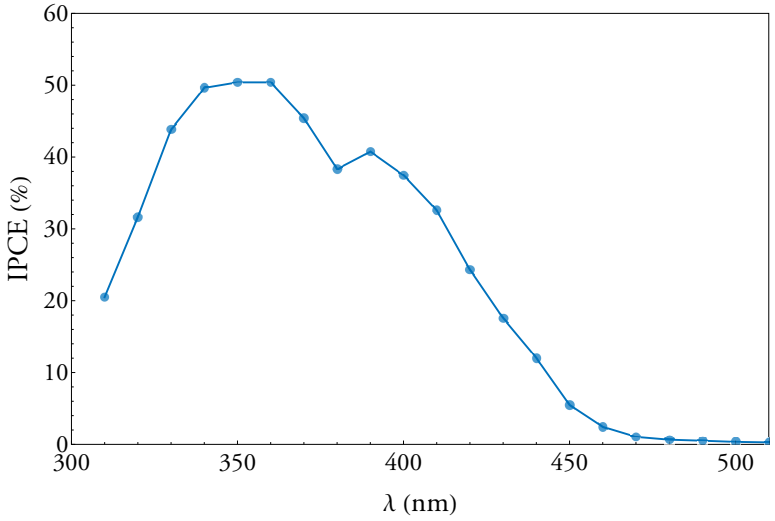

Figure 2.42: IPCE spectrum under 1.5 V vs Pt in neutral (pH 7) Na_2SO_4 electrolyte 0.5 M.

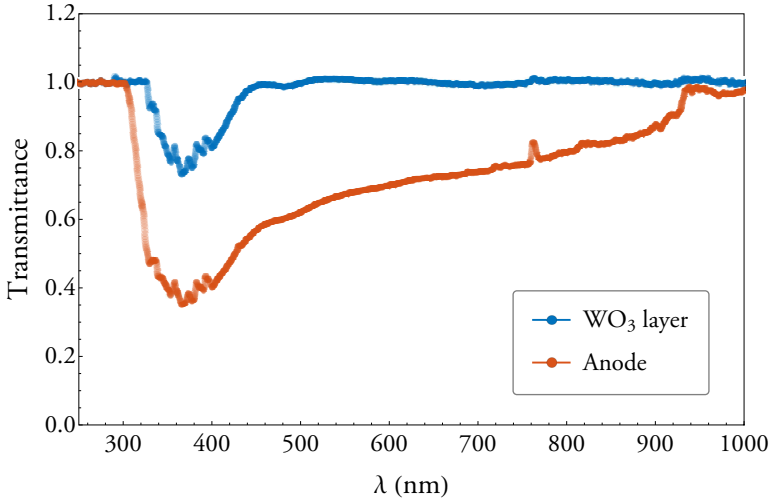

Figure 2.43: Blue curve: total transmittance of the anode that includes the absorption of WO_3, FTO layer and glass substrate, in addition to the reflection of the WO_3 layer. Orange curve: pure transmittance of the WO_3 layer without the contribution from reflection and the other layers. Adapted from [34].

The data displayed an average transparency of the colloidal WO_3 photoanode of 32% of the incident radiation, with an absorption peak at ∼370 nm. To conclude, differently from TiO_2, WO_3 was active until ∼470 nm, working in a wider range of natural sunlight (∼ 15% at AM 1.5).

2.4 Conclusions

In this chapter, the features of TiO_2 and WO_3 as photoanode materials have been studied. In particular, the possible techniques that can be employed to improve their efficiency were described, and their results were discussed.

The first step concerned the attempt to improve the visible absorption of a TiO_2 nanosol exploiting doping with nitrogen. Electrochemical and optical tests have been carried out to observe the possible activation of this photocatalyst in the visible part of the spectrum. Unfortunately, the N-doped TiO_2 showed worse efficiency with respect to the sol-gel TiO_2 and WO_3. This result has been probably due to the too thin layer, maybe because of an incorrect deposition method, and for an insufficient spectral response to visible frequencies.

Since its visible absorption makes it suitable as photoanode within solar devices, WO_3 has been investigated as an alternative photocatalytic material. Several realization techniques have been discussed, among which the sol-gel method and the solvothermal deposition on glass, and the electrochemical anodization of metallic tungsten. Morphological, electrochemical—JV curves and IPCE spactra—and optical measurements have been considered to test the photocatalytic performances. High photocurrent values—in the range of 1–5 mA/cm^2—have been reached in the case of all the deposition techniques thanks to a good nanostructuration of the layer surfaces and thanks to a good photoconversion—more than 50 %—which exploited also part of the visible spectrum until $\sim$ 480 nm.

To summarize, in Figures 2.45 and 2.46 are reported the characteristic curves that have been carried out considering the diverse methods. The measurements have been performed following the same test conditions:

- configuration of the apparatus: three electrodes vs SCE;
- pH value, considering a neutral (pH 7) and an acidic (pH 0) environment;
- electrolyte concentration 0.5 M;
- and illumination intensity of 100 mW/cm^2 (AM 1.5).

In these final results, back and front (Scheme in Fig. 2.44) tests on the electrodes were performed in order to study if the film thickness could be sufficient to allow for a good harvesting of solar photons without jeopardizing charge collection. However, in case of the metallic electrodes the back tests were not possible, thus the reported curves in Fig. 2.46 are the same of those displayed in the front case (Fig. 2.45).

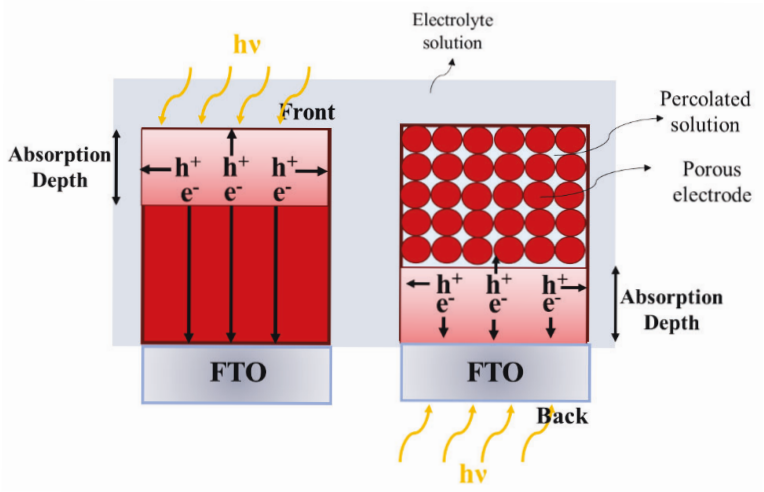

Figure 2.44: Schematic representation of the electron/hole transport under front and backside illumination.

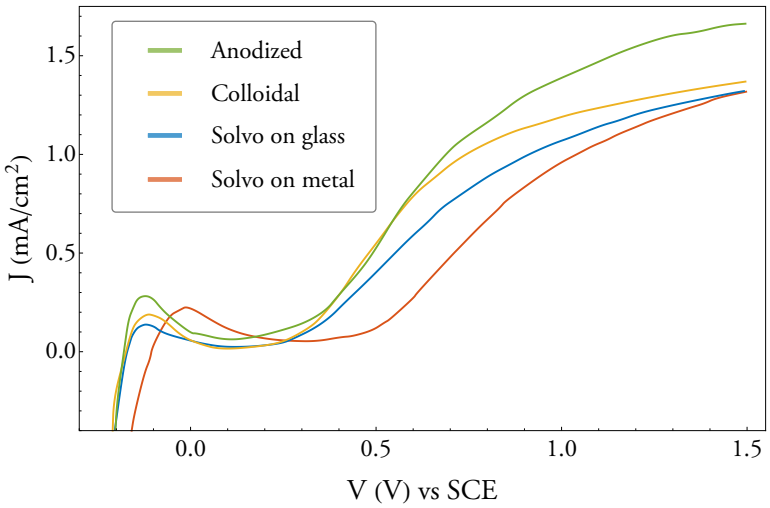

Figure 2.45: Front illumination of WO_3 electrodes at 100 mW/cm^2 (AM 1.5) intensity, in three electrodes conditions, and in neutral environment (pH 7) of Na_2SO_4 0.5 M. Comparison between the deposition methods: electrochemical anodization (green), colloidal sol-gel (yellow), solvothermal on glass (blue), and solvothermal on metal (red).

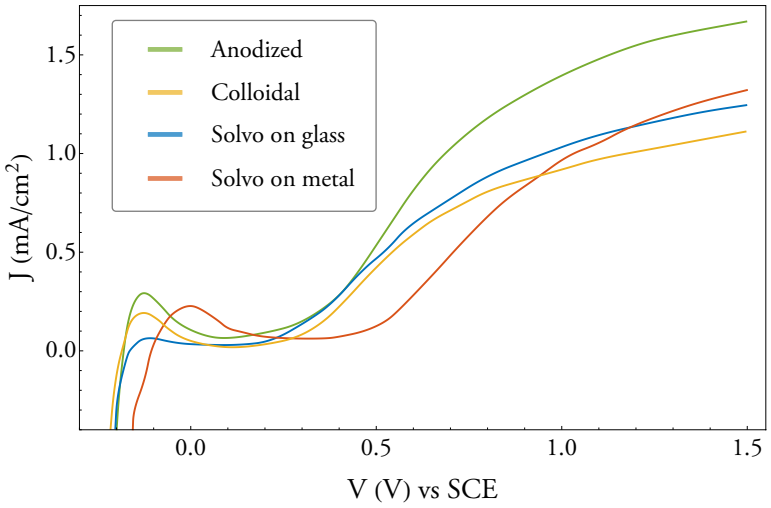

Figure 2.46: Back illumination of WO_3 electrodes at 100 mW/cm^2 (AM 1.5) intensity, in three electrodes conditions, and in neutral environment (pH 7) of Na_2SO_4 0.5 M. Comparison between the deposition methods: electrochemical anodization (green), colloidal sol-gel (yellow), solvothermal on glass (blue), and solvothermal on metal (red).

From graphs 2.45 and 2.46, it is highlighted that both the front and the back electrodes performances were coherent referring to the maximum photocurrent values and the relative V_{oc} values. This confirm a good charge transport within the electrodes.

The same tests were performed exploiting diluted solutions (0.7 mM). In these conditions, the behavior of the electrodes was highly different to those obtained with the concentrated solution: the recorded currents are between 5–7 times lower than those measured in the 0.5 M solution. Nevertheless, also in this case, both in front and back configuration, the performances of the electrodes are in accordance: this demonstrated that the probable limiting factor in the system was only the resistance of the solution.

The solvothermal technique was attempted also on metallic tungsten substrates, obtaining results not so good as those displayed by the electrochemically anodized metallic W. Indeed, the photocurrents show lower values both in concentrated and in diluted solutions. For this reason, it was decided to employ the anodized electrodes within the solar devices.

To conclude, each WO_3 electrode, which has been realized with the three discussed deposition methods, showed good features to be an efficient active photoanode material for the designed and realized devices. The assembly of the devices are displayed in the next Chapters. Respectively:

– The electrochemical anodization of metallic tungsten showed the best perfor-

mances about the reached photocurrent values, in particular under concentrated illumination conditions. For this reason, the so-called anodized electrodes have been employed in a solar parabolic concentrator device—able to work as photocatalytic system for wastewater treatment—in order to improve the anode performances.

– The glass spheres, due to the improved adhesion of the deposited WO_3 layer via solvothermal methods, have been exploited in the same solar concentrator device, in order to study the electrodes behaviour in flow. The choice of a spherical surface was linked to the increase in active surface exposed to the electrolyte, which corresponds to the wastewater to be treated.

– The colloidal sol-gel electrodes, thanks to their transparency for wavelength above the 470 nm and the good adherence to FTO, have been assembled in single element devices in a tandem cell configuration with photovoltaic cells. Each element has been part of a modular array building-up a stand-alone photocatalytic reactor. The described single element, thanks to the cell configuration, was able to allow an additional production of hydrogen, in addition to the use for the wastewater treatment.

Each electrode has been tested considering the photodegradation of several drugs, which, to date, are unfortunately present in the environment. In the following chapters, the design and the realization of the photocatalytic solar devices are presented, sustained by the photodegradation tests performed in our laboratories.

CHAPTER 3

Photocatalytic solar concentrator: assembly and photodegradation tests

As introduced in the Section 1.3, parabolic-trough concentrators are the most promising type of concentrating solar reactors for wastewater treatment. These systems can be defined as parabolic reflective surfaces able to concentrate the sun radiation on a focal line, where the wastewater flows in a tubular reactor [38].

In this Chapter, the realization of a parabolic solar concentrator for wastewater treatment is presented. The described device has been planned starting from a previously designed system, which was built for architectural integration with the aim of energy conversion, from solar into electrical one. The modifications applied to the solar device allow its exploitation in the waste-water treatment field. As described in the previous Chapter, WO_3 was used as active material to realize the electrodes for the photocatalytic process. In this case, the glass spheres covered via sol-gel and solvothermal methods, and the electrochemical oxidized metallic tungsten were planned to be integrated into the parabolic solar concentrator as electrodes.

After the parabolic concentrator description, the photodegradation tests, which were carried out on several drugs by exploiting the WO_3 glass spheres and the tungsten foils, are presented. Finally, Chemical Oxygen Demand (COD) abatement is shown.

3.1 The parabolic solar concentrator

The parabolic solar concentrator was designed starting from an already planned system for electrical energy production exploiting solar radiation. The described device was realized during last years within the Sensor and Semiconductor Laboratory (SSL) of the Physics and Earth Science Department of the University of Ferrara and is based on a patent deposition [92].

The Solar F-Light® for electrical energy production

The device, named Solar F-Light®, is a unique parabolic linear solar concentrator that integrates a sun-tracking system (Fig. 3.1). It provides electricity generation, sun shading, and architectural illumination. Indeed, during the day, it can convert solar energy into electrical one, powering lamps for the night-time illumination. In particular, it can be located where the electrical energy distribution network is absent, i.e. particularly difficult-to-reach and/or mountainous places. This feature could be considered also in case of water treatment, for those regions where the abundance of the solar light go together with the absence of power and wastewater-treatment plants.

The Solar F-Light® is a parabolic linear trough with single-axis tracking having an optical concentration factor of 20×. The structure consists in an extruded aluminum profile, 1500 mm long, having an f-number of F/0.5. A high-reflectivity aluminum foil coated by Ag via PVD (Physical Vapor Deposition) acts as a mirror surface (reflectance about 95%) and is applied on the parabolic trough to achieve the optical concentration. The array of solar cells lies in the focal line of the parabolic trough and, as can be observed in Figure 3.2 a, its position is optimized to enhance the angular acceptance of the system and to ensure uniform solar irradiance impinging on the solar cells. Each PV module is composed of 5 connected receivers of 30 monocrystalline silicon solar cells 0.8 cm × 0.8 cm each one. In addition, in each receiver the solar cells are arranged in

Figure 3.1: Picture of a Solar F-Light® concentrator for electrical energy production.

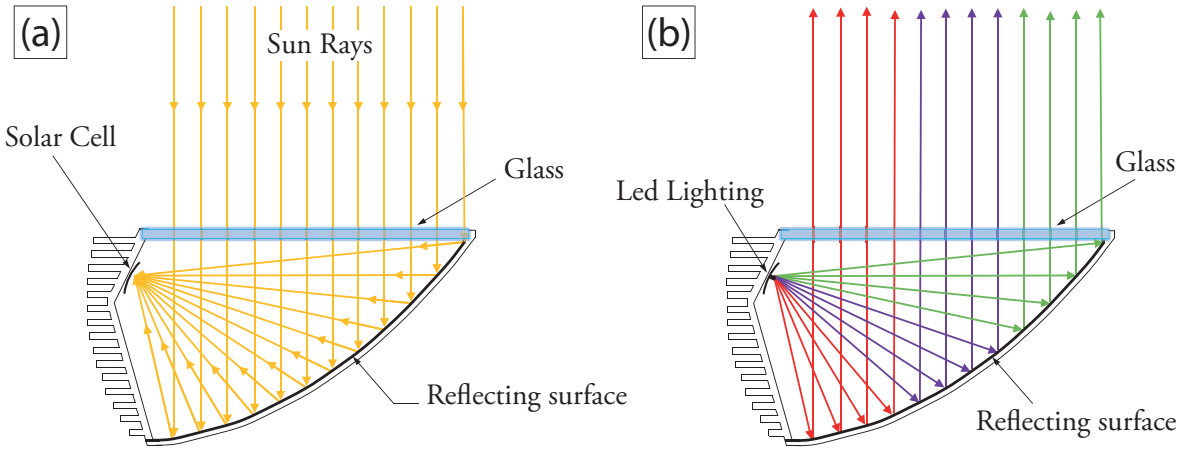

Figure 3.2: Cross section of the Solar F-Light®: a) in the daily and b) in the nocturnal operating situation.

6 groups of 5 parallel connected cells, while the groups are connected in series. In close proximity of the PV array, each receiver is equipped with 5 (3-chip) LEDs, white or RGB (red-green-blue) depending on the necessity, for a total of 25 LEDs per module. Exploiting the illumination by the LED devices, the Solar F-Light® can be used for indoor and outdoor direct or diffuse lighting in a nocturnal operating configuration (Fig. 3.2 b), in particular when the modules are installed on building façades, where can act also as solar louvers.

The tracking system of the Solar F-Light® consists in a two-quadrant sensor mounted on a printed circuit board. This latter is completely integrated in one module end cap. In particular, the tracking system is composed by three photodiodes, a voltage comparator, a logic unit, and a motor drive. In Figure 3.3, the picture (a) and the block diagram (b) of the tracking system are shown. The photodiodes convert the solar radiation impinging on them into a current that is proportional to the radiation intensity. Then, the current is amplified and transformed in a voltage signal. The comparator compares the signal coming from the photodiodes and send the output signals to the logic unit, which communicates with the motor drive. Finally, the motor drive operates the motor depending on the operation required to point the solar module perpendicularly to the sun. In order to reduce the power consumption, the sun tracking system is deactivated when the outdoor illuminance decreases below the 1 W/m^2 threshold. This is achieved by a dedicated circuit equipped with an IR-sensitive photodiode facing the interior of the Solar F-Light® concentrator. The electronic circuit is also equipped with a RF receiver to switch the modules from auto-tracking to manual movement, useful to control sun shading and lighting modes.

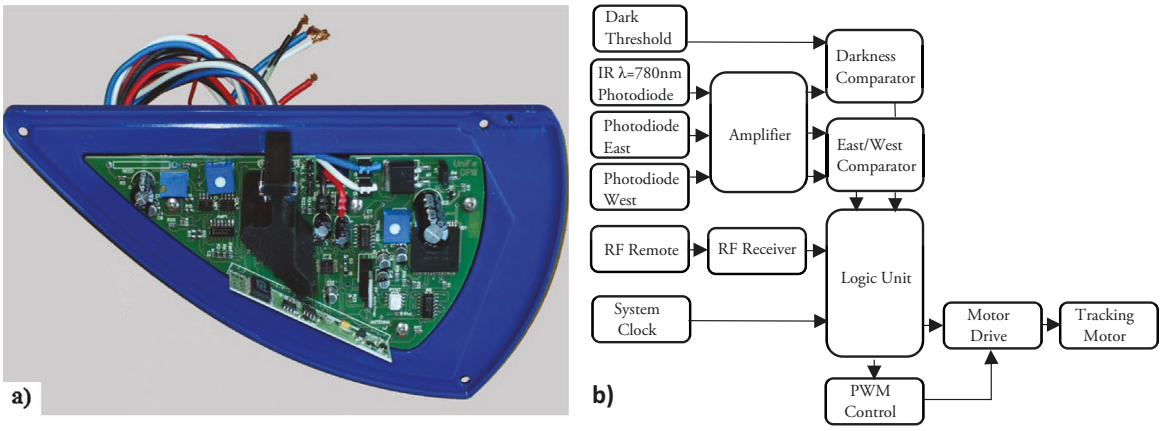

Figure 3.3: Tracking system of the Solar F-Light®: a) picture of the system on the printed circuit board, and b) block diagram.

The actuator of the tracking system is a 3 W electric motor that can move up to 12 modules at the same time connected each other via mechanical joint. When several modules are kept in motion by the same motor, the power consumption needed for tracking is very low. In addition, in this case only the first module, i.e. the one directly connected to the motor, needs to be equipped with the two-quadrant sensor.

The Solar F-Light® concentrator has been designed also in a thermal version to produce hot water, using a 10 mm outside diameter, black-anodized, metal pipe, positioned in the focus of the parabolic mirror. To reduce the heat conduction, each pipe has to be sustained on the focal line by a set of thermally insulated clips. Convection losses are minimized by the presence of stagnating air within the module, while radiative losses can be reduced by the use of solar selective coatings. Neglecting the radiative losses, which correspond to the 1%, the calculated single-pass temperature increase for water at 20 °C, at flow rate of 1 l/min is about 13 °C. The equilibrium temperature of the hot fluid is 53 °C in summertime (external temperature of 28 °C), while it decreases to 33 °C in wintertime (external air temperature of 7 °C) [93].

The Solar F-Light® for water decontamination

Within this thesis work, the Solar F-Light® concentrator was especially modified to allow the water decontamination in flow (Fig. 3.4). As introduced, starting from the external aluminum profile, the PVD Ag-coated mirror was applied on the parabolic trough to achieve the incident solar radiation concentration along the parabolic focal line. In this water-decontamination version, the water flows within the module through a 22 mm outside-diameter glass pipe placed along the focal line, as in the case of the

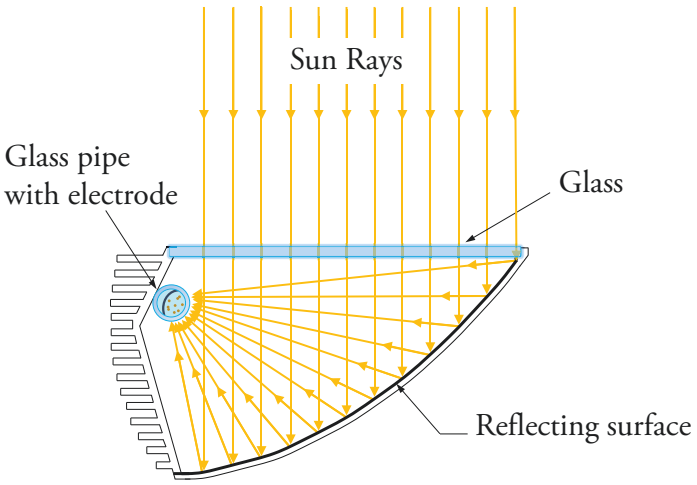

Figure 3.4: Cross section of the Solar F-Light® for wastewater treatment. The sun rays impinge on the glass tube inside which the photo-excited electrode (in gray)oxidizes the micropollutants molecules (in brown)

thermal version. Differently from the thermal device, the pipe is made of borosilicate glass (Favs s.r.l scientific equipment, Italy) since it resists to temperature leap, thanks to the minimal thermal expansions. Each pipe was 1140 mm long: this length is mandatory to ensure that the tube could be inserted inside the module, leaving the necessary space for the super-rapid fittings, which connected the glass tube to nylon (Rilsan) pipes to allow the water to circulate. To accurately place the glass tube along the focal line, transparent supports made of PMMA were positioned inside the module.

The nylon pipes exit at the two lateral ends of the module through PVC plugs specifically designed and manufactured to seal the module. The caps can be assembled to fix the device to the structure that supports one or more devices. In addition to the caps, the module was also sealed by a front glass that closed the extruded aluminum profile, thus preventing the water leaks and the soiling of the mirror surface.

The functioning of the assembled modules was tested in relevant environment and exposed to the sun (Fig. 3.5 a) to perform photodegradation measurements on micropollutants, in particular on drugs.

In order to recirculate the water inside the module, a pumping system consisting of pipes, a tank containing the water to be treated, and an immersion pump was assembled, as shown in Figure 3.5 b. The system was inserted inside a structure sheltered from the weather. The pump was externally power supplied, and the flow and temperature of the water could be controlled. In particular, the temperature was measured by a thermometric probe since the water, when exposed to concentrated solar radiation,

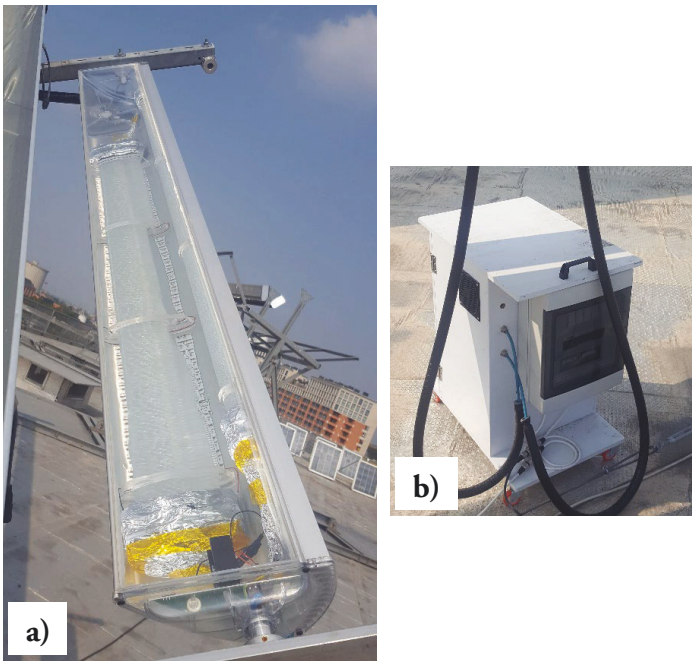

Figure 3.5: Picture of the assembled system exposed to the sun: a) the module, and b) the pumping system

heats up. This functionality can be exploited from an industrial standpoint as solar thermal system. Considering the data obtained in laboratory and the features of the system, an estimate to scale up the solar concentrator devices foresees the treatment of 1 m^3/h of waste water through the exploitation of 10 m^2 of collecting surface. This means that, considering a direct radiant power of the sun equal to 850 W/m^2 and a thermal conversion efficiency equal to 25%, as an added value to the decontamination process, there is an increase of about 30 °C every m^3/h of treated water.

3.2 Photodegradation tests with covered-by-WO_3 glass spheres

3.2.1 Experimental

The photodegradation tests that are discussed in the following Section, and repeated in case of anodized and sol-gel WO_3-on-FTO layers, were performed on several new emergent micro-pollutants, in particular on drugs. Degradation tests were carried out through a collaboration with the Analytical Chemistry group of the University of Ferrara. Following, a list of the analyzed drugs is reported:

- Atenolol (99% purity, Aldrich). It is a beta blocker medication primarily used to treat high blood pressure and heart-associated chest pain.
- Carbamazepine (98.5% purity, Aldrich). It is an anticonvulsant. It works by decreasing nerve impulses that cause seizures and nerve pain, such as neuralgia and diabetic neuropathy.
- Levofloxacin (>98% purity, Fluka). It is a fluoroquinolone antibiotic used to treat different types of bacterial infections.
- Ketoprofen ($\geq$ 98% purity, Aldrich). It is a nonsteroidal anti-inflammatory drug and it works by reducing hormones that cause inflammation and pain in the body.
- 4-Hydroxybenzaldehyde (98% purity, Aldrich). It is a compound widely used as starting material for polymers and pharmaceuticals.

These compounds are barely eliminated by the traditional—biological and chemical—methods of the current wastewater treatment plants. For this reason, the photodegradation analysis was focused on them.

The samples were analyzed by High performance Liquid Chromatography (HPLC) grade acetonitrile (ACN), purchased from Merck (Darmstadt, Germany). A HPLC/DAD (Waters, MA, USA pump:Waters 515, DAD:Waters PDA 996) was employed under isocratic elution condition. The eluent was 18 : 82 ACN : phosphate buffer 25 mM at ph 4 and 60 : 40 MeOH : phosphate buffer 2 mM at pH 3.3. The flow rate was 1 ml/min. The column was a C18 Kromasil Eternity 150×4.6 mm and the injection volume was 20 μl for all standards and samples.

When necessary, a diluted aqueous solution of sulfuric acid was added to adjust the pH of the drug solution to 6. The saline concentration was chosen to reproduce the average salinity of fresh-water. The drug solution pH was measured by a combined electrode connected to an Amel pH-meter.

3.2.2 Colloidal WO_3 layer over glass spheres: photodegradation tests and discussion

In the first configuration, the Solar F-Light® concentrator for waste-water treatment was assembled using the colloidal WO_3 layer over glass spheres as active material for the photocatalysis process. Firstly, the measurements were performed in laboratory, considering static conditions (Fig. 3.6). The glass spheres, covered by colloidal WO_3, were inserted within a 150 mm long tube with 22 mm in diameter to simulate a section of the glass pipe of the solar concentrator. Considering the static conditions, the tube

Figure 3.6: Picture of the lab scale photodegradation apparatus with colloidal WO_3 spheres in static conditions

Table 3.1: Photodegradation tests in on Atenolol solutions of 10 mg/l using 0.7 mM Na_2SO_4 as a support electrolyte under illumination of 100 mW/cm^2.

N° Coats	H_2SO_4treatment	Irradiation time (h)	Degradation (%)
1 coat	NO	1	17.5
1 coat	NO	2	42.5
2 coats	NO	1	60.7
2 coats	NO	2	65.6
1 coat	YES	1	90.0
2 coat	YES	1	100.0

was closed at the ends. The tests were carried out on Atenolol solutions with a concentration of 10 mg/l using 0.7 mM Na_2SO_4 (Aldrich, purity 99%) as a support electrolyte. The abatement kinetics were observed by considering diverse kind of illumination conditions: via 380 nm and 400 nm LEDs, and via solar simulator (by using the Xe-lamp that has been introduced in the Section 2.2.2). The best results were obtained with the solar simulator and are reported in Table 3.1. Also the tests performed with LEDs at 400 nm gave good results, i.e. an abatement of more than 50% of atenolol, but in longer time (40 h).

The measurements with the solar simulator were performed with irradiation times of 1 and 2 h, under illumination of 200 mW/cm^2. The photodegradation efficiencies of the Atenolol with the colloidal WO_3 on spheres in static condition are reported in Table 3.1.

As can be noticed, an improvement of the photodegradation was obtained both in case of prolonged illumination time—with an abatement from 17.5% in 1 h to 42.5% in 2 h—and of double coating. These features were further enhanced by the treatment with H_2SO_4; this allowed to reach a complete photodegradation of the atenolol. Indeed, as already introduced in the electrochemical characterizations in Chapter 2, the H_2SO_4

is a typical compound used to enhance the photocurrent and, hence, the photo-activity of the electrode. In particular, it allows to remove ionic residues from the sol-gel synthesis, while preserving WO_3 from dissolution during surface cleaning step. In this way, more is the photocatalytic capacity of the electrode, more oxidant molecules are produced in contact with the electrolyte, and more the organics are photo-degraded.

Due to the promising results in static conditions, the Solar F-Light® module for wastewater treatment was assembled including the covered-by-WO_3 glass spheres within the pipe. Thus, the same measurement were carried out in flow under solar illumination. Unfortunately, considering a starting concentration of 10 mg/l, only the 20% of atenolol photodegradation was obtained in several hours of solar illumination. This result was a consequence of the detachment of the WO_3 material from the substrate when immersed into an electrolyte in flow, but it also was the demonstration that, in case of the active material absence, an effective micropollutant oxidation has not been possible with the only contribution of the solar radiation. Indeed, the direct irradiation of the drug solution in absence of the WO_3 leads to a negligible degradation. Therefore, it is possible to conclude that the observed degradation process shows a photocatalytic nature.

To find a solution to the colloidal WO_3 detachment from the bare glass surface—i.e. not covered by the FTO film—the solvothermal method was selected as an alternative technique to obtain a better adhesion.

3.2.3 Solvothermal WO_3 layer over glass spheres: photodegradation tests and discussion

The measurements performed considering the solvothermal technique were carried out in laboratory, firstly by testing the adherence of the solvothermal layer on the glass electrodes covered by FTO (the results were introduced in the Section 2.3.3), and then by testing with different flow rates the coating adherence over the sphere. In this case, the WO_3 detachment was not observed thanks to the stronger interaction with the glass surface established with the slow growth during the solvothermal process, and by the addition of the TiO_2 adhesion layer, which also improved the photocurrent efficiency of the electrodes, as shown in the Section 2.3.3 in Figure 2.38. Therefore, the photodegradation tests were carried out in flow condition by assembling the apparatus shown in Figure 3.7.

The obtained results on the abatement tests are reported in Figure 3.8, which shows the ratio between the initial and the final concentrations C/C_0 as function of the irradiation time.

Here, the glass tube that simulated the Solar F-Light® glass pipe was not closed at the end, but was connected by two PVC tubes with a small pump and with a bubbler. The latter contained the electrolyte solution with the micropollutants. The glass spheres covered by solvothermal WO_3 were inserted into the glass tube, and the pump allowed the circulation of the solution. In this case, the measurements were carried out on Atenolol, Carbamazepine, and Levofloxacin solutions of 5 mg/l, respectively. The abatement kinetics were observed by considering illumination of 400 nm LEDs: this wavelength was chosen in accordance to the second %IPCE peak of the solvothermal WO_3 electrode, which is shown in Figure 2.40. In this case, the first and higher peak was not considered because of its extension in the UV range of the solar spectrum. These measurements were carried out in order to test the solvothermal-WO_3 features in case of LED illumination. Indeed, because of the impossibility for a solar concentrator to work during the night or in conditions of sun absence, it is possible to integrate a LED stripe within the modulus, as in case of the Solar F-Light® that was designed for electrical energy production. In this way, the photodegradation process could occur during the day, by exploiting the solar radiation, and during the night, by exploiting the LED illumination.

As can be observed, the worse abatement was obtained in case of Carbamazepine,

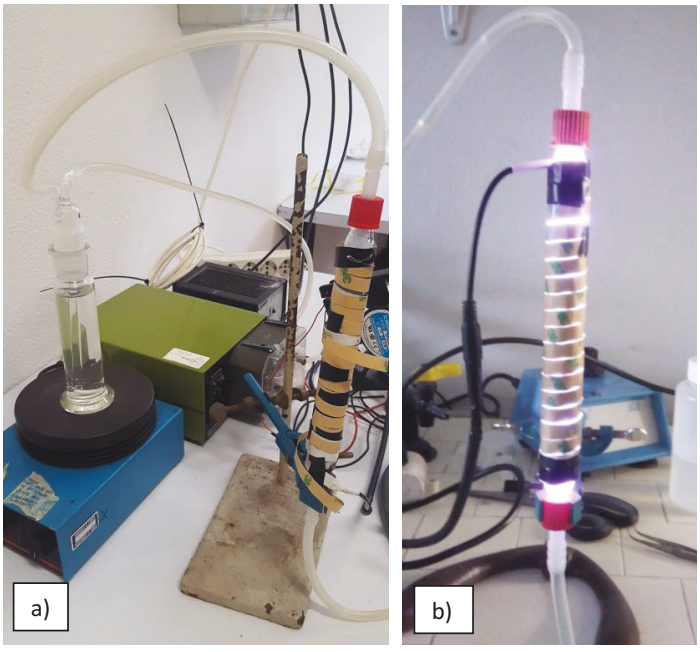

Figure 3.7: Picture of the photodegradation apparatus with solvothermal WO_3 spheres in flow conditions (a), and with LED illumination (b). This setup was assembled by the Analytical Chemistry group to monitor the degradation kinetics by HPLCs.

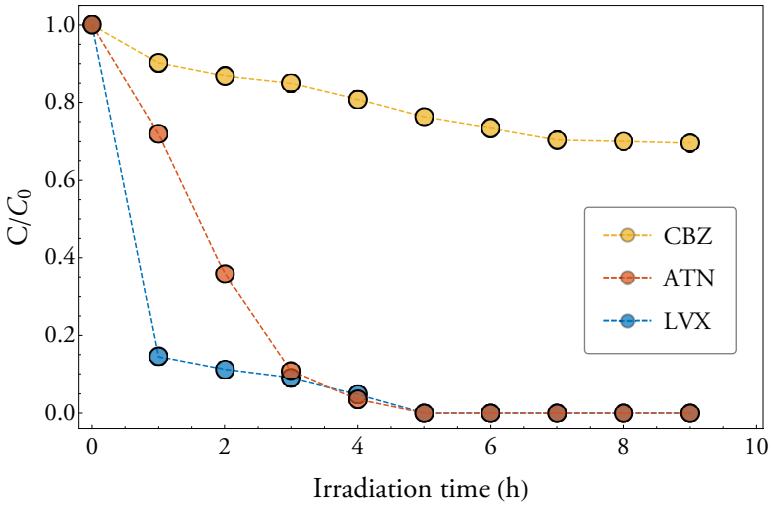

Figure 3.8: Photodegradation tests on Carbamazepine (CBZ, yellow), Atenolol (ATN, orange) and Levofloxacin (LVX, blue).

which was degraded only of the 30% with respect the initial concentration in 9 hours of irradiation. This result does not come completely as a surprise, given the high stability of the CBZ molecule. Differently, in case of Atenolol and Levofloxacin, the data showed a percentage of abatement near to the 100%. In particular, they showed more than 90% of photodegradation already in the first three hours of irradiation.

The same tests were performed also in case of an initial concentration $[C_0]$ of 10 mg/l, obtaining the same photodegradation results.

3.3 Abatement test with electrochemically anodized WO_3

Concerning the photodegradation measurements performed by using the electrochemical anodized WO_3 lamina, tests were carried out on several drugs, among which Atenolol, Carbamazepine, Levofloxacin, and Ketoprofen. In addition, Chemical Oxygen Demand (COD) abatement was considered. In particular, these photoelectrochemical degradation tests were performed by using real wastewater solutions. The rationale is to apply the photoelectrochemical process also to organic rich wastewater, not only to tertiary potabilization process, in order achieve a first remediation of wastewater. That is why also COD was analyzed.

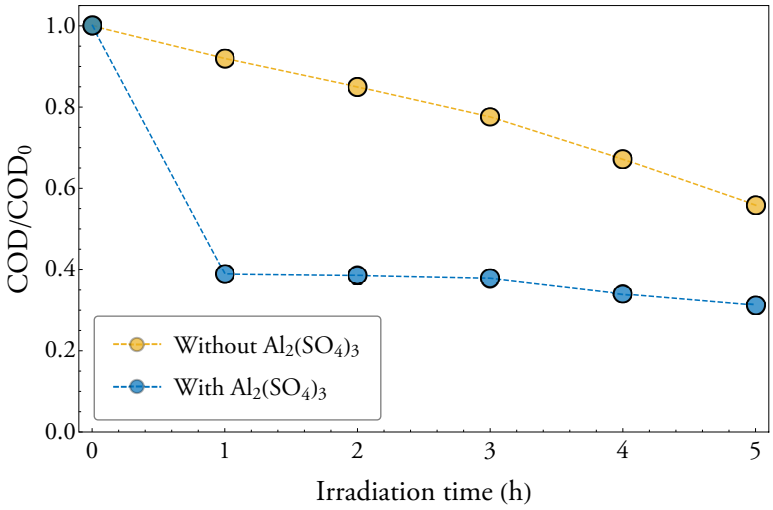

Figure 3.9: COD abatement on waste-water samples with anodized WO_3, without (yellow) and with (blue) the addition of aluminum sulfate.

3.3.1 COD abatement: results and discussion

In environmental chemistry, in order to quantify the amount of oxidizable pollutants that are present in water or wastewater, the most commonly used parameter is the Chemical Oxygen Demand (COD). Indeed, COD is part of the chemical characteristics of the wastewater and it is relative to the degradation processes of organic substances. This parameter represents the amount of oxygen per unit volume—and therefore the concentration—required to chemically oxidize organic, biodegradable, and non-organic substances present in wastewater. Its decrease, in percentage, determines the decrease of the organic load present in the wastewater. COD is commonly expressed in mass of oxygen consumed over volume of solution, that is in mg/L; however, it is also expressed by percentage [12]:

$$\text{Removal efficiency}\% = 100 \cdot \left(1 - \frac{[C]}{[C_0]}\right), \tag{3.1}$$

where $[C_0]$ and $[C]$ are the initial and the final concentration, respectively.

For the COD abatement tests, the measurements were carried out on a set of waste-water samples provided by the local water treatment and management authority, HERA. The wastewater samples came from hospital wastes; these were pre-treated by HERA with mechanical and chemical processes to obtain a clear water without sludge.

To assess the photodegradation of the pollutants, the tests were carried out under photoelectrochemical conditions in a two-electrode configuration (volume 10 ml) under

potentiostatic conditions controlled by an Autolab PGSTAT302N potentiostat. The working electrode was the anodized WO_3, while a Pt grid was used as counter electrode, both featuring area of 1 cm^2. A Xe ABET LS 150W sun simulator of 100 mW/cm^2 provided with a 1.5 Air Mass filter was used as illumination source with irradiation time up to 5 h at 500 mW/cm^2. The Figure 3.9 shows the ratio COD/COD_0 between the initial and the final concentrations of COD as function of the irradiation time. The measurements were performed on the bare wastewater (yellow line) and with the addition of aluminum sulfate $Al_2(SO_4)_3$ (0.1 M).

It can be observed that, in the absence of the $Al_2(SO_4)_3$ as electrolyte, the speed of photodegradation of pollutants slowly decreased and after 5h the abatement of the COD was about 45%. Differently, in the presence of $Al_2(SO_4)_3$, after 1 h of irradiation a COD abatement of more than 60% was evident. However, by prolonging the irradiation time, a further increase of the COD abatement was not obtained. Thus, this explained the non-correlation between the charge exchanged and the abatement of the COD. Even other measurements at 5 or 6 hours showed that it is not possible to break down more than 60% of the COD. The reason is not yet clear. However, one of the possible factors could be the presence of a high quantity of sulphates that competed with the oxidation of pollutants, particularly when the concentration of these latter tended to decrease dramatically.

Nevertheless the abatement of 50/60% COD in real wastewater is a significant achievement in view of the process scale up within an industrial context. The reasons behind the incomplete COD abatement, while the photoanode is still fully functional, are still under investigation, and demand an accurate chemical characterization of the main components present in the analyzed wastewater samples, and of the chemical intermediates produced during the photoelectrochemical treatment.

3.3.2 Photodegradation measurements: results and discussion

For the electrochemical anodized tungsten lamina, the measurements were carried out in laboratory with the same analysis method—via HPLC—that has been exploited for the previous photodegradation tests. However, in this case, the tungsten lamina (area 1 cm^2) was immersed in 30 ml of solution within a small glass container.

The abatement tests were carried out on several drugs, such as atenolol (ATN), Carbamazepine (CBZ), Levofloxacin (LVX), and Ketoprofen (KTP). The analyzed drugs, whose initial concentration C_0 was 10 mg/l, were dissolved in aerated aqueous solution containing Na_2SO_4 (0.1 M) and photo-catalytically degraded by comparing the dark

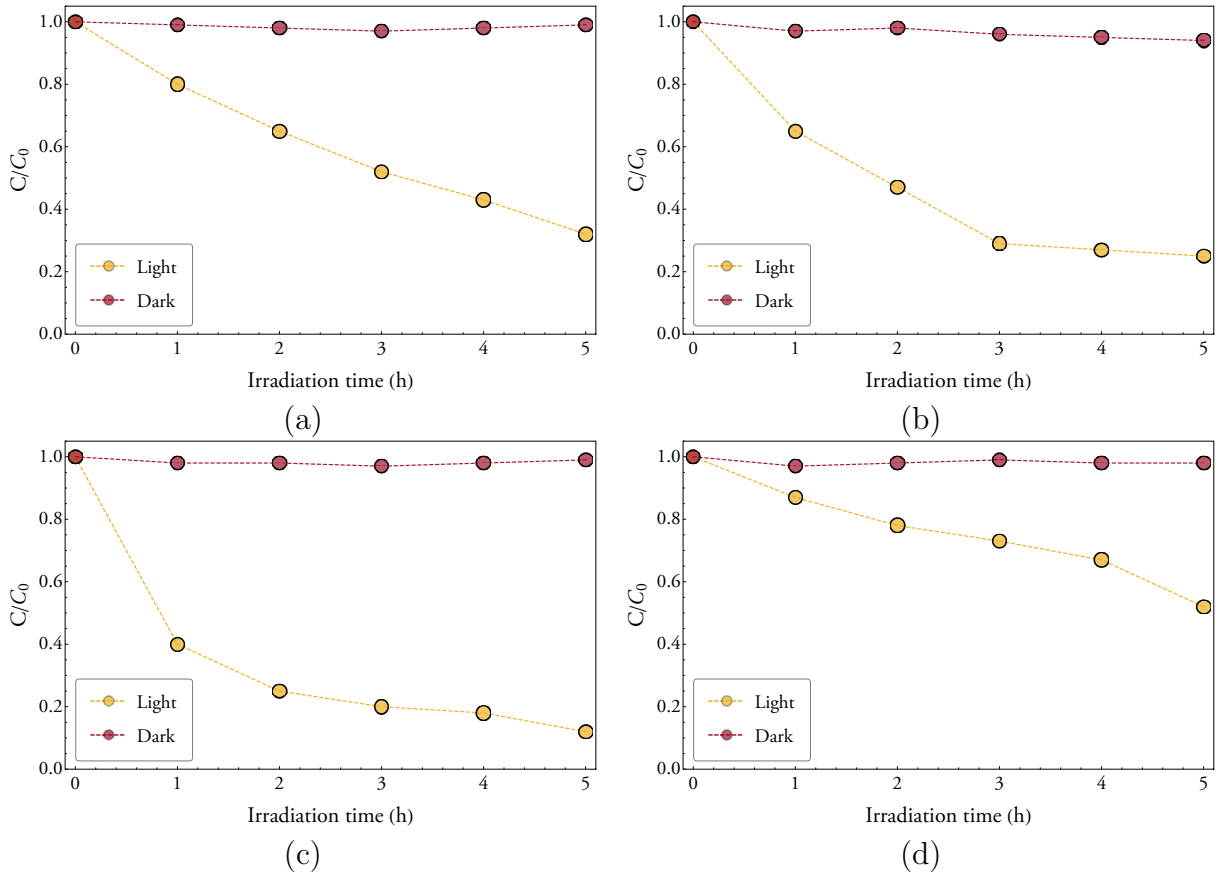

Figure 3.10: Degradation of drugs (C_0 of 10 mg/l) dissolved in aqueous solution (pH 5.1) with Na_2SO_4 (0.1 M) under simulated solar illumination (500 mW/cm^2) in yellow curves with respect to dark conditions (red curves). (a) atenolol (ATN); (b) Carbamazepine (CBZ); (c) Levofloxacin (LVX); (d) Ketoprofen (KTP).

condition (red line) with respect to the illumination (yellow line) (see Fig. 3.10). The Figure shows the ratio C/C_0 between the initial and the final concentrations as function of the irradiation time. Drug concentration variation in the dark did not exceed the 10%: this was probably due to the surface absorption on the semiconductor. Differently, in illumination condition, the degradation of LVX was almost complete after 5 h, while the ATN, CBZ, and KTP reached the abatement values of 70%, 80%, and 50% respectively.

To date, several tests have been carried out on the photodegradation performances of the electrochemical anodized WO_3, also in comparison with the colloidal one. Indeed, photodegradation efficiencies have been studied, firstly, on suspended WO_3 powder and, then, on the photoactive films deposited of FTO or anodically grown on W foils. From this comparison, the drugs degradation on the suspended powder was faster

than with immobilized WO_3 because of a decreased surface area in the sintered films. Nevertheless, the percentage differences were not so remarkable, but of the order of 10% [78].

Measurements performed by Longobucco et al. [78]—within the research group of the University of Ferrara—shows that the two different electrodes, i.e. the colloidal and the anodized WO_3, display equivalent photocatalytic performances. This suggests the possibility of their customized use depending on their intrinsic characteristics. For example, the colloidal WO_3 can be best employed in those substrates where transparency is important, while the tungsten sintered WO_3 can be best suited for applications demanding conductivity, mechanical flexibility, and resistance to high solar irradiance and temperature. The realized and discussed electrodes were selected for these applications. In particular, the anodized WO_3 lamina was integrated within the solar concentrator module that is described in this Chapter, while the colloidal one was inserted as active material of a solar device based on a tandem cell configuration, for which the transparency to the red part of the solar spectrum was an important feature.

3.4 Conclusions and further works

In this chapter, the Solar F-Light® concentrator for wastewater treatment has been described. The Solar F-Light® is a parabolic linear trough along whose focal line a glass pipe, which contains the active material, is integrated. In this work, the active material concerns, on the one hand, small glass spheres covered by colloidal and solvothermal WO_3, and, on the other hand, electrochemical anodized WO_3 over a tungsten lamina.

Photodegradation tests were carried out on all of the materials in laboratory and under solar illumination condition, with the following results:

- After good results performed on atenolol in static condition, in laboratory, the glass spheres covered by the colloidal WO_3 were integrated in the Solar F-Light® concentrator, in order to test the material in flow, under solar illumination. Unfortunately, a detachment of the WO_3 material from the substrate was obtained.

- Solvothermal technique was selected as a possible solution. In this case, photodegradation tests were carried out in flow conditions with LED illumination in laboratory. The obtained drugs abatement, in particular in case of Atenolol and Carbamazepine, was almost complete.

- In case of the electrochemical anodized WO_3 over a tungsten lamina, in illumination condition, the degradation of LVX was almost complete after 5 h, while

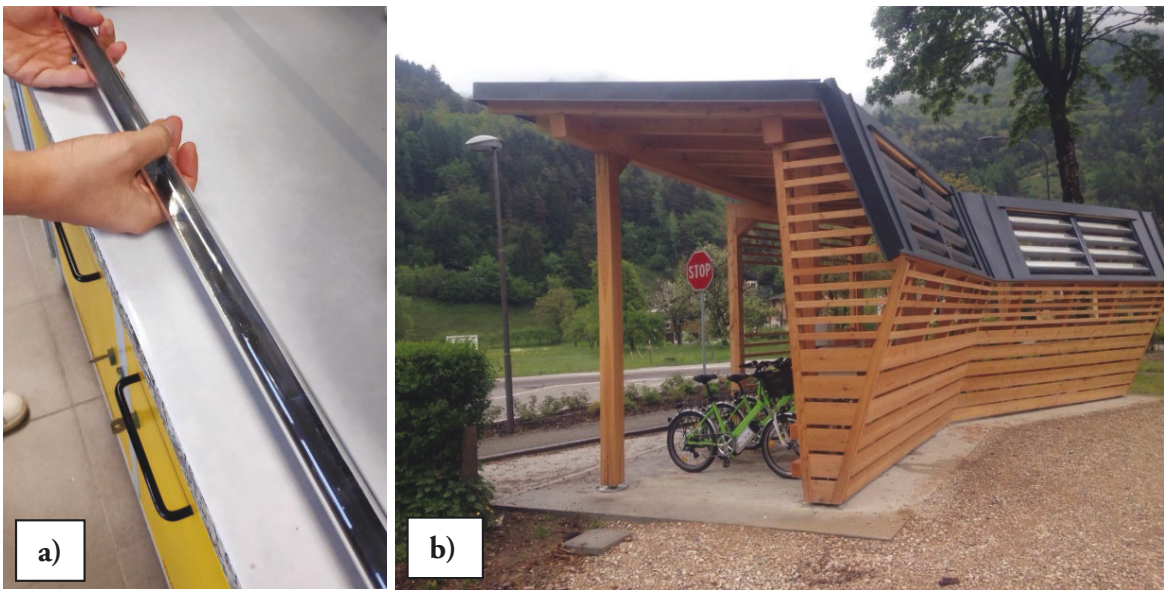

Figure 3.11: a) Electrochemically anodized tungsten lamina integrated in the glass pipe. b) Picture of a projecting roof realized with the Solar F-Light® concentrators for electric energy production.

the ATN, CBZ, and KTP reached the abatement values of 70%, 80%, and 50% respectively. In addition, Chemical Oxygen Demand (COD) abatement was carried out on a set of hospital waste-water samples provided by HERA. In the presence of $Al_2(SO_4)_3$, after 1 h of irradiation, a COD abatement of the 60% was observed, even if the obtained percentage did not increase in the successive hours, displaying, in this way, a stabilization around the 60%.

Typical experiments had a duration of 5 hours, at the end of which the percentage of the abatement was measured. To date, longer experiments (ca. 20 hours) were carried out, aimed at the determination of decomposition drugs intermediates. The results showed a complete mineralization after ∼20 hours.

To date, the WO_3 features are still under investigation. In particular, as introduced in Section 2.3.1, in order to obtain an electrochemical oxidation of a large surface area, the electrochemical recipe was adapted for the anodization of a metallic tungsten strip of ca. 1.5×100 cm^2. The obtained lamina is shown in Figure 3.11 a; however, several improvements have to be studied to allow a scale-up to the industrial scope. Nevertheless, because of the promising results obtained with the solvothermal technique, the WO_3 glass sphere could be produced in a bigger quantity and could be tested in real environmental conditions under solar illumination, using "real" waste-water samples. With this aim, a Crowdfunding Project of the University of Ferrara, named "Beviamo

sicuri: l'energia solare al servizio della decontaminazione delle acque", is arising, in collaboration with the "Terra & Acqua Tech" laboratories. The final goal of the project provides for the realization of a projecting roof (see Fig. 3.11 b) integrating the Solar F-Light® concentrators for the waste-water treatment in a small context, such as the academic one.

CHAPTER 4

The photoelectrocatalytic modular stand-alone reactor

Since it was first reported as a potential photoanode for photoelectrochemical cells in 1976 [94], many aspects of WO_3 have been extensively studied. Latest efforts have been devoted to promote minority carriers collection via nanostructuration, to increase visible absorption via intentional doping, to improve charge separation with heterojunctions, to tailor photocatalytic selectivity toward water oxidation with electrocatalysts, and to enhance WO_3 stability in neutral solution using surface coating [89].

This thesis research provides for the design and the realization of a solar system based on PEC cells, which have been created by exploiting the discussed characterizations and the results concerning the active materials. Indeed, in this chapter, the integration of WO_3 electrodes in a modular stand-alone reactor for solar waste-water decontamination is described. The reactor was composed by single elements. These single devices were based on photoelectrochemical tandem cells, which were assembled including the colloidal WO_3 electrodes as photoanodes. Finally, the photodegradation tests, which were carried out on several drugs, are presented.

4.1 The photoelectrocatalytic reactor: design and realization

As already introduced considering PEC cells, although the efficiency of the photocatalytic effect is effective also with no external action, it extensively increases when the semiconductor is externally biased. From the microscopic point of view, the application of a positive potential to WO_3 should exponentially increase the photoholes surface

concentration, resulting in a parallel increase of the charge transfer rate, and in a higher $^{\bullet}OH$ radicals production rate at the photoactive interface. Consistent with this interpretation, previous experiments [78, 50] were performed both on anodized and on colloidal WO_3 layers. They showed a higher efficiency of the photo-oxidation process that was obtained by exploiting an external bias. During this photo-assisted electrolysis, photogenerated electrons are collected at the ohmic back contact of the photoelectrode and transferred to the counter electrode, where hydrogen can evolve. Photocatalytic degradation, in a open circuit condition, gave good results, as discussed in the previous Chapter. Nevertheless, the drug degradation in case of photo-electrocatalytic conditions reached a higher value, near to a complete abatement of the pollutants.

These results confirmed that higher efficiency of the photo-oxidation process can be obtained by exploiting an external bias, which leads to an increase of the surface photohole density. In addition, considering a PEC cell, photogenerated electrons are transferred to the cathodic compartment where they trigger proton reduction on the metallic cathode. The complete process results in a greater production of $^{\bullet}$OH radicals at the anode, according to Equation 4.1, and the respective proton reduction at the cathode:

$$H_2O + h^+ \rightarrow {}^{\bullet}OH + H^+. \tag{4.1}$$

As just introduced, the photocatalytic effect of the WO_3 can be enhanced by biasing the solar device. However, in case of high bias within liquid electrolytes, polarization effects occur, and the catalytic efficiency is reduced down to a minimum after a few minutes of operation. This limiting effect can be overcame by periodically applying a small reverse potential to the tandem cell [89].

Following, the discussion about polarization processes is presented. In addition, the description of the realized solar system based on a PEC cell is shown. In this case, the active material, integrated within the device, was the colloidal WO_3 produced via sol-gel method over the covered-by-FTO glass substrate. These electrodes were chosen as photoanode components due to their transparency.

4.1.1 Single element and rector design and assembly

The realized device was a modular stand-alone photoelectrocatalytic reactor for which a patent has been deposited [95] during this thesis work.

The prototype was a vertical cylindrical reactor embedded between two PMMA tubes. The PMMA tubes were selected due to the UV transparency of the material. The outer tube had a diameter of 160 mm, while the inner one had a diameter of 120 mm. The gap between the two tubes was used to pump the water from the bottom

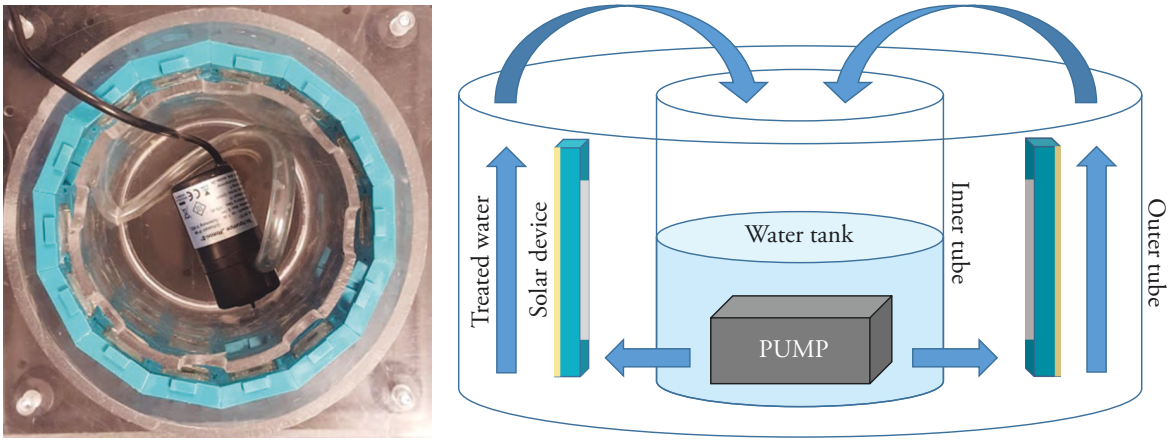

Figure 4.1: On the left: top view of the cylindrical reactor embedded between the two PMMA tubes. On the right: cross section scheme of the reactor, which compries the outer and inner tubes, the pump and the solar devices.

to the top in the reactor, while the internal tube acted as a sink for the treated water (Fig. 4.1).

The cylindrical shape of this system was selected since, during the day, at least a part of the solar system could be always exposed to the direct solar radiation. In this way, a solar tracking system was not needed. The pumping system for the water recirculation could be placed externally or integrated within the cylindrical structure, creating a more compact apparatus (as in the scheme in Fig. 4.1). In addition, it could be powered by an external source, or by a photovoltaic panel making the whole apparatus completely self-powered. For the prototype assembly, a solar-powered high-efficiency (2 W with prevalence of 50 cm) water pump was chosen. The waste-water flux could be adjusted by using the pumping system. It is reasonable to think that in case of laminar flow, the probability that the $^{\bullet}$OH radicals enter in contact with pollutants is greater, making the abatement of COD faster with respect to a turbulent flow.

The reactor was a modular array of PVC frames 30×30 mm^2 building up the cylindrical structure with diameter of 140 mm and thickness of 10 mm. Thanks to the element modularity, the height of the reactor column could be tailored according to the user need by stacking multiple ring-shaped stages of PVC frames. In particular, each element was a completely independent watertight system, composed by a photoanode in a tandem cell (TC) configuration with photovoltaic (PV) solar cells, the electronic components and a metallic cathode. The configuration of the single element and of the reactor was designed by Rhinoceros, a commercial 3D computer graphics

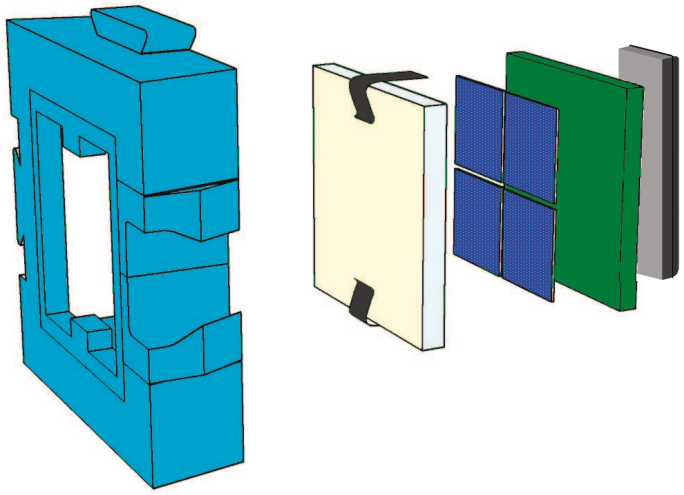

Figure 4.2: Graphic rendering of the single element with distinct components. Following from left to right: the external frame, the photoanode, the PV cells, the printed circuit board with electronic components and the metallic cathode.

and computer-aided design application software. A graphic rendering of the single element with distinct components is shown in Figure 4.2. Following, the working principle of the device is discussed (see Figure 4.3).

The photoanode was composed by colloidal WO_3 layer over the glass substrate, which was covered by the FTO film. The WO_3 film was deposited with an active area of 15×15 mm^2 and a thickness of ∼1.5 μm. The glass substrate was cut by a high-precision dicing machine (DISCO, DAD 3220) with an area of 19.6×19.6 mm^2 in order to be inserted within the PVC frames. The photoanode represented the front component of the PEC cell. When the radiation impinges on the photoanode, the WO_3 is photoactivated by light under 470 nm, thus initiating the photocatalytic process. The %IPCE of the colloidal WO_3 is shown in Figure 2.37 in the Section 2.3.3.

The longer wavelengths could be converted by the PV cells, which were arranged behind the photoanode in a tandem cell configuration. The placement of the solar cells, directly embedded within the single element, was fundamental to avoid the presence of wires and, hence, to prevent corrosion issues, which are likely in an aqueous environment. The PV cells were four back-contact mono-crystalline silicon (c-Si) solar cells (SunPower^{TM} Maxeon C60); they were cut by dicing machine, featuring an area of 8×8 mm^2 each. Then, they were soldered on a Printed Circuit Board (PCB). The cells are connected in series in order to bias the entire device with ∼2.4 V (the minimum is 1.8, which is necessary to bias the tandem cell), without reaching a too high voltage (above 3 V), which could damage the WO_3 layer. As already discussed, by biasing the

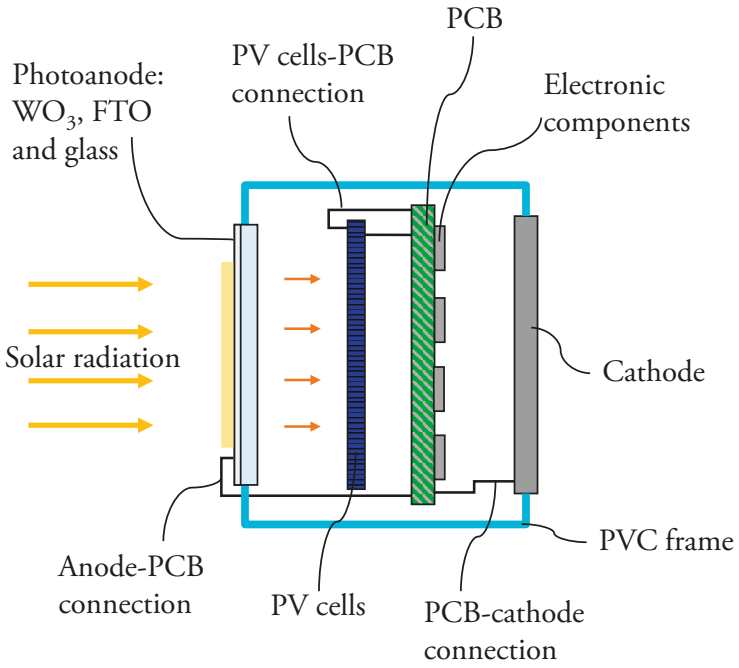

Figure 4.3: Schematic cross section of the solar device, including the components in the tandem cell configuration.

PEC cell it is possible to increase the anode photocurrent and hence the photocatalytic process. Moreover, by coupling the biased tandem system with a metallic cathode it is possible to exploit the electrons collected by the metallic cathode for hydrogen production, which can be considered as an additional value to the process of photocatalysis. In the back front of the single element, the PV cells were connected to the metallic cathode (Ni, Au, Pt). In the realized prototype for the laboratory analysis, a nickel foil (thickness 0.125 mm, purity >99.9%, Aldrich) was used as cathode (area $\sim 25 \times 3$ mm), but, in case of the reactor employment in a real water-mineralization environment, a non-toxic metallic cathode must be used as alternative.

In addition to the tandem cell, electronic components were assembled on the back side of the PCB, behind the solar cells. The photoanode, in particular the FTO film, was connected to the PCB by using two 10×3 mm^2 lamellas of copper covered by tin. This connection allowed the electron transfer from the photoanode to the cathode within an external circuit (but internal to the PVC frame). All of these components were encapsulated by a self-levelling silicone in a watertight frame. In this way, the device became waterproof, resistent to corrosion and to the temperature variation. Each element was a completely autonomous system and was designed and realized in two main different versions.

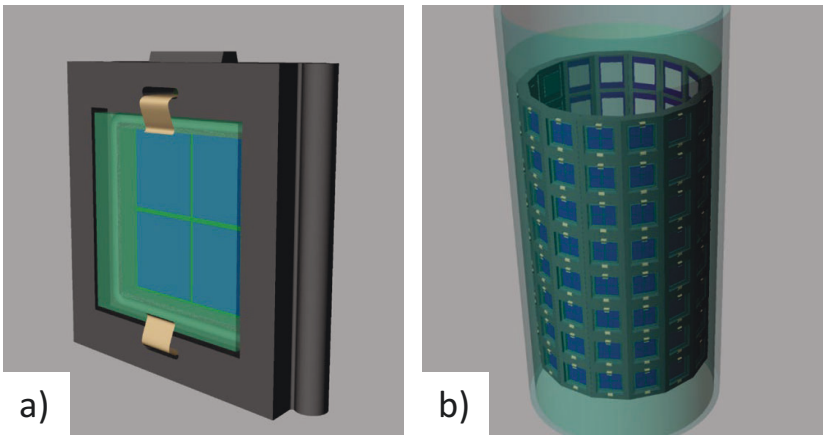

Figure 4.4: Graphic design of the first version of the single element a) and of the reactor b).

The graphic design of the first version is reported in Figure 4.4, which shows both the single element (a) and the entire reactor (b). In this first version of the single device (Fig. 4.5), the external frame was realized via Micro Stereolithography (JustPrint3D s.r.l., Italy) by using a white synthetic resin. In this case, the PCB was realized in order to keep the polarization constant between the anode and the cathode and in order to work with the four Si-solar cells in series or in parallel in pair by the placement of suitable resistances.

In the second and final version (Fig. 4.6), the frame was realized in light blue natural PVC (Defi International, China) by using a mold. The PVC frames were expressly designed to assemble 14 single elements in a ring, exploiting the wedges and

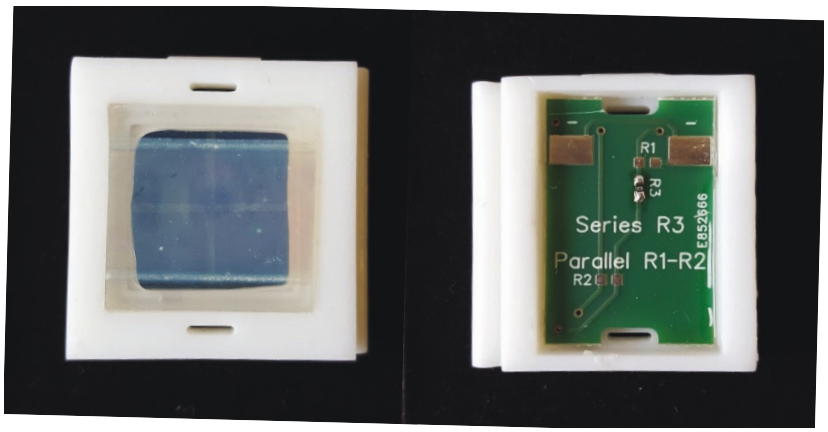

Figure 4.5: Picture of the first version of the single element, both in the front (on the left) and in the back side (on the right).

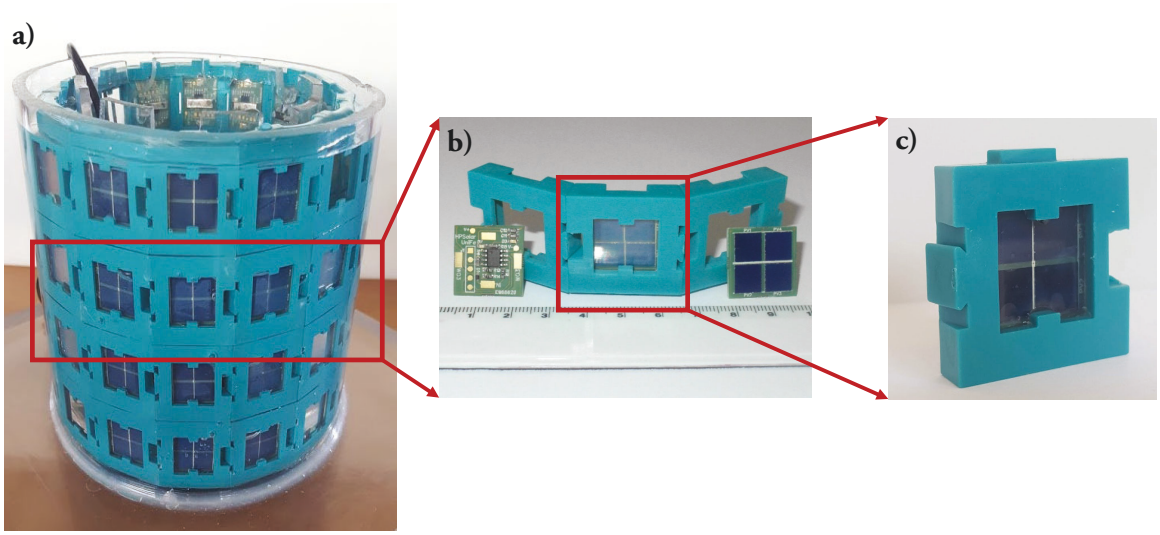

Figure 4.6: Picture of the modular reactor (a), of the single element components (b) and of the single element assembled (b, front side).

the slots that were obtained from the frame sides.

In this second version, more electronic components are present; they were soldered to the PCB by Surface-mount technology (SMT). Firstly, the solder paste was rubbed by a silk-screen printer (Smtech 100 MV). Then, the electronic components were placed by using an Autotronik BA385V Pick and Place. Finally, the assembly process was completed by melting the solder paste within an infrared reflow oven (Autotronik BT301P). The temperature was increased by heating ramps for 300 s with a permanence at 240 °C for 90 s, and a final decrease down to room temperature. The components were connected by following the scheme of the electronic circuit shown in Figure 4.7, which was designed by DipTrace, a schematic diagrams and PCB design software.

The electronic circuit, directly powered by the PV cells, applied an alternating bias to the electrodes. Here a microcontroller (Microchip PIC12LF1572) provided the required voltages (from 2.0 to 2.5 V and from 0 to -0.3 V) and timings to bias the photoanode and periodically restore its efficiency. The selected anodic bias (2.0–2.5 V) corresponded to the plateau photocurrent originated by the maximum hole transfer rate from the semiconductor to the electrolyte. Since the current available from the solar cells was ten times higher than the current absorbed by the anode (see Fig. 4.8 in the following section), a MPPT (Maximum Power Point Tracking) was not necessary, simplifying the design of the circuit. Moreover, anode and cathode were directly connected to the pins of the microcontroller, thus the applied bias was roughly equal to the V_{OC} of the solar cells without the contribution of the voltage drop

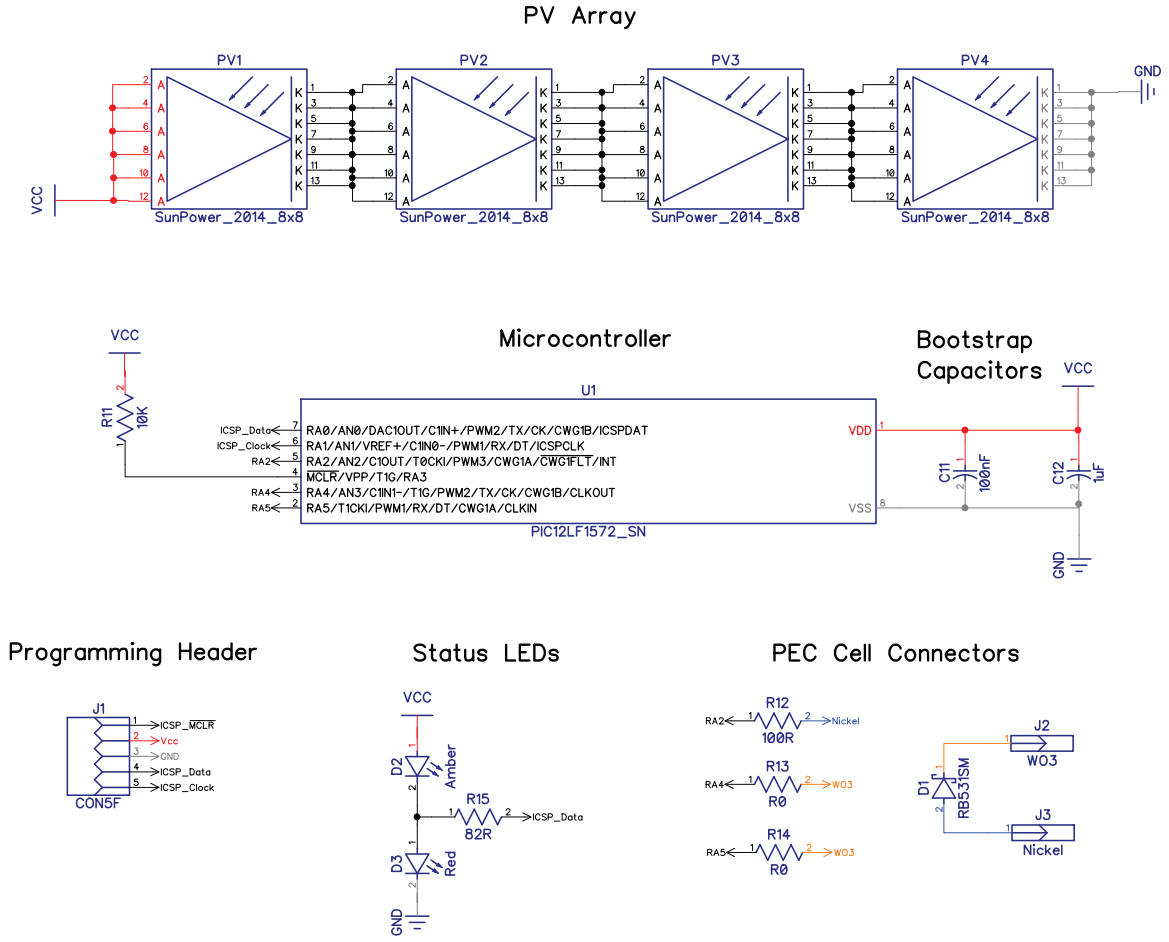

Figure 4.7: Scheme of the electronic circuit divided by functional blocks.

(typically of the order of 0.1–0.2 V) across the microcontroller. In order to limit the bias to -0.3 V during the reverse polarization cycles, a Shottky diode D_1 was connected in series to the electrodes while a resistor set the current limit. The current limitation was mandatory because, without MPPT, it prevented an excessive voltage drop from the solar cells. Observing the Scheme 4.7, J_1 was used to program the microcontroller, while C_{11} and C_{12} were capacitors able to switch on the microcontroller with a constant current. The diodes named D_2 and D_3 were LEDs used to check the correct functioning of the circuit: they lighted up for 200 ms according to the transition from direct to inverse polarization. The circuit elements $D_4 - D_7$ represented the four PV cells. The parallel R_{SH} and series R_S resistances were added to outline the behaviour of a real PV cell, respectively in parallel or in series. Finally, the resistances R_{13} and R_{14} connected the microcontroller with the anode, while R_{12} with the cathode.

4.2 Polarization cycles and photodegradation tests

4.2.1 TC bias and polarization cycles

The longer wavelengths of the solar radiation that impinge on the device could be converted by the PV cells, which were arranged behind photoanode in a tandem cell configuration. They powered the device by biasing the PEC cell to increase the anode photocurrent and hence the photocatalytic process.

Current-voltage curves were measured under solar simulator by using the bare PV cells in comparison with the addition of the photoanode ahead of the cells, in order to study the effect of the radiation absorbtion by the photoanode on the PV cell efficiency. The data were acquired by using a Tektronix Keithley (Series 2400 SourceMeter® Line) coupled with a Labview interface to obtain the current-voltage values. As can be observed in Figure 4.8, the current available from the solar cells was ten times higher than the current absorbed by the anode. Moreover, despite of the 32% of light absorption from the photoanode, the short circuit current decreased only of 26 %, showing a good coupling between the WO_3 photoanodes and the Si solar cells.

As already introduced in Chapter 2, after the JV measurements, chronoamperometry tests were carried out on the same electrodes in order to measure the photocurrent trends in time. Here, a drop of the efficiency over time was observed (Fig. 2.34). The phenomenon was probably due to the accumulation of peroxide intermediates on the WO_3 surface during water oxidation. The attempt of reactivating the electrode by applying a negative potential close to the V_{oc} value caused a temporary return of the photocurrent to the initial values. From here, the polarization cycles idea was devel-

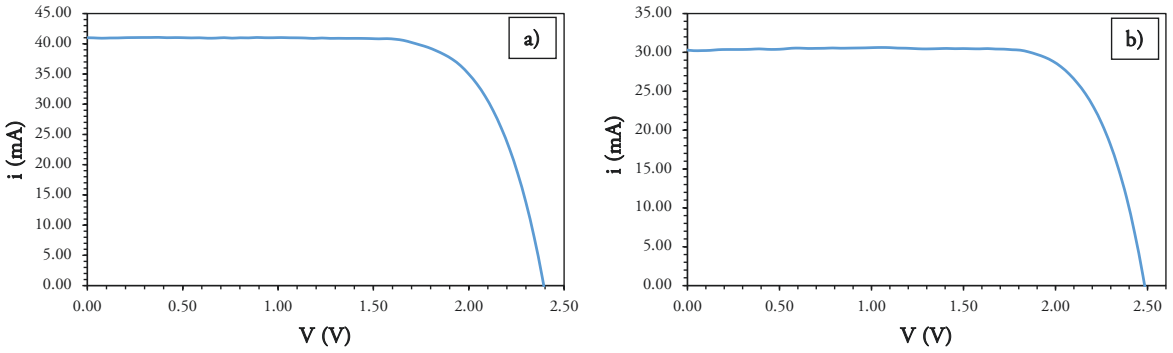

Figure 4.8: Characteristic curves of the PV cells in absence (a) and in presence (b) of the photoanode prior to the cells.

Table 4.1: Polarization cycles data to improve the photoanode efficiency: from left to right, the forward bias (FB) and the reverse bias (RB) with the respective timings, the initial J_i (t=0s) and the final J_f (t=4200s) current densities and the calculated efficiency by the rate J_f/J_i.

FB(V)	Time(s)	RB(V)	Time(s)	J_i (mA/cm^2)	J_f (mA/cm^2)	Efficiency
2.3	1800	-0.2	180	0.73	0.60	0.82
2.3	180	-0.2	30	1.82	0.64	0.35
2.3	4200	-0.2	0	1.95	0.96	0.49
2.3	180	-0.2	10	1.69	0.44	0.26
2.3	180	-0.2	18	1.16	0.29	0.25
2.3	180	-0.3	30	0.51	0.19	0.38

oped as a possible solution. Therefore, several measurements about the polarization cycles were performed to find the correct voltages and timings to improve the photoanode efficiency [96] (Table 4.1). The measurements were performed in Na_2SO_4 in concentrated (0.5 M) solutions.

A better efficiency was obtained in case of the application of 2.3 and -0.2 V for 1800 and 180 s, respectively. Unfortunately, the decrease of the photocurrent with time was reduced in speed but was still present. Therefore, other chronoamperometries were carried out in diluted (0.7 mM) solution of Na_2SO_4 as support electrolyte to 10 mg/l of atenolol. In these tests, the reproduction of a real-condition and neutral (pH 6.5) environment was attempted. The results are reported in Figure 4.9. Here, it can be observed that in case of diluted solution, i.e. in presence of low concentration of pollutants, and in a neutral environment, the polarization cycles sustained the photoanode efficiency by preserving a constant photocurrent production. This allows the maximum

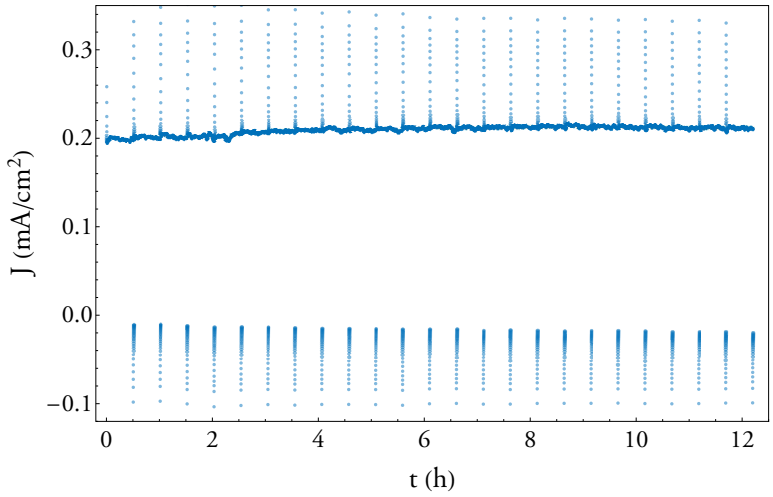

Figure 4.9: Chronoamperometry with polarization cycles of 2.3 V for 1800 s and -0.2 V for 180 s in ATN solution (10 ppm) with Na_2SO_4 0.7 mM pH 6.5, at 100 mW/cm^2).

possible hole transfer rate from the semiconductor to the electrolyte, and hence the photodegradation of the pollutants.

4.2.2 Photodegradation tests

All the discussed measurements concerning the chronoamperometry tests and the polarization cycles were carried out by using wires directly encapsulated within the devices. The wires helped to monitor the measurements via a direct connection with the PCB, and hence with the photoanode and the cathode. Differently, the photodegradation tests were performed by including the microcontroller within the single element, in order to make the device completely autonomous.

Thus, several microcontrollers were programmed by setting the studied voltages (2.3 and -0.2 V) and timings (1800 and 180 s). Then, they were encapsulated within the single elements. In this way, the device turned out to be completely independent and waterproof, and the only components in contact with the electrolytes remained the photoanode and the cathode for the redox processes occurrence. The photodegradation tests were carried out by using the same procedure discussed in the previous Chapter, but in this case it was used a mix of several drugs: Atenolol (ATN), Carbamazepine (CBZ), Levofloxacin (LVX) and 4-hydroxybenzaldehyde (HBA) with an initial concentration C_0 of 5 mg/l. Single elements were placed in flow under illumination of 100 mW/cm^2.

The obtained photodegradation are shown in Figure 4.10. Here, the ratio between the initial and the final concentrations C/C_0 is presented as function of the irradiation

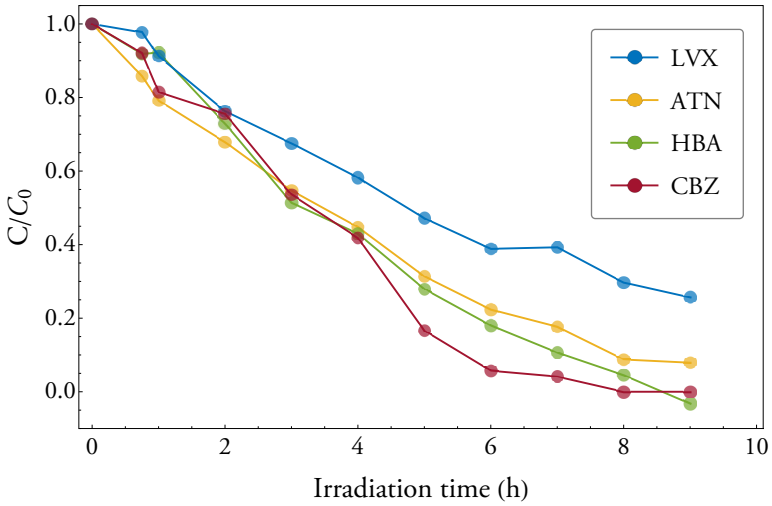

Figure 4.10: Photodegradation tests in flow on a mix of drugs: percentages of abatement are indicated. Atenolol (ATN) 92%, carbamazepine (CBZ) ∼100%, levofloxacin (LVX) 74%, and 4-hydroxybenzaldehyde (HBA) ∼100%, 5 mg/l under solar illumination at 100 mW/cm^2.

time. As can be observed, an abatement of more than 70% of Levofloxacine was obtained, but, even more encouraging, it is highlighted an almost complete degradation of the ATM, CBZ, and HBA, which was obtained with a completely stand-alone solar device.

4.3 Conclusions and further works

In this last Chapter, the modular stand-alone photoelectrocatalytic reactor has been presented. The reactor was born from the idea that the photoanode efficiency could extensively increase is the semiconductor is externally biased. Furthermore, this photoelectrocatalytic process can be environmentally sustainable when the bias comes from the solar energy, by exploiting photovoltaic cells. The reactor was a modular array of PVC frames building up a cylindrical structure. Thanks to the element modularity, the height of the reactor column can be tailored according to the user need by stacking multiple ring-shaped stages of PVC frames. Each element was a completely independent watertight system, composed by a photoanode in a tandem cell configuration with the photovoltaic cells, the electronic components, and a metallic cathode.

The components were encapsulated within each device, leaving the photoanode and the cathode as the only elements in contact with the electrolyte for the redox processes, as shown in Figure 4.11. The electronic circuit, directly powered by the solar cells,

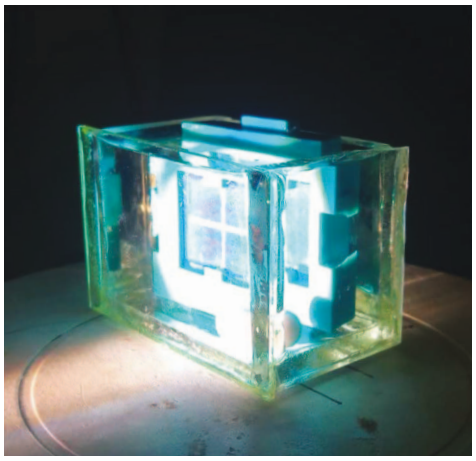

Figure 4.11: Single element device immersed into the electrolyte and illuminated during laboratory measurements.

applied an alternating bias to the electrodes. Between the electronic components, a microcontroller provided the required voltages and timings to bias the photoanode and periodically restore its efficiency via polarization cycles.

The photodegradation tests were carried out on a mix of drugs in flow conditions under the illumination of one sun. The measurements were carried out in a neutral environment and in case of diluted solution, according to the real conditions of a so-called tertiary stage of a waste-water treatment plant. The results showed outstanding percentages of abatement in particular in case of atenolol, carbamazepine, and 4-hydroxybenzaldehyde, whose photodegradation was almost complete. Also in case of Levofloxacine, the abatement percentage was around the 70%.

To date, it has to be highlighted that several drugs are still present in clean water after waste-water treatments and are spilled in the environment through water basins. In particular, in Italy several purifiers are not able to totally degrade these pollutants, and thus, for instance, Levofloxacine, Atenolol, and Carbamazepine are present in rivers in concentrations of respectively 0.6, 0.5, and 0.3 mg/m^3 [97]. For this reason, the discussed tests showed outstanding and encouraging results. In case of the shown reactor, a patent has been deposited and a possible scale up of the system may be possible. In consequence, the entire reactor prototype has to be tested in a real industrial or domestic context of waste-water treatment. The system shows the advantage of being environmentally sustainable, of exploiting only solar energy for its own functioning, and of being modular, and therefore adaptable to divers contexts and dimensions.

In addition, the possible production of solar hydrogen from photoelectrocatalytic technique is certainly an added value to the decontamination process. During the

HPSolar project, and hence during this thesis work, the research was focused in particular to the study of the material optimization, and to the design and the realization of the prototypes for the micro-pollutant degradation. However, by using theoretical calculations, it was estimated a production of 6.65 mmol/h for each single device of the realized reactor: undoubtedly a small number, but with margins of improvement. The hydrogen production by exploiting sunlight is extremely attractive due to several features.

- Photo-produced hydrogen is a valuable fuel and the highest clean energy carrier.
- It has a great advantage of transportation over long distances and storage for a long time.
- It can be produced for competitive prices with conventional fuels by renewable sources, innovative technologies, and smart processes[98].

To conclude, due to the promising results, an improvement of the reactor functioning is needed for an industrial scale up. The prototype will become part of the Crowdfunding Project of the University of Ferrara, within the realization of a solar column for water purification in small urban contexts.

Conclusions

This thesis work concerned the development of solar devices for wastewater treatment, whose working principle is based on photocatalysis and photoelectrocatalysis processes. Two different oxide semiconductors were examined as active material, which could be exploited for the oxidation processes triggered via sunlight.

Firstly, titanium dioxide (TiO_2) was investigated since it features a high stability, which is well known in literature. Considering that TiO_2 cannot absorb the visible light, a nitrogen-doped TiO_2 was used to realize the electrodes, which were produced as N-TiO_2 layers on glass substrates. Unfortunately, these electrodes did not show any activity in the visible range; this behaviour can be ascribed to an insufficient spectral response to the visible frequencies, probably due to the poor quality of the N-doping industrial process.

As an alternative, tungsten trioxide (WO_3) was chosen as active material for the electrodes because its band gap of 2.5–2.7 eV makes possible the absorption of the visible solar spectrum. Furthermore, it is resistant to photo-corrosion in aqueous solutions and it shows good electron transport properties. Nevertheless, to date, one of the most important parameters for practical applications, i.e. the stability of the photoanode, is still not addressed for this material. Therefore, the development of more efficient methods to overcome this feature is still urgent for the application in photocatalysis and in photoelectrocatalysis processes.

WO_3 can be prepared via several techniques. In this work, the WO_3 electrodes were realized by means of three different techniques, i.e. solvothermal, electrochemical oxidation, and sol-gel deposited on several substrates; such methods were selected because they permitted to obtain the nanostructuration of the WO_3 films. Indeed, since a nanostructured film has an increased surface roughness, it facilitates the penetration of the electrolyte, enhancing the photoinduced hole injection and facilitating the interfacial charge separation. The nanostructuration—nanopores and nanoflakes—was realized by means of the listed methods followed by electrode annealing at high temperature. The electrochemical characterizations of the electrodes pointed out pho-

tocurrents in the range of 1–5 mA/cm^2, which are consistent with the literature. Moreover, concerning the Incident Photon to Current Conversion Efficiency (IPCE), a wide spectral sensitivity was measured, and the activation in the visible part of the solar spectrum, up to ∼470 nm, was observed. For each electrode type, photodegradation tests were carried out on several specific drugs, which are barely eliminated by the current wastewater treatment plants.

The solvothermal technique was used to obtain crystal nucleation with a subsequent growth of WO_3 films in order to cover small glass spheres. In this case, photodegradation tests were carried out in flow conditions by using LED illumination in laboratory. The obtained drug abatement, in particular in case of Atenolol and Carbamazepine, was almost complete.

The electrochemical anodization of metallic tungsten was employed to create WO_3 layers over metallic foils. Also in this case, the photodegradation tests gave outstanding results. In addition, Chemical Oxygen Demand (COD) measurements were carried out on a set of hospital waste-water samples, obtaining an abatement of the 60% after 1 h of irradiation in presence of $Al_2(SO_4)_3$.

During the test worked out during this research, it has been observed that the anodized WO_3 showed an improvement in the photocurrent with increasing light intensity. Therefore, a parabolic linear trough solar concentrator was developed to increase the irradiation on the active material. Both the solvothermal glass spheres and the anodized tungsten were planned to be integrated in the parabolic concentrator, in order to have wastewater decontamination via photocatalysis. However, only the glass spheres were tested within the modulus, which was coupled by a pumping system. Further improvements have to be studied to allow a scale-up of the system to the industrial scope, in particular in the case of anodized WO_3, for which further investigation is mandatory to improve the electrochemical anodization on larger surface areas.

The third technique for WO_3 manufacturing, i.e. the sol-gel method, was exploited to realize colloidal WO_3, which was deposited via spin coating on a glass substrate covered by Fluorine-doped Tin Oxide, obtaining ∼1.5-μm thick films. These electrodes were integrated as photoanodes of PEC cells, which in turn were the base element for the solar devices. These single devices, once assembled each other, result in a modular stand-alone reactor for water decontamination. Owing to the tandem cell configuration of the photoanodes with photovoltaic cells, each device is self-powered only by solar energy. Indeed, the photovoltaic cells power the devices by biasing the PEC cells to increase the anode photocurrent and to allow polarization cycles to improve the photoanode efficiency. This strategy allows a higher drug photo-degradation, near to a complete abatement of the pollutants, thanks to the photoelectrocatalytic pro-

cess, which leads to an increase of the surface photo-hole density. Consequently, the coupled photogenerated electrons are transferred to the cathodic compartment, where they trigger proton reduction on the metallic cathode, obtaining hydrogen production. Certainly, the possible production of solar hydrogen is an added value to the decontamination process. A patent regarding the modular reactor structure and its working principle has been deposited during this work (IT 102019000010164).

This research was developed within the HPSolar (High Performance Solar Decontamination) project, which was part of the POR-FESR 2014-2020 program funded by Regione Emilia Romagna and European Union, and realized in collaboration with laboratories of the University of Ferrara and local companies, in particular HERA. The results of this thesis work, especially those concerning the modular reactor, were presented at the 69^{th} meeting of the International Society of Electrochemistry (ISE, 2018) and to the 25^{th} topical meeting of ISE (2019).

Further works regard a possible scale up of the modular reactor. From this perspective, pollutant abatement may be carried out in a real industrial or domestic context of waste-water treatment, by using the entire reactor, and not only the single elements. In addition, within the Crowdfunding Project of the University of Ferrara, named "Beviamo sicuri: l'energia solare al servizio della decontaminazione delle acque", in collaboration with the "Terra & Acqua Tech" laboratories, the final goal provides for the realization of a projecting roof integrating the solar concentrators for the waste-water treatment in a small urban context.

This work confirmed that photocatalysis and photoelectrocatalysis processes are among the most efficient Advanced Oxidation Processes for water decontamination by using a clean energy source. Certainly, both the designed and assembled solar devices for waste-water decontamination, namely the parabolic concentrator and the modular reactor, should concern the abatement of emergent organic micro-pollutants at the so-called tertiary treatment stage. Indeed, these solar systems have the necessity to treat clear water, in order to allow the solar rays to reach the electrodes for their photo-activation, which would be impossible in case of muddy water. In this way, after the oxidation treatment and before the water spill into the water basins, the pollutants that are currently present in the water environment, such as drugs, antibiotics, and other organic pollutants, can be eliminated by using the described sustainable process and without additional energy costs.

Acknowledgments

Ringrazio innanzitutto il Prof. Pasquini e la Dott.ssa Meda per aver gentilmente svolto il ruolo di referee di questa tesi. Ringrazio Donato, per essere stato il mio tutor in questi anni di dottorato e Stefano per aver accettato il ruolo di co-tutor. Grazie a chi ha fatto parte del progetto HPSolar e agli organizzatori della campagna di Crowdfunding. Ringrazio il mio gruppo di ricerca, per il sostegno e il supporto in questi anni. Grazie a tutti i miei amici, fisici e non, e soprattutto alle mie amiche. Grazie alla mia famiglia, tutta quanta. Grazie Riccardo.

La fisica è uno sforzo creativo.

Bibliography

[1] S. Uhlenbrook and R. Connor. The United Nations World Water Development Report 2017: Wastewater, the untapped resource, 2017.

[2] United Nations Environment Programme. A snapshot of the world's water quality: Towards a global assessment, 2016.

[3] International Food Policy Research Institute (IFPRI) VEOLIA. The murky future of global water quality: new global study projects rapid deterioration in water quality, 2015.

[4] A. De, R. Bose, A. Kumar, and S. Mozumdar. *Targeted Delivery of Pesticides Using Biodegradable Polymeric Nanoparticles*. Springer Briefs in Molecular Science, 2014.

[5] United Nations World Water Assessment Programme. The United Nations World Water Development Report 2014: Water and Energy, 2014.

[6] M. R. Hipsey and B. Arheimer. Challenges for water-quality research in the new iahs decade on: Hydrology under societal and environmental change. In *Understanding Freshwater Quality Problems in a Changing World*, pages 17–29, 2013.

[7] R.K. Pachauri and L.A. Meyer. Climate Change 2014: Synthesis Report. Contribution of Working Groups I, II and III to the Fifth Assessment Report of the Intergovernmental Panel on Climate Change, 2014.

[8] D. Panepinto, S. Fiore, M. Zappone, G. Genon, and Meucci L. Evaluation of the energy efficiency of a large wastewater treatment plants in Italy. *Appl. Energy*, 161:404 – 411, 2016.

[9] A. De Battisti, P. Formaglio, S. Ferro, M. Al Aukidy, and P. Verlicchi. Electrochemical disinfection of groundwater for civil use – An example of an effective endogenous advanced oxidation process. *Chemosphere*, 207:101–109, 2018.

[10] A. R.Ribeiro, O.C. Nunes, M.F.R. Pereira, and M.T. Silva. An overview on the advanced oxidation processes applied for the treatment of water pollutants defined in the recently launched Directive 2013/39/EU. *Environ. Int.*, 75:33–51, 2015.

[11] D. Robert and S. Malato. Solar photocatalysis: a clean process for water detoxification. *Sci. Total Environ.*, 291:85–97, 2002.

[12] S. C. Ameta and R. Ameta. *Advanced Oxidation Processes for Waste Water Treatment: Emerging Green Chemical Technology*. 2018.

[13] W.H. Glaze, J.-W. Kang, and D.H. Chapin. The chemistry of water treatment processes involving ozone, hydrogen peroxide and ultraviolet radiation. *Ozone Sci. Eng.*, 9:335–352, 1987.

[14] S. Gligorovski, R. Strekowski, S. Barbati, and D. Vione. Environmental Implications of Hydroxyl Radicals ($^{\bullet}$ OH). *Chem. Rev.*, 115:13051–13092, 2015.

[15] S. Caramori, F. Ronconi, R. Argazzi, S. Carli, R. Boaretto, E. Busatto, and C. A. Bignozzi. *Applied Photochemistry - Solar energy conversion in Photoelectrochemical System*, chapter 2. 2016.

[16] E. Spagnoli. Synthesis and characterization of photo-active hematite and tungsten trioxide electrodes for water-splitting, 2019.

[17] C.J. Philippopoulos and M.D. Nikolaki. *Photocatalytic Processes on the Oxidation of Organic Compounds in Water*. 2010.

[18] H. Choi, S. Al-Abed, D.D. Diionysiou, E. Stathatos, and P. Lianos. *TiO_2-based Advanced oxidation Nanotecnologies for water purification and reuse*, volume 2, chapter 8. 2010.

[19] J. Kotz, P. Treichel, and J. Townsend. *Chemistry and Chemical Reactivity*. 2008.

[20] C. A. Bignozzi, S. Caramori, V. Cristino, R. Argazzi, L. Meda, and A. Tacca. Nanostructured photoelectrodes based on WO_3: applications to photooxidation of aqueous electrolytes. *Chem. Soc. Rev.*, 42:2228–2246, 2013.

[21] M. Grätzel. Photoelectrochemical cells. *Nature*, 414:338–344, 2001.

[22] A.G. Maldonado, A.G. Fitch, and N.S. Lewis. *Nanostructured And Photoelectrochemical Systems For Solar Photon Conversion*. 2008.

[23] W. W. Gartner. Depletion-layer photoeffects in semiconductors. *Phys. Rev.*, 116, 1959.

[24] M. A. Butler. Photoelectrolysis and physical properties of the semiconducting electrode WO_2. *J. Appl. Phys.*, 48, 1977.

[25] D. S. Ginley and M. A. Butler. The photoelectrolysis of water using iron titanate anodes. *J. Appl. Phys.*, 48, 1977.

[26] A.E Becquerel. Recherches sur les effets de la radiation chimique de la lumiere solaire au moyen des courants electriques. *C. R. Acad. Sci.*, 9:145–149, 1839.

[27] J. Moser. Notiz über die verstärkung photoelectrischer ströme durch optische sensibilisierung. *Monatsh. Chem.*, 8, 1887.

[28] R. W. Gurney and N. F. Mott. Theory of the photolysis of silver bromide and the photographic latent image. *Proc. R. Soc. Lond. A*, 164:151–167, 1938.

[29] W. West. First hundred years of spectral sensitization. *Photogr. Sci. Eng.*, 18:35–48, 1974.

[30] W. H. Brattain and C. G. B. Garrett. Experiments on the interface between germanium and an electrolyte. *Bell Syst. Tech. J.*, 34:129–176, 1955.

[31] H. Gerischer. Electrochemical behavior of semiconductors under illumination. *J. Electrochem. Soc.*, 113:1174–1182, 1966.

[32] A. Fujishima and K. Honda. Electrochemical photolysis of water at a semiconductor electrode. *Nature*, 238:37 – 38, 1972.

[33] P. Lianos. Production of electricity and hydrogen by photocatalytic degradation of organic wastes in a photoelectrochemical cell: The concept of the photofuelcell: A review of a re-emerging research field. *J. Hazard. Mater.*, 185:575 – 590, 2011.

[34] P. Bernardoni, M. Boschetti, G. Mangherini, D. Vincenzi, S. Fugattini, A. Andreoli, V. Cristino, S. Caramori, and C.A. Bignozzi. A modular stand-alone photocatalytic reactor for waste water purification: the HPSolar project. In *Proc. 35th EU PVSEC 2018 Scientific Journal Publication of Papers*, volume 126, pages 1750–1753, 2018.

[35] L.J. Brillet, M. Cornuz, F.L. Formal, J-H. Yum, M. Gratzel, and K. Sivula. Examining architectures of photoanode-photovoltaic tandem cells for solar water splitting. *J. Mater. Res.*, 25:17–24, 2010.

[36] O. Khaselev and J.A. Turner. A monolithic photovoltaic-photoelectrochemical device for hydrogen production via water splitting. *Science*, 280:425 – 427, 1998.

[37] H. Fu Z. Li Q. Chen, G. Fan and Z. Zou. Tandem photoelectrochemical cells for solar water splitting. *Adv. Phys. X*, 3:1487267, 2018.

[38] M. A. Fendrich, A. Quaranta, M. Orlandi, M. Bettonte, and A. Miotello. Solar concentrators for wastewaters remediation: a review of materials and techonologies. *Appl. Sci.*, 9, 2019.

[39] R.J. Braham and A. T. Harris. Review of major design and scale-up considerations for solar photocatalytic reactors. *Ind. Eng. Chem. Res.*, 48:8890–8905, 2009.

[40] M. Tanveer and G.T. Guyer. Solar assisted photo degradation of wastewater by compound parabolic collectors: Review of design and operational parameters. *Renew. Sustain. Energy Rev.*, 24:534 – 543, 2013.

[41] S. Malato Rodríguez, J. Blanco Gálvez, M.I. Maldonado Rubio, P. Fernández Ibáñez, D. Alarcón Padilla, M. Collares Pereira, J. Farinha Mendes, and J. Correia de Oliveira. Engineering of solar photocatalytic collectors. *Sol. Energy*, 77(5):513 – 524, 2004.

[42] M. Grätzel and J. Augustynski. Tandem cell for water cleavage by visible light, 2001. WO Patent 0102624 A1.

[43] J.M. Keable, D.H. Auty, A. Stevenson, J. White, and S. Voorhess. Photoelectrochemical system, 2005. GB Patent 2414243 A.

[44] A. Birkel, Y-G. Lee, D. Koll, X.V. Meerbeek, S. Frank, M.J. Choi, Y.S. Kang, K. Char, and W. Tremel. Highly efficient and stable dye-sensitized solar cells based on SnO_2 nanocrystals prepared by microwave-assisted synthesis. *Energy Environ. Sci.*, 5:5392–5400, 2012.

[45] J.R. Swierk, D.D. Méndez-Hernández, N.S. McCool, P. Liddell, Y. Terazono, I. Pahk, J.J. Tomlin, N.V. Oster, T.A. Moore, A.L. Moore, D. Gust, and T.E. Mallouk. Metal-free organic sensitizers for use in water-splitting dye-sensitized photoelectrochemical cells. *Proc. Natl. Acad. Sci. U.S.A.*, 112:1681–1686, 2015.

[46] U. Joost, K. Juganson, M. Visnapuu, M. Mortimer, A. Kahru, E. Nõmmiste, U. Joost, V. Kisand, V. Vambola, and A. Ivask. Photocatalytic antibacterial activity of nano-TiO_2 (anatase)-based thin films: effects on escherichia coli cells and fatty acids. *J. Photochem. Photobiol. B.*, 142:178–185, 2015.

[47] Q. Chen, J. Li, X. Li, K. Huang, B. Zhou, and W. Cai. Visible-light responsive photocatalytic fuel cell based on WO_3/W photoanode and Cu_2O/Cu photocathode for simultaneous wastewater treatment and electricity generation. *Environ. Sci. Technol.*, 46:11451–11458, 2012.

[48] Z. Wu, G. Zhao, Y. Zhang, J. Liu, Y. Zhang, and H. Shi. A solar-driven photocatalytic fuel cell with dual photoelectrode for simultaneous wastewater treatment and hydrogen production. *J. Mater. Chem. A.*, 3:3416–34244, 2015.

[49] L. Xia, J. Bai, J. Li, Q. Zeng, X. Li, and B. Zhou. A highly efficient $BiVO_4$/WO_3/W heterojunction photoanode for visible-light responsive dual photoelectrode photocatalytic fuel cell. *Appl. Catal. B: Environ.*, 183:224–230, 2016.

[50] V. Cristino, S. Marinello, A. Molinari, S. Caramori, S. Carli, R. Boaretto, R. Argazzi, L. Meda, and C.A. Bignozzi. Some aspects of the charge transfer dynamics in nanostructured WO_3 films. *J. Mater. Chem. A*, 4:2995–3006, 2016.

[51] Q. Zeng, J. Bai, J. Li, L. Li, L. Xia, B. Zhou, and Y. Sun. Highly-stable and efficient photocatalytic fuel cell based on an epitaxial TiO_2/WO_3/W nanothorn photoanode and enhanced radical reactions for simultaneous electricity production and wastewater treatment. *Appl. Energy*, 220:127 – 137, 2018.

[52] G. Rossi, L. Pasquini, D. Catone, A. Piccioni, N. Patelli, A. Paladini, A. Molinari, S. Caramori, P. O'Keeffe, and F. Boscherini. Charge carrier dynamics and visible light photocatalysis in vanadium-doped TiO_2 nanoparticles. *Appl. Catal. B: Environ.*, 237:603–612, 2018.

[53] Q. Xiao, Z. Si, J. Zhang, C. Xiao, and X. Tan. Photoinduced hydroxyl radical and photocatalytic activity of samarium-doped TiO2 nanocrystalline. *J. Hazard. Mater.*, 150:62–67, 2008.

[54] R. Daghrir, P. Drogui, and D. Robert. Modified TiO_2 for environmental photocatalytic applications: A review. *Ind. Eng. Chem. Res.*, 52:3581–3599, 2013.

[55] S.A. Ansari, M.M. Khan, M.O. Ansari, and M.H. Cho. Nitrogen-doped titanium dioxide (N-doped TiO_2) for visible light photocatalysis. *New. J. Chem.*, 40:3000–3009, 2016.

[56] Y. Guo, X. Qiu, H. Dong, and X. Zhou. Trends in non-metal doping of the $SrTiO_3$ surface: a hybrid density functional study. *Phys. Chem. Chem. Phys.*, 17:21611–21621, 2015.

[57] R. Asahi, T. Morikawa, H. Irie, and T. Ohwaki. Nitrogen-doped titanium dioxide as visible-light-sensitive photocatalyst: Designs, developments, and prospects. *Chem. Rev.*, 114:9824–9852, 2014.

[58] A. Enesca, L. Andronic, A. Duta, and S. Manolache. Optical properties and chemical stability of WO_3 and TiO_2 thin film photocatalysts. *Rom. J. Inf. Sci. Tech.*, 10(3):269–277, 2007.

[59] C.W. Lai and S. Sreekantan. Fabrication of WO_3 nanostructures by anodization method for visible-light driven water splitting and photodegradation of methylorange. *Mat. Sci. Semicon. Proc.*, 16:303–310, 2013.

[60] D. Qin, C. Tao, S.A. Friesen, T. Wang, O.K. Varghese, N. Bao, Z. Yang, T.E. Mallouk, and C.A. Grimes. Dense layers of vertically oriented WO_3 crystals as anodes for photoelectrochemical water oxidation. *Chem. Commun.*, 48:729–731, 2012.

[61] C. Santato, M. Odziemkowski, M. Ulmann, and J. Augustynski. Crystallographically oriented mesoporous WO_3 films: Synthesis,characterization, and applications. *J. Am. Chem. Soc.*, 123:10639–10649, 2001.

[62] J. Su, X. Feng, J.D. Sloppy, L. Guo, and C.A. Grimes. Vertically aligned WO_3 nanowire arrays grown directly on transparent conducting oxide coated glass: Synthesis and photoelectrochemical properties. *Nano Lett.*, 11(1):203–208, 2011.

[63] R. Liu, Y. Lin, L.Y. Chou, S.W. Sheehan, W. He, F. Zhang, H.J. Hou, and D. Wang. Water splitting by tungsten oxide prepared by atomic layer deposition and decorated with an oxygen-evolving catalyst. *Angew Chem. Int. Ed. Engl.*, 50:499–502, 2011.

[64] W. Kim, T. Tachikawa, D. Monllor-Satoca, H. Kim, T. Majima, and W. Choi. Promoting water photooxidation on transparent WO_3 thin films using an alumina overlayer. *Energy Environ. Sci.*, 6:3732–3739, 2013.

[65] V. Cristino, L. Pasti, N. Marchetti, S. Berardi, C.A. Bignozzi, A. Molinari, F. Passabi, S. Caramori, L. Amidani, M. Orlandi, N. Bazzanella, A. Piccioni, J.K. Kesavan, F. Boscherini, and L. Pasquini. Photoelectrocatalytic degradation of emerging contaminants at $WO_3/BiVO_4$ photoanodes in aqueous solution. *Photochem. Photobiol. Sci.*, 18:2150–2163, 2019.

[66] S. Ortelli. *Tailoring properties and functionalities of TiO_2 and Ag nanoparticles involved in surfaces engineering processes.* PhD thesis, University of Bologna, 2015.

[67] S. Ortelli, A.L. Costa, and M. Dondi. TiO_2 nanosol applied directly on textiles using different purification treatments. *Materials*, 8:7988–7996, 2015.

[68] M. Minella. *Caratterizzazione elettrochimica dell'interfaccia semiconduttore-elettrolita in elettrodi a film sottile di TiO_2 nanocristallino.* PhD thesis, University of Torino, 2006.

[69] A. Pancaldi. Misure ottiche e caratterizzazione delle proprietà fotocatalitiche di campioni di ossidi metallici semiconduttori, 2019.

[70] I. Bodurov, I. Vlaeva, A. Viraneva, T. Yovcheva, and S. Sainov. Modified design of a laser refractometer. *Nanosci. Nanotechnol.*, 16:31–33, 2016.

[71] L. Meda, G. Tozzola, A. Tacca, G. Marra, S. Caramori, V. Cristino, and C.A. Bignozzi. Photo-electrochemical properties of nanostructured WO_3 prepared with different organic dispersing agents. *Sol. Energy Mater. Sol. Cells*, 94:788–796, 2010.

[72] H. Wang, T. Lindgren, J. He, A. Hagfeldt, and S.E. Lindquist. Photoelectrochemistry of nanostructured WO_3 thin film electrodes for water oxidation: mechanism of electron transport. *J. Phys. Chem. B*, 104:5686–5696, 2000.

[73] R. Solarska, B.D. Alexander, and J. Augustynski. Electrochromic and structural characteristics of mesoporous WO_3 films prepared by a sol-gel method. *J. Solid State Electrochem.*, 8:748–756, 2004.

[74] V. Cristino, S. Caramori, R. Argazzi, L. Meda, G.L. Marra, and C.A. Bignozzi. Efficient photoelectrochemical water splitting by anodically grown WO_3 electrodes. *Langmuir*, 27(11):7276–7284, 2011.

[75] M.F. Daniel, B. Desbat, J.C. Lassegues, and R. Garie. Infrared and raman spectroscopies of rf sputtered tungsten oxide films. *Journal of Solid State Chemistry*, 73(1):127 – 139, 1988.

[76] M. Allaf Behbahani, M. Ranjbar, P. Kameli, and H. Salamati. Hydrogen sensing by wet-gasochromic coloring of $PdCl_2$(aq)/WO_3 and the role of hydrophilicity of tungsten oxide films. *Sens. Actuator. B-Chem.*, 188:127–136, 2013.

[77] G. Leftheriotis, S. Papaefthimiou, and P. Yianoulis. The effect of water on the electrochromic properties of WO_3 films prepared by vacuum and chemical methods. *Sol. Energy Mater. Sol. Cells*, 83(1):115–124, 2004.

[78] G. Longobucco, L. Pasti, A. Molinari, N. Marchetti, S. Caramori, V. Cristino, R. Boaretto, and C.A. Bignozzi. Photoelectrochemical mineralization of emerging contaminants at porous WO_3 interfaces. *Appl. Catal. B: Environ.*, 204:273 – 282, 2017.

[79] A. Tacca, L. Meda, G. Marra, A. Savoini, S. Caramori, V. Cristino, C.A. Bignozzi, V.G. Pedro, P.P. Boix, S. Gimenez, and J. Bisquert. Photo-electrochemical properties of nanostructured WO_3 prepared with different organic dispersing agents. *Chem. Phys. Chem.*, 13:3025–3034, 2012.

[80] F. Angiuli, R. Argazzi, S. Caramori, and C.A. Bignozzi. Method for preparing nanocrystalline transparent films of tungsten oxide, 2007. PCT/IT2006/000084.

[81] K. Byrappa and M. Yoshimura. *Handbook of hydrothermal techonology: a technology for crystal growth and materials processing.* William Andrew publishing, Norwich, 2001.

[82] H. Yoshioka, H. Habazaki, A. Kawashima, K. Asami, and K. Hashimoto. An XPS study of the corrosion behavior of sputter-deposited amorphous Al-W alloys in 1 M HCl. *Corros. Sci.*, 32(3):313 – 325, 1991.

[83] M. Metikos-Hukovic and Z. Grubac. The growth kinetics of thin anodic WO_3 films investigated by electrochemical impedance spectroscopy. *J. Electroanal. Che.*, 556:167 – 178, 2003.

[84] L. Meda, A. Tacca, C.A. Bignozzi, S. Caramori, and V. Cristino. Modified tungsten oxide and process for its preparation, 2012. PCT/EP2010/004404.

[85] F. Passabì. *Propreità fotoelettrochimiche di giunzioni n-n di WO_3-$BiVO_4$ per water splitting.* PhD thesis, University of Ferrara, 2016.

[86] Y.P. Xie, G. Liu, L. Yina, and H. Chenga. Crystal facet-dependent photocatalytic oxidation and reduction reactivity of monoclinic WO_3 for solar energy conversion. *J. Maer. Chem*, 22:6746–6751, 2012.

[87] D. Zhang, S. Wang, J. Zhu, H. Li, and Y. Lu. WO_3 nanocrystals with tunable percentage of (001)-facet exposure. *Appl. Catal. B: Environ.*, 123-124:398–404, 2012.

[88] S. Caramori, V. Cristino, L. Meda, A. Tacca, R. Argazzi, and C.A. Bignozzi. Efficient Anodically Grown WO_3 for Photoelectrochemical Water Splitting. *Energy Procedia*, 22:127–136, 2012.

[89] J. Zhao, E. Olide, and F.E. Osterloh. Enhancing majority carrier transport in WO_3 water oxidation photoanode via electrochemical doping. *J. Elechtrochem. Soc.*, 162:H65–H71, 2015.

[90] R. Solarska, B.D. Alexander, A. Braun, R. Jurczakowski, G. Fortunato, M. Stiefel, T. Graulea, and J. Augustynski. Tailoring the morphology of WO_3 films with substitutional cation doping: Effect on the photoelectrochemical properties. *Electrochim. Acta.*, 55:7780–7787, 2010.

[91] R. Nakamura and Y. Nakato. Primary intermediates of oxygen photoevolution reaction on TiO_2 (rutile) particles, revealed by in situ ftir absorption and photoluminescence measurements. *J. Am. Chem. Soc.*, 126:1290–1298, 2004.

[92] D. Vincenzi. A lighting group, 2013. WO2013/156925A1.

[93] F. Aldegheri, S. Baricordi, P. Bernardoni, M. Brocato, G. Calabrese, V. Guidi, L. Mondardini, L. Pozzetti, M. Tonezzer, and D. Vincenzi. Building integrated low concentration solar system for a self-sustainable mediterranean villa: The astonyshine house. *Energy and Buildings*, 77:355–363, 2014.

[94] G. Hodes, D. Cahen, and J. Manassen. Tungsten trioxide as a photoanode for a photoelectrochemical cell (PEC). *Nature*, 260:312–313, 1976.

[95] D. Vincenzi, M. Boschetti, P. Bernardoni, C.A. Bignozzi, S. Caramori, V. Cristino, and L. Pasti. Sistema fotocatalitico modulare, 2019. IT 102019000010164.

[96] G. Mangherini. Development of a solar system for water decontamination treatment, 2018.

[97] E. Zuccato, S. Castiglioni, R. Bagnati, and R. Fanelli. I farmaci: inquinanti ambientali ubiquitari. *Quaderni acp*, pages 203–206, 2007.

[98] I. Dincer and C. Acar. Smart energy solutions with hydrogen options. *Int. J. Hydrog. Energy*, 43(18):8579 – 8599, 2018.